SCIENCE CHINA
Chemistry

•REVIEWS•

March 2023 Vol.66 No.3: 620–682
https://doi.org/10.1007/s11426-022-1475-x

Porous organic polymers: a progress report in China

Qing Hao[1†], You Tao[2,9†], Xuesong Ding[2†], Yajie Yang[3†], Jie Feng[4†], Rui-Lei Wang[4†], Xue-Ming Chen[4†], Guan-Le Chen[4†], Xiaomeng Li[5†], Huang OuYang[6†], XunLiang Hu[6†], Jia Tian[7†], Bao-Hang Han[2,9*], Guangshan Zhu[3*], Wei Wang[4*], Fan Zhang[5*], Bien Tan[6*], Zhan-Ting Li[7,8*], Dong Wang[1,9*] & Li-Jun Wan[1,9]

[1]*Key Laboratory of Molecular Nanostructure and Nanotechnology, Beijing National Laboratory for Molecular Sciences, CAS Research/Education Center for Excellence in Molecular Sciences, Institute of Chemistry, Chinese Academy of Sciences, Beijing 100190, China;*
[2]*CAS Key Laboratory of Nanosystem and Hierarchical Fabrication, CAS Center for Excellence in Nanoscience, National Center for Nanoscience and Technology, Beijing 100190, China;*
[3]*Key Laboratory of Polyoxometalate and Reticular Material Chemistry of Ministry of Education and Faculty of Chemistry, Northeast Normal University, Changchun 130024, China;*
[4]*State Key Laboratory of Applied Organic Chemistry, College of Chemistry and Chemical Engineering, Lanzhou Magnetic Resonance Center, Lanzhou University, Lanzhou 730000, China;*
[5]*School of Chemistry and Chemical Engineering, State Key Laboratory of Metal Matrix Composites, Shanghai Electrochemical Energy Devices Research Center, Shanghai Jiao Tong University, Shanghai 200240, China;*
[6]*Key Laboratory of Material Chemistry for Energy Conversion and Storage, Ministry of Education, School of Chemistry and Chemical Engineering, Huazhong University of Science and Technology, Wuhan 430074, China;*
[7]*Key Laboratory of Synthetic and Self-Assembly Chemistry for Organic Functional Molecules, Shanghai Institute of Organic Chemistry, Chinese Academy of Sciences, Shanghai 200032, China;*
[8]*Department of Chemistry, Fudan University, Shanghai 200438, China;*
[9]*University of Chinese Academy of Sciences, Beijing 100049, China*

Received October 17, 2022; accepted November 28, 2022; published online February 3, 2023

Porous organic polymers (POPs) are porous materials composed of light elements such as C, H, N, and O. The benign characters, including large surface area, good physical and chemical stability, well-defined chemical composition, wide ranges of monomer selection, and strong designability, have made POPs one of the frontiers in materials research. In this review, we discussed the design and synthesis of various POP materials that mainly led by Chinese scientists, including conjugated microporous polymers (CMPs), porous aromatic frameworks (PAFs), and hypercrosslinked porous polymers (HCPs), as well as crystalline POPs comprised of covalent organic frameworks (COFs) and a special class of COFs with triazine rings, covalent triazine frameworks (CTFs), and supramolecular organic frameworks (SOFs), and sorted out their main applications in adsorption, separation, catalysis, and electrochemistry fields.

porous organic polymers, conjugated microporous polymers, porous aromatic frameworks, hypercrosslinked porous polymers, covalent organic frameworks, covalent triazine frameworks, supramolecular organic frameworks

Citation: Hao Q, Tao Y, Ding X, Yang Y, Feng J, Wang RL, Chen XM, Chen GL, Li X, Ouyang H, Hu XL, Tian J, Han BH, Zhu G, Wang W, Zhang F, Tan B, Li ZT, Wang D, Wan LJ. Porous organic polymers: a progress report in China. *Sci China Chem*, 2023, 66: 620–682, https://doi.org/10.1007/s11426-022-1475-x

†These authors contributed equally to this work.
*Corresponding authors (email: hanbh@nanoctr.cn; zhugs@nenu.edu.cn; wang_wei@lzu.edu.cn; fan-zhang@sjtu.edu.cn; bien.tan@mail.hust.edu.cn; ztli@mail.sioc.ac.cn; wangd@iccas.ac.cn)

CONTENTS

1 Introduction

Porous materials are functional materials with pore structures, which are composed of continuous solid phases of the material skeleton and gas phase or liquid phase forming pores [1–3]. IUPAC divides porous materials into three categories according to the pore size, namely, microporous materials (<2 nm), mesoporous materials (2–50 nm), and macroporous materials (>50 nm) [1]. Inorganic porous materials include metal porous materials (like foam metal materials) and non-metal porous materials, which can be further categorized as natural or synthetic zeolites, pure silica molecular sieves, porous carbon, porous silicon, aerogel porous materials, and organic-inorganic hybrid materials like metal-organic frameworks (MOFs), *etc*. [4–6]. On the other hand, the porous organic polymer (POPs) is a kind of organic porous material with microporous or mesoporous structures, which is usually composed of C, H, O, N, B, and other elements [2]. POP materials always possess large pores, high surface areas, excellent stability and good designability, and can be widely used in various fields [7–19]. According to the structural characteristics of POPs, they can be divided into either amorphous or crystalline. Typical amorphous POPs mainly include conjugated microporous polymers (CMPs) [7–9], porous aromatic frameworks (PAFs) [10,11], and hypercrosslinked porous polymers (HCPs) [14–16], while crystalline POPs include covalent organic frameworks

(COFs) [17,18] and a special class of COFs with triazine rings, and covalent triazine frameworks (CTFs) [19]. Moreover, there are some crystalline framework materials linked by non-covalent bonds (like H-bonding interactions [20], halogen bonding interactions [21], ionic interactions [22]), such as supramolecular organic frameworks (SOFs) [12,13].

Pore structure is the most important feature of POPs. The timeline of POPs development is correlated with the advancement of chemistry to construct the porous structure. Generally, the molecules tend to form close-packed structures in the solid state. To avoid this tend, people use monomers with the rigid and non-planar backbones to construct polymers of intrinsic microporosity (PIMs). Unlike other types of POPs, PIMs are traditional one-dimensional polymers that are not networks composed of cross-linked covalent bonds. This characteristic endows them with good solubility but also makes the pore structure difficult to control. HCPs feature rich microporous structures by controlling the cross-linking of polymer chains and preventing the close packing between chains, and the micropores are fixed during or after the synthesis process. Later, CMPs and PAFs, which were constructed by coupling reactions with rigid molecules, were further developed. Except for amorphous materials, with the development of reticular chemistry, crystalline porous organic polymers COFs and CTFs have been proposed and demonstrated. In contrast, SOFs with similar framework structures were constructed entirely based on non-covalent interactions between organic molecules. It should be pointed out that some of the names of these POP materials do not have strict boundaries.

Based on the diversity of organic chemistry, there are many synthetic routes of POPs, including Yamamoto coupling [23,24], Suzuki coupling [25,26], Sonogashira-Hagihara cross-coupling [27,28], Schiff-base condensation [18,29], Knoevenagel condensation [30,31], and Friedel-Crafts alkylation reaction [32,33]. Through the rational selection of monomers and the special design of the synthesis route, the types and functions of POPs can be enriched.

Compared with inorganic porous materials such as zeolites, metal oxides, and MOFs, the advantages of POPs are very prominent. Firstly, the molecular chains of POPs are mainly composed of light elements and the skeleton densities are always low. Secondly, POPs are designed and synthesized by organic reactions from molecular building blocks, and thus it is convenient to realize the functionalization of POPs. The structural units of POPs are connected by covalent bonds and possess high physical and chemical stability, which can be used in some application that requires harsh environments. The unique structure features have made POPs to be candidate materials for a number of applications. Based on the design of pore structures, building blocks, stacking structures, and so on, POPs have shown excellent properties and enormous application potential in various fields. In recent years, Chinese scholars have made great contributions to the research of POP materials. This review summarized the structure, design, and synthesis of different types of POPs. Most POP materials synthesized in the solution phase are powder, and not easy to be processed. In this regard, great efforts have been paid to directly synthesize POP films. Finally, we exemplified the properties and potential applications of POP materials.

2 Design and synthesis of POPs

2.1 Conjugated microporous polymers

CMPs constructed by extended π-conjugation building blocks are a booming subclass of POPs. Since the first example was reported in 2007, the CMPs have been endowed with exuberant vitality by a wide range of conjugated monomers and network-forming reactions [7–9]. The functional units of CMP materials are incorporated into their conjugated networks to form permanent microporous structures. These characteristics allow CMPs to be utilized in a variety of frontier application fields including molecule adsorption/separation, thermocatalysis, photo/electro catalysis, energy storage, environment remedy, sensing, and biological application [34].

The common architectural structures of CMPs show three-dimensional (3D) conjugated networks with plenty of fixed permanent micropores. Therefore, the designed principles of CMP synthesis include at least: (1) conjugated monomers; (2) multiple functional groups for connection; (3) available polymerization reactions for network-formation. First, the π-conjugated system is required to be extended on the main skeletons of the microporous polymers, and thus the conjugacy of selected monomers is essential for designing the CMPs. Second, the monomers can provide extended π-conjugation skeletons for polymers rather than formation of oligomers or nonporous polymers. The combinations between building blocks with C_2 and C_3 symmetries are presented as the most common approaches for designing CMPs. As compared with $C_2 + C_3$ cases, the monomers with higher connectivity, such as C_4 or C_6 symmetry, show more diversity of connection directions and more possible combinations for constructing CMPs. Third, the polymers are constructed by covalent bond-forming reactions, which are required to contain appropriate functional groups to achieve polymerization [35]. For example, the first series of CMPs were synthesized through Sonogashira-Hagihara cross-coupling reaction. By selecting monomers with C_2 and C_3 symmetries, the polymers with alkynyl linkages were formed by using alkynyl compounds and halogen (iodine and bromine) compounds, and their Brunauer-Emmett-Teller specific surface area values were as high as 500–900 $m^2 g^{-1}$ [36].

Since the first CMP has been successfully prepared *via* Sonogashira-Hagihara cross-coupling reaction, some network-forming reactions are successively utilized to incorporate the conjugated building blocks into networks. Figure 1 shows the summary of most network-forming reactions for the synthesis of CMPs. Meanwhile, the commonly used building blocks that are classified into terminal alkyne-, halogen-, aldehyde-, amino-, carbazole-, and thiophene-functionalized building blocks have been summarized in Figures 2 and 3.

2.1.1 Preparation of CMPs by Sonogashira-Hagihara coupling reaction

Cooper and coworkers [37] employed 1,3,5-triethynylbenzene as the monomer, palladium as the catalyst, copper as the co-catalyst, and *N*,*N*-dimethylformamide (DMF) as the solvent to prepare the CMP with S_{BET} of 1,260 $m^2 g^{-1}$ *via* Sonogashira-Hagihara cross-coupling reaction. Meanwhile, lightweight alkyne struts were incorporated into the polymer networks. These alkyne struts propel the electron transfer within porous networks so that CMPs produced from terminal alkyne-monomers show application potential in photoelectron catalysis.

The numerous varieties of building blocks for the Sonogashira-Hagihara cross-coupling reaction are commercially available and contribute much to the preparation of novel and practical CMPs [38]. A series of CMPs with adjustable band gaps were prepared *via* a coupling reaction between alkynyl-containing monomers and iodine-functionalized ferrocene, which were applied to photocatalytic dye degradation [39]. Zhang and Feng and coworkers [40] employed nanocarbon materials as templates for preparing CMPs with dimensionality-controlled structures. Halogenated monomers were chosen as the functional monomer for polymerization with 1,3,5-triethynylbenzene through the metal-catalyzed Sonogashira-Hagihara coupling reactions on the template surface. The resulting CMPs with S_{BET} of about 600 $m^2 g^{-1}$ well inherit the original architecture of the corresponding templates.

2.1.2 Preparation of CMPs by Suzuki-Miyaura coupling reaction

In the presence of a mild base in DMF/water, Suzuki-Miyaura coupling reaction is a mature bond-forming reaction catalyzed by Pd(0), which couples an aryl-boron monomer with an aryl halide or sulfonate unit. The monomers of the Suzuki-Miyaura coupling reaction are abundant and commercially available. Notably, this reaction should be thoroughly degassed when constructing CMPs. Otherwise, its oxygen sensitivity would propel the production of by-

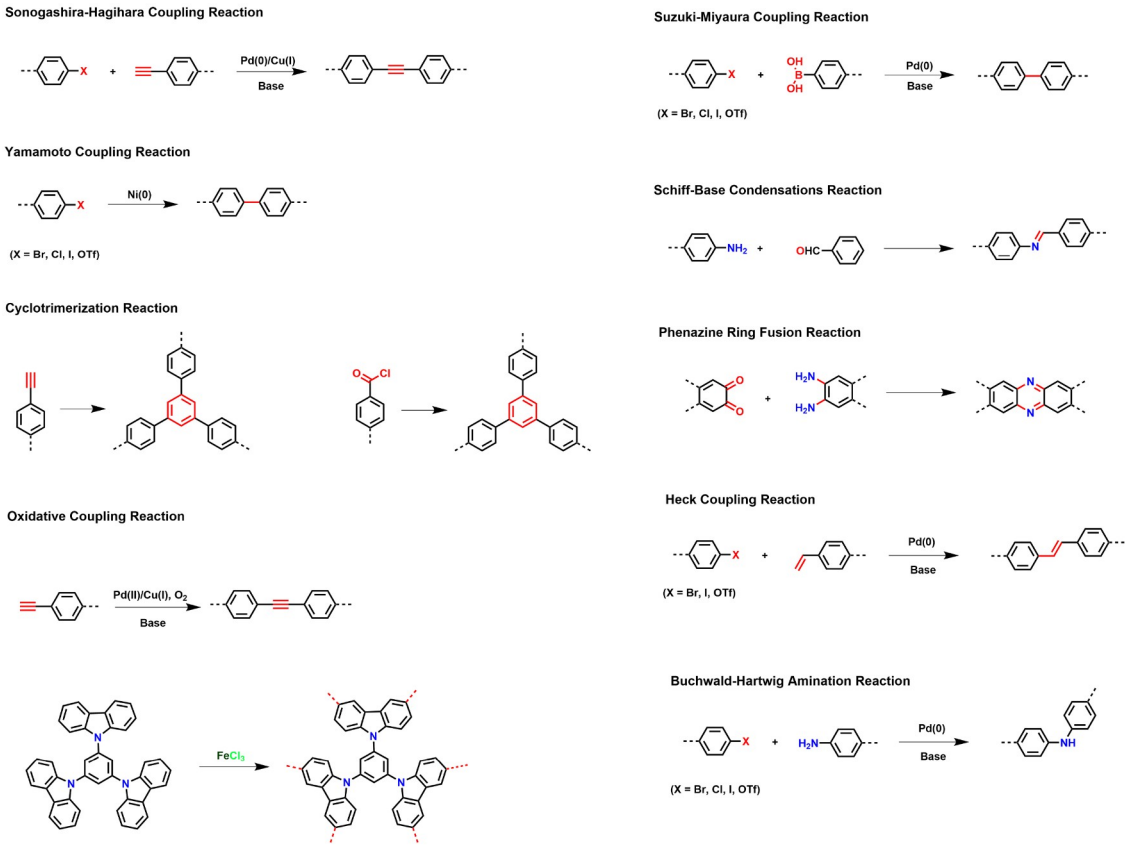

Figure 1 Summary of the network-forming reactions for CMP synthesis (color online).

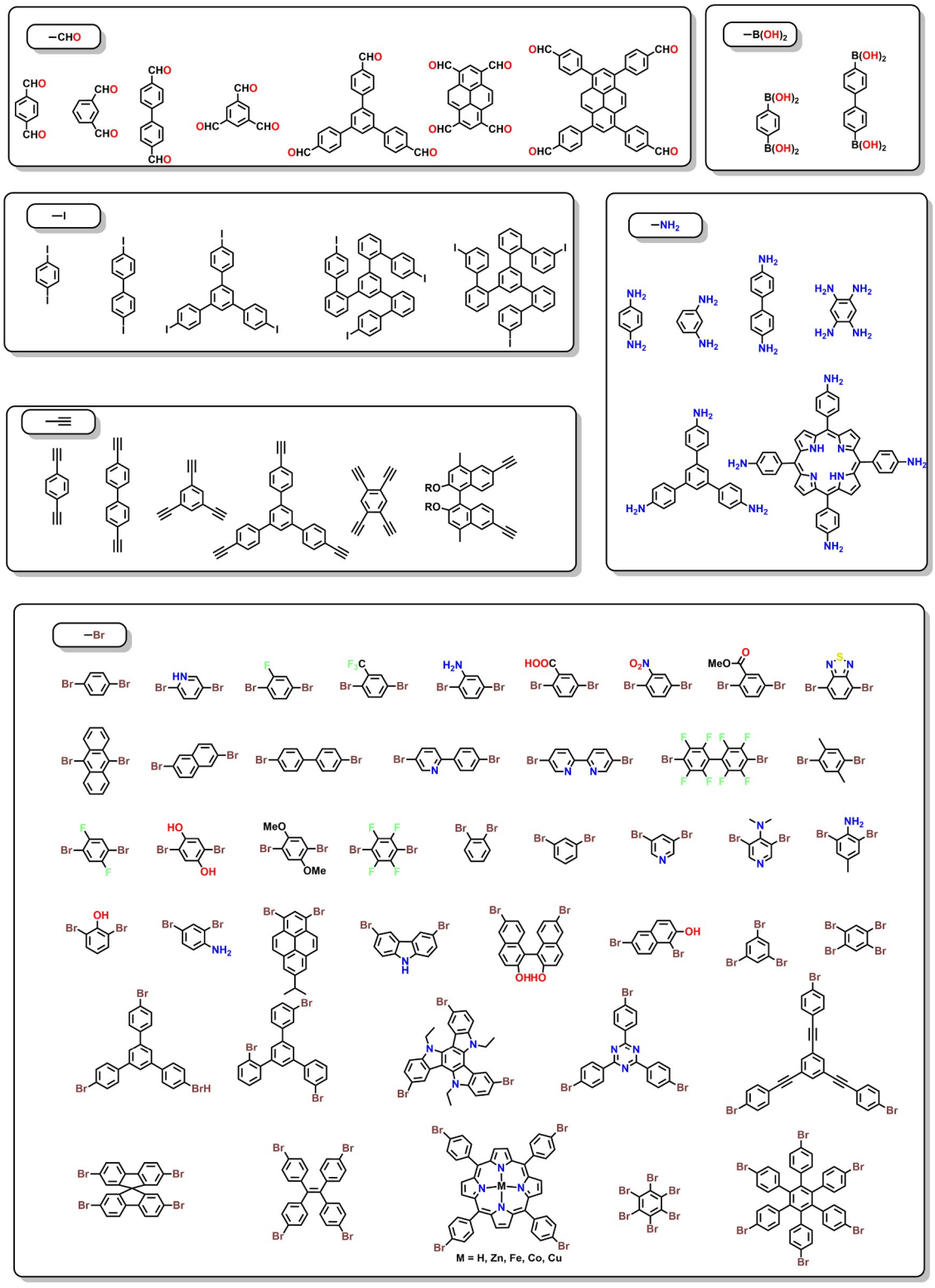

Figure 2 Summary of the terminal alkyne-, halogen-, aryl-boron-, aldehyde-, and amino-functionalized building blocks for CMP synthesis (color online).

products during this reaction, resulting in damage to CMP porosity.

In order to design photocatalysts for hydrogen evolution reaction, based on perylene with four polymerizable functional groups, Jiang and coworkers [25,26] developed a series of perylene-containing CMPs (PrCMPs) *via* Suzuki-Miyaura cross-coupling reaction. The pore property and band gap of the resulting PrCMPs are tunable by selecting

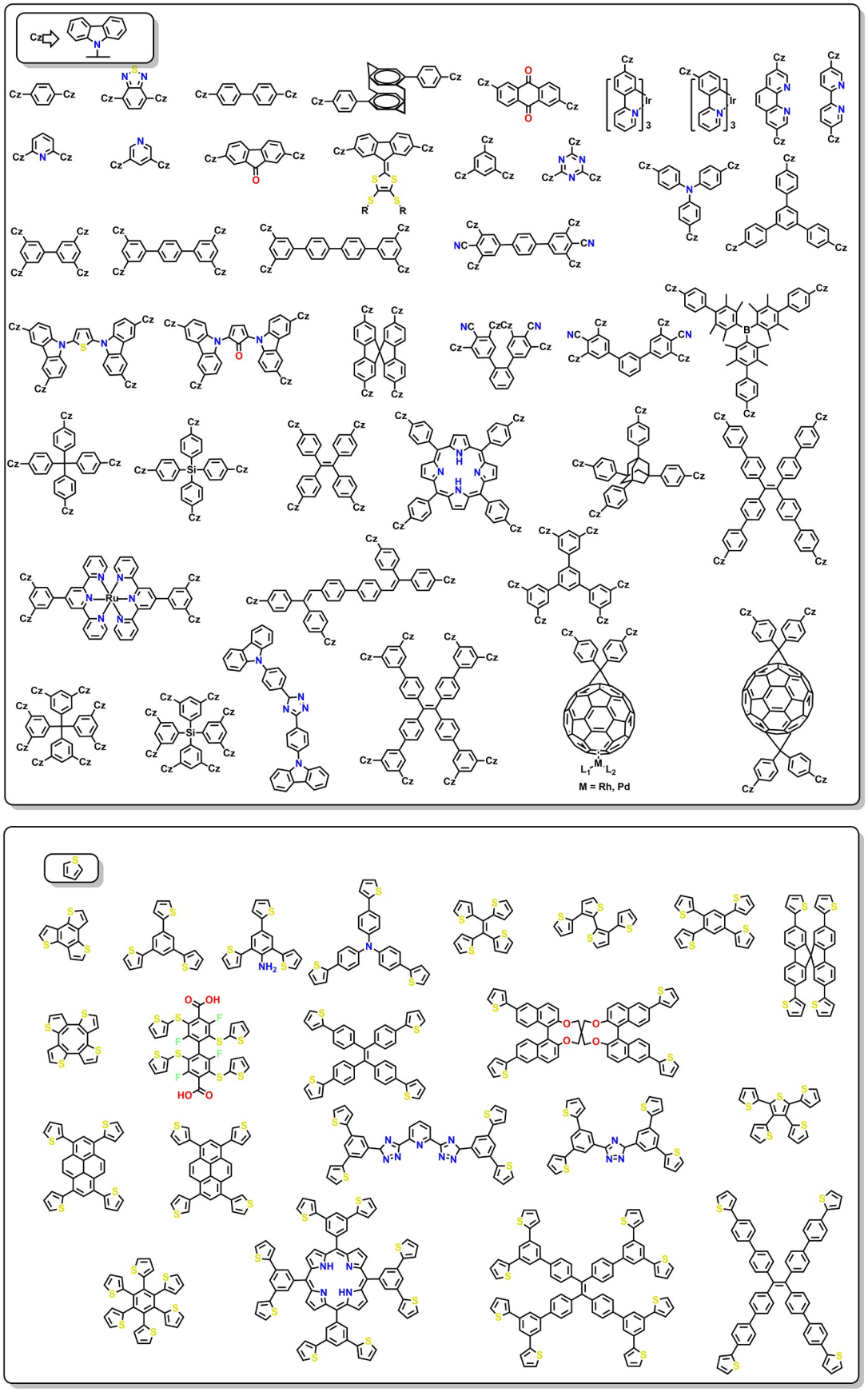

Figure 3 Summary of the carbazole- and thiophene-functionalized building blocks for CMP synthesis (color online).

the comonomers with different substituted groups and positions. This result demonstrates that the crucial role of the linkage geometry offers a general principle for the rational design of conjugated microporous polymer photocatalysts. Similarly, Niu and coworkers [41] synthesized two homologous conjugated skeletons of triazine units combined with perylene (CTP-1) and spirobifluorene (CTP-2) through the Suzuki-Miyaura coupling reaction, and the resulting materials served as the polysulfides immobilizer and catalyst to achieve high-performance Li-S batteries. Being compared with CTP-2, CTP-1 with perylene donor features a narrower band gap and faster electron transfer, thus exhibiting stronger binding ability toward polysulfides. These works broaden the understanding of the construction of CMPs by Suzuki-Miyaura cross-coupling reaction.

2.1.3 Preparation of CMPs by Yamamoto coupling reaction

Yamamoto reaction couples aryl halide monomers with nickel(0) as the catalyst to produce polymers with high specific surface area. The advantage of Yamamoto coupling reaction is that only one single type of aryl halide monomer is required, leading to a simple reaction procedure. This character simplifies the reaction conditions, such as reaction temperature, monomer solubility, solvent polarity, and specific catalysts. An important example of Yamamoto coupling reaction to prepare CMPs is the condensation of a carbazole derivative. Jiang and coworkers [23] synthesized a diindolocarbazole monomer for the construction of TCB-CMP with a large S_{BET} (1,280 $m^2 g^{-1}$) and blue luminescence.

CMPs with strong fluorescence are great candidates for sensing materials. A series of luminescent CMPs containing fluorescent units, such as triazine rings introduced by Cao and coworkers [24], and fluorene units introduced by Ren and coworkers [42], were prepared *via* Yamamoto coupling reactions. These luminescent CMPs show promising prospects in fluorescence detection. In view of the abundant types of commercially available halogen-functionalized monomers, the Yamamoto coupling reaction is considered one of the most commonly used methods for constructing CMPs.

2.1.4 Preparation of CMPs by cyclotrimerization reaction

Cyclotrimerization reaction is another kind of commonly used reaction for preparing CMPs. The "core", such as benzene and triazine, is produced from cyclotrimerization reactions, and becomes part of the skeletons of CMPs. For example, three alkyne monomer units generate benzene as "core" linkages to form extended networks [43].

Cyclotrimerization reaction typically forms aromatic rings as linkages to obtain an extended network [44]. A lot of researches about the construction CMPs by cyclotrimerization reaction focus on the formation of benzene or triazine rings through alkyne or cyano-functionalized monomer, respectively. In addition, Aldol self-condensation of di- and multiacetyl-containing building blocks catalyzed by thionyl chloride is a convenient route. A series of CMPs were synthesized by Han and coworkers [45] through this method, in which S_{BET} is as high as 832 $m^2 g^{-1}$ when using acetyl-functionalized tetraphenylmethane as the monomer. As a type of cyclotrimerization reaction, this route is a promising synthetic strategy for CMP construction by using acetyl-functionalized monomers [46,47].

2.1.5 Preparation of CMPs by oxidative coupling reaction

The oxidative coupling reaction is a typical method for constructing CMPs. Using 1,3,5-triethynylbenzene, homocoupled CMPs were synthesized by the oxidative coupling of terminal alkynes in the presence of Pd(II)/$CuCl_2$ and O_2 [48]. Besides the oxidative coupling for terminal alkynes, some electron-rich aromatics, such as carbazole, thiophene, and triphenylamine, were coupled *via* oxidative coupling reaction, which is catalyzed by Lewis acid including $FeCl_3$ and $AlCl_3$ in organic solution.

Representatively, the oxidative coupling reaction of 1,3,5-tri(9-carbazolyl)-benzene occurs at 3,6-position of carbazole units catalyzed by $FeCl_3$ to afford CMPs with S_{BET} as high as 2,200 $m^2 g^{-1}$ [49]. Meanwhile, inexpensive catalysts are in favor of controlling costs in the preparation of CMPs *via* oxidative coupling reaction [50,51]. Afterward, more and more porous polycarbazoles as one important type of CMPs were reported. The porosity of these porous carbazoles can be effectively adjusted by changing the length, size, and number of active sites of carbazole-functionalized building blocks [52]. Yu and coworkers [53] synthesized a series of carbazole-based CMPs with tunable redox potentials and explored photocatalytic performance with regard to C-3 formylation and thiocyanation of indoles. As a result, CMP-CSU6 derived from 1,3,5-tri(9*H*-carbazol-9-yl) benzene showed high efficiency for C-3 formylation and thiocyanation of indoles at room temperature due to its good oxidative capability. Han and coworkers [54] developed carbazole-based CMPs bearing rhenium-metalated polypyridine functionalities *via* oxidative coupling reaction. As heterogeneous photocatalysts, these materials show high efficiencies for CO_2 photoreduction. As for the construction of metal-free photocatalysts, Yu and coworkers [55] synthesized CMPs with the phenothiazine unit as a core by oxidative coupling reaction of carbazole-based monomers. CMPs with phenothiazine-core exhibit superior photocatalytic performance towards Ugi-type reaction and aerobic selenation of indoles compared with phenothiazine-free counterparts. The intrinsic semiconductor property of polycarbazole networks propels them to perform as advanced porous materials in the fields of photo-/electro-catalysis, sensing, and electronics.

Preparing carbazole-based CMP films *via* the emerging electrochemistry method boosts the practical potential of

CMPs in cutting-edge applications, such as information storage and electron/proton conduction. Without additional catalysts, the oxidative coupling reaction of carbazole-functionalized monomers can be induced by electrochemical potential, and the products show the formation of porous films with the thickness of nanometers. The electrochemical method may be one of the most effective methods for preparing carbazole-based CMP films, which shows unique advantages in solving the non-processability of traditional CMP bulk materials, especially in the construction of electronic devices, optoelectronic components, and wearable devices [56–58]. By using tetraphenyl ethylene-bearing carbazole units as monomers, Gu *et al*. [59] developed a facile electrochemical method for the direct synthesis of large-area CMP films. The approach enables the preparation of CMP films within even a few seconds and allows precise control over the thickness of these CMP films with sub-nanometer precision. Inheriting the fluorescence from monomers, the thin films enable the detection of explosives with a concentration at parts-per-million levels. Applying the same electropolymerization method, a high-luminescence CMP film was constructed with central tetraphenyl ethylene "core" by Li and coworkers [60]. These dendrimer-based CMP films show excellent sensitivity to volatile organic compounds.

Similar to carbazole monomers, thiophene and thiophene-functionalized building blocks possess a high density of electron clouds. Thus, the vicinal carbon of sulfur on the thiophene ring is prone to form covalent bonds in the oxidative coupling reaction, and these thiophene-functionalized building blocks are woven into porous polythiophene materials [61]. Some porous polythiophene materials produced from designed monomers, such as COTh, 1,3,5-trithienylbenzene, 1,2,4,5-tetrathienylbenzene, and hexathienylbenzene, show the S_{BET} values of more than 1,000 $m^2 g^{-1}$ [62,63]. Correspondingly, their porosity would be decisively influenced by the parameters of building blocks, such as the number of active sites. Notably, thiophene-based CMP films were successfully prepared *via* the electrochemistry method by Jiang and coworkers [64]. In the meanwhile, according to Wang and coworkers [65], the thiophene-based CMP films exhibit promising performance in photoenergy conversions and possess high potential in new application scenarios because the thiophene-based CMP is one of the few CMPs with sulfur-containing networks.

As for triphenylamine-based CMPs, Lu and coworkers [66] developed a novel conjugated poly[1,3,5-tri[4-(diphenylamino)phenyl] benzene] (MPDPB) with a pore size matching the size of bisphenol A (BPA) *via* oxidative coupling reaction. As a result, MPDPB showed super-high adsorption performance towards BPA and high absorbing stability under extreme environments due to suitable pore size distribution and high binding force between MPDPB and BPA. In short, the oxidative coupling reaction benefits from the abundant kind of monomers, commercial catalysts, and mild reaction parameters, which contributes a lot to the development of CMPs.

2.1.6 Preparation of CMPs by Schiff-base condensation reaction

Although the Schiff-base reaction is generally applied to synthesize crystalline covalent organic frameworks owing to its reversibility, it is also a commonly used method for constructing CMPs *via* forming conjugated imine linkages between amine and aldehyde-functionalized monomers. For example, by Schiff-base condensation reaction, Han and coworkers [29] reported the construction of novel metallophthalocyanine-based CMPs (MPc-CMPs). The extended π-conjugation systems and the microporous structure enable MPc-CMPs to be considered promising photosensitizers for the generation of $^1O_2$. Lu and coworkers [67] constructed a series of porphyrin-based donor-acceptor (D-A) type CMPs through a Schiff-base reaction between metalloporphyrins (MTAPP) and benzothiadiazole (BT) units. The transfer and separation of photo-induced carriers can be significantly improved through the metal-to-ligand charge transfer and electron push-pull effect between porphyrin units (electron donor) and benzothiadiazole moieties (acceptor). These investigations provide new insight into the design and synthesis of novel CMPs with enhanced photocatalytic activities.

2.1.7 Preparation of CMPs by other reactions

Besides the above-mentioned bonding reactions, more and more network-forming reactions have been developed and applied to the construction of CMPs. Heck coupling reaction and Buchwald-Hartwig amination reaction form vinyl-linkage and carbon-nitrogen bonds in the presence of a Pd(0) catalyst and a base, respectively [35]. As for Buchwald-Hartwig amination reaction, simple inorganic salts are used to tune pore size distribution and S_{BET} of *N*-containing poly (triphenylamine). In detail, the pore size distribution of poly (triphenylamine) is narrowed to the microporous range after the addition of inorganic salts rather than a broad distribution of micropores, mesopores, and macropores. The S_{BET} of *N*-containing poly(triphenylamine) is radically improved from 58 to 1,152 $m^2 g^{-1}$ [68]. Pyridyl building blocks with different substitutions were selected to synthesize four amine-linked CMPs (PTPA) networks *via* Buchwald-Hartwig cross-coupling reaction by Liao and coworkers [69]. PTPA obtained using 2,5-diaminopyridine dihydrochloride displays high specific capacitances. The polymer maintains good initial capacitances up to 65% upon 5,000 cycles. The formation of heterocycles serving as linkages between monomers can also endow CMPs with good porosity, such as phenazine ring, benzimidazole, and thiazolothiazole [70]. The emer-

ging functionalized building blocks of acetonitrile groups have constructed a series of acrylonitrile-linked CMPs with a high degree of conjugation through the condensation reaction with aldehyde groups [71]. In addition, some examples of CMPs synthesized through cross-linking of conjugated linear polymers were reported. For example, the 3D networks formed through cross-linking of polyaniline show porous structure, suggesting that these conjugated linear polymers can be regarded as a type of building block [72].

Owing to extended conjugation skeletons, high porosities, and excellent stabilities, CMPs have been evaluated for gas storage and separations, encapsulation of chemicals, heterogeneous catalysis, and so on. Furthermore, the development of new network-forming reactions attracts more types of monomers to participate in the construction of CMPs, which promotes the enrichment of the CMP types. These signs of progress allow CMPs to exhibit promising potential in the application of heterogeneous catalysis, photoredox catalysis, light emittance, sensing, energy storage, *etc*.

2.2 Porous aromatic frameworks

PAFs are another important member of the porous material family. They are well-known for their highly robust skeleton, ultra-large surface area, and high structural stability against extreme conditions including thermal, acid/basic, redox, and humid treatments [10]. The PAFs are constructed through bottom-up approaches from rigid organic monomers with predesigned configurations, which are defined as building units, and the frameworks are cross-linked *via* carbon-carbon bonds [11].

In contrast to the crystalline frameworks constructed *via* dynamically reversible reactions, PAFs are generally synthesized by irreversible coupling reactions. Although they are found to possess regularity in local structure, the distortion and free rotation of the phenyl-based fragments results in irregular network and architectural defects. Based on this unique structural feature, PAFs also distinguish them from other amorphous organic porous polymers, including HCPs with post-pillared polymer chains [73], polymers of intrinsic microporosity (PIMs) with distorted 1D polymeric skeleton [74], and CMPs originating from π-conjugated units [36].

As a remarkable example, the first porous aromatic framework (PAF-1) revealed an exceptionally large surface area with values of 5,600 $m^2 g^{-1}$ in the Brunauer-Emmett-Teller (BET) model and 7,100 $m^2 g^{-1}$ in the Langmuir model [75]. PAFs were synthesized under the guidance of theoretical prediction and designed by replacing the C–C bonds of diamond structure with benzene rings. The simulation indicated these porous materials were obtained with micro/meso pores and super-large specific surface areas. For example, tetrakis(*p*-bromophenyl) methane was selected as the tetrahedral monomer and linked by the Ullman coupling reaction for the preparation of PAF-1 (Figure 4). From the perspective of porous solids, PAF-1 simultaneously achieved the two important features of ultra-high stability and ultra-large surface area. Furthermore, the successful synthesis of PAF-1 revealed that high surface area can be obtained by amorphous networks, and thus it is regarded as a milestone for porous materials [76]. In the following decade, hundreds of PAF materials have been synthesized and the corresponding construction strategies, preparation methods, and extensive applications have been reported [77].

2.2.1 *Synthesis of PAFs*

Several key factors are essential for the design and synthesis

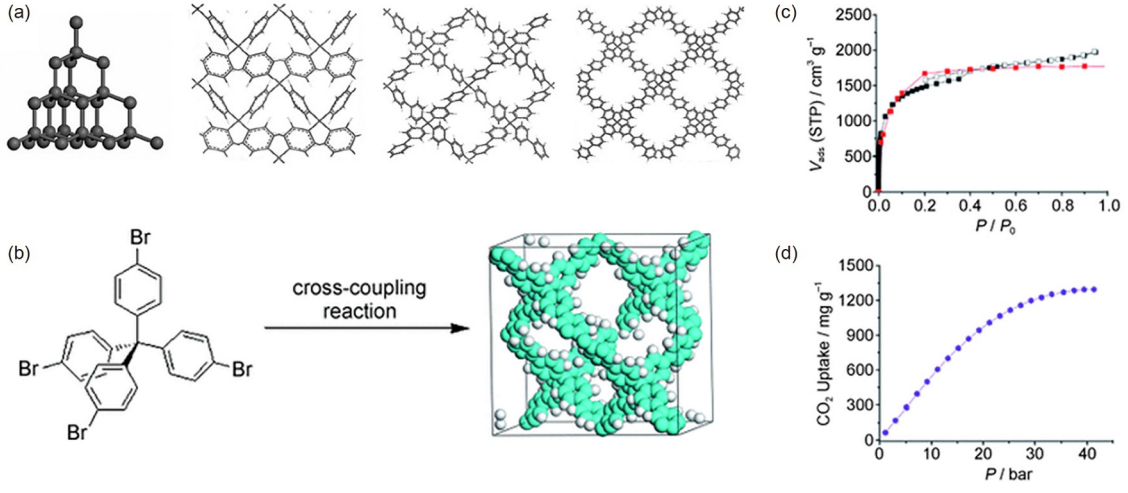

Figure 4 (a) Theoretical calculation of P1, P2, and P3, inserting respective one, two, and three benzene rings into the C–C bond of the diamond. (b) PAF-1 synthesized from the Ullman coupling reaction of tetrakis(*p*-bromophenyl)methane. (c) N_2 adsorption-desorption isotherms of PAF-1 powder at 77 K. (d) CO_2 adsorption isotherm at 298 K under high pressure [75]. Copyright 2009, Wiley-VCH (color online).

of PAF networks, including 1) building units with symmetrical configuration, 2) coupling reaction for efficient crosslinking, and 3) topology design strategy that directs the formation of framework structure. The reactive monomers normally contain benzene rings to form rigid building units with shapes of line, trigon, or tetrahedron. They hold the position of struts and joints and directly affect the overall structure of the porous materials. For example, monomers with three-reactive-node connected to each other are preferred to form two-dimensional hexagonal layered grids [78–81]. On the other hand, in order to achieve specific functions, targeted modifications of functional groups on these building units are required, like amino groups can be decorated on the aromatic unit to specifically bind to carbon dioxide molecules, thus improving the adsorption and storage capacity of carbon dioxide [80,82]. However, it is noteworthy that during the stage of PAF design some contradictions between reactive groups and functional groups should be considered. Specific functional groups may significantly affect the activity of reactive groups on reacting monomers. This in turn leads to a reduction in the yield of the coupling reaction, and thus, the continuity and extensibility of the grid are broken and structural defects increase [83].

With regard to the coupling reactions, a basic criterion for selecting coupling reactions is that they possess a high yield. Statistically, if the yield of a reaction is relatively low, it would seriously affect the integrity of the whole network when hundreds of such reactions occurred. Owing to the development of organic synthetic methodology, many effective coupling reactions such as Ullmann, Suzuki, Sonogashira-Hagihara, and Heck reactions have been applied for the preparation of PAF networks (Figure 5a) [84–87]. Such numerous choices provide us with lots of possibilities in the construction and functionalization of porous framework materials. For example, the reactivity of the Sonogashira-Hagihara reaction is barely affected by the functional groups. Through this reaction, functional groups such as carboxyl or amino groups in the network can be introduced into the PAF framework without reducing its porosity [27,28].

Topology design was extensively used for guiding the formation of crystalline open frameworks, such as metal-organic frameworks and covalent organic frameworks. The crystalline frameworks are usually achieved by reversible bond formation, so in the case of irreversibly linked frameworks like PAFs, the use of topology design strategy was to some extent ignored. However, it was revealed that the topology design was a powerful tool for structure prediction and function incorporation of PAF frameworks. Unique structures in PAF architecture can be designed by the selection of proper building units and suitable coupling reactions according to the guidance of topology design [88]. For example, triangular building monomers connecting to linear, triangular, and tetrahedral building units would respectively result in a series of PAF structures with tunable porous channels [89]. Desired functions can be decorated to the building units and introduced to the framework *in situ* [90]. Based on the above unique structural characteristics, PAF materials have been developed rapidly. Typical categories of

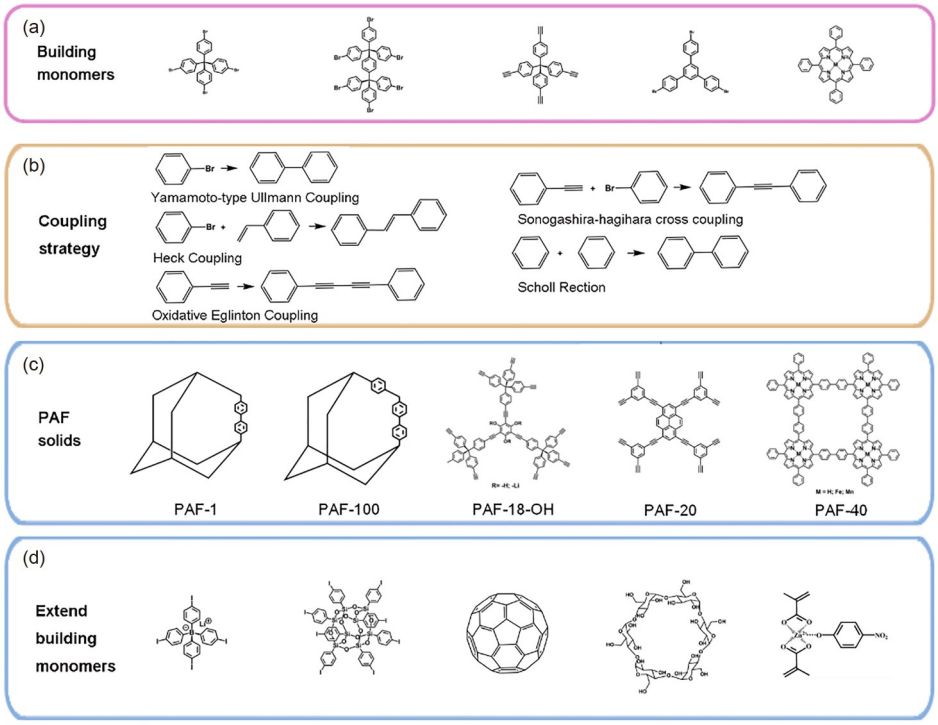

Figure 5 Schematic illustration of topology-directed design and final structures of PAF materials (color online).

large-surface-area PAFs, ion-skeleton PAFs, and molecularly imprinted PAFs are described below.

2.2.2 *PAFs with high surface-area*

Porous materials with large surface areas are an extremely precious feature. The large pore surface area indicates the existence of a large amount of space for mutual contact between the host and the object, thereby realizing the accommodation of a large number of atoms, molecules, ions, and the like. But in nature, matter tends to form densely packed structures and collapse occurs when the constructing bonds break caused by external stimulation. Therefore, it is scarce to obtain a rigid, stable material with a very large surface area. The successful synthesis of PAF-1 encouraged the research on the preparation of porous materials with a large surface area and excellent stability.

Isostructural porous networks of PAF-1 with different center atoms were first prepared. Qiu *et al*. [91] utilized tetrakis(*p*-bromophenyl)silane and tetrakis(*p*-bromophenyl) germane as building units replacing the tetrakis(*p*-bromophenyl)carbon for the PAF synthesis, resulting in the Si- and Ge-centered PAFs, denoted as PAF-3 and PAF-4, respectively. Zhou's group [92] adopted the four-node building monomers with different central motifs including adamantine, silicon, and germanium to synthesize the porous networks PPN-3, PPN-4, and PPN-5, respectively. All these samples presented extremely large specific BET surface areas with a value range from 2,900 to 6,500 $m^2\ g^{-1}$.

Other PAF materials with the ultrahigh surface area were also reported. Zhu's group [93] has made great progress in the synthesis of high surface area PAFs. They exploited a building-unit-engineering strategy and synthesized two new types of PAF samples, namely PAF-100 and PAF-101. These two materials were constructed from asymmetric building units, which have the dimer configuration of tetrahedral tetrakis(*p*-bromophenyl)silane monomers, both exhibiting high BET surface areas over 5,000 $m^2\ g^{-1}$. Meanwhile, these PAFs synthesized from dimer-shaped building units were found to have better structural regularity. The PAFs from the same building units were reported by Eddaoudi and coworkers [94]. They proposed a similar strategy named as the molecular-building-block approach. The obtained porous products also revealed ultra-large BET surface areas (ca. 5,120 $m^2\ g^{-1}$ for KPOP-1 and 5,730 $m^2\ g^{-1}$ for KPOP-2, respectively). Both works indicated the configuration of the building units and coupling reaction contributes to the synthesis of high surface area PAF materials.

2.2.3 *Ion-skeleton PAFs*

The recognition of guest molecules depending on their molecular size is effective but precise control of the pore size is usually hard to be achieved. Besides controlling the porosity of PAFs, pore chemistry is another important factor that affects the property and application of the material. For example, molecules are selectively captured by porous materials when specific interactions exist between adsorbents and adsorbates. Electrostatic interaction is one of the most common interactions in the channels of porous materials [95]. A series of PAF materials with ionic sites on electrically neutral frameworks were designed and prepared [96–103]. In 2014, cationic-skeleton-based PAF-50 solids were synthesized *via* the *in-situ* reaction of melamine and cyanuric chloride [96,97]. After the ion-exchange process, the counterpart chloride ions in the porous channels can be replaced by fluorine, bromine, and iodine ion. Because each ion has a unique kinetic size, the pore size was precisely adjusted from 7.2 Å (F-PAF-50) to 3.4 Å (2I-PAF-50). The synergy between the electronegativity of the ions and the size-dependent sieving effect led to the effective separation of five gas molecules (H_2, N_2, O_2, CH_4, and CO_2).

Besides the cationic skeleton, an ionic building unit, lithium tetrakis(4-iodophenyl)borate (LTIPB), with a boron-based anion center and tetrahedral structure was selected as the raw monomer. Through a Sonogashira-Hagihara coupling reaction, three alkyne monomers such as 1,4-diethynylbenzene, 1,3,5-triethynylbenzene, and tetrakis(4-ethynylphenyl)methane served as linkers and copolymerized with LTIPB to produce PAF-23, PAF-24, and PAF-25 [98]. Due to the introduction of the ion center and aromatic motifs in the framework, the resulting materials with anionic centers are capable of capturing iodide molecules with a strong binding capacity.

The imidazolium salts are inert in some coupling reactions for PAF construction. Therefore, it is possible to introduce imidazolium cations in the PAF framework by *in-situ* synthesis, which ensures the even distribution of the cationic sites in the framework. The obtained ionic PAF (iPAF-1) can be used for the application of adsorptive desulphurization and as catalyst support [99]. The iPAF-1 exhibited the highest adsorptive desulphurization capacity of 769.23 $mg\ g^{-1}$ for dibenzothiophene, which is due to the affinity between electron-rich thiophene-based compounds and electrophilic imidazolium motifs, as well as the fast diffusion of thiophene-based compounds in the ionic channels. The Keggin-type vanadium-based polyoxometalates (POMs) which were anionic catalysts were immobilized in the iPAF-1 as catalyst supports. The catalysis performance of the POM@iPAF-1 indicated that the composites were able to catalyze organosulfur compounds into their corresponding sulfones with better conversion efficiency under milder reaction conditions than POM does by itself [100]. The iPAF support captured the substrates and the POM sites catalyzed the conversion with a synergistic effect in the heterogeneous catalysis systems. The imidazolium-based iPAFs also exhibited potential usages for biotoxin removal and gas separation [101].

The PAFs with pending ionic sites are able to incorporate metal ions through the acid-base interaction. The incorporated metal ions bring strong gas-adsorbing affinity to the framework. Based on this idea, a series of materials have been prepared by introducing Brønsted acid groups such as hydroxyl and carboxylic groups into the backbone materials (PAF-18-OH and PAF-26-COOH) [102,103]. Alkali metals, such as lithium, sodium, potassium, and magnesium, reacted with the above groups and subsequently gave a series of ionic PAF solids, including PAF-18-OLi, PAF-26-COOLi, PAF-26-COONa, PAF-26-COOK, and PAF-26-COOMg. The polarized porous architecture has significantly improved their gas adsorption performance, and the adsorption capacity for H_2 and CO_2 is obviously increased compared with the neutralized pores. On the basis of large specific surface areas, the ionized PAF materials can realize precise regulation of the surface polarity. The combination of the porous skeleton with the ionic properties may have great potential applications in the fields of environmental protection, heavy metal removal, and catalysis.

2.2.4 Molecularly imprinted PAFs

The synthesis of PAFs with diverse structures and controllable properties sheds light on the unique structural characteristics of PAF solids and their unique functional applications. The assembly of multiple functional groups within PAFs can maintain their specific spatial configuration after the decoration of PAF skeletons. In view of this feature, it is expected to introduce the aggregation of different functional units with unique geometric configurations in the PAF structures. The so-called molecular imprinting technology is an effective method to achieve the recognition of guest species including ions, molecules, biomacromolecules, and even micro-organisms [104–106].

In general, molecular imprinting technology goes through several processes. First, target substances assemble with several functional groups by means of hydrogen bonds, ionic bonds, coordination bonds, *etc*. Then, the assemblies are modified into the structure of the polymer. After eluting the template, the specific recognition sites are formed in the polymer matrix. Molecular imprinting technology has unique advantages, such as stable structure, low cost, easy operation, and high selectivity. However, a polymer matrix itself has a certain degree of flexibility, resulting in slow mass transfer, template molecule leakage, and low binding capacity. Recently, molecular recognition by molecular imprinting technology has been successfully combined with PAFs to achieve effective host-guest interactions, leading to a series of molecularly imprinted PAF materials (MIPAFs) [107–110].

Imprinting sites for lead were formed by the coordinating interactions of two carboxylic acid groups and two pyridyl groups with lead ions within a multi-directional framework [107]. Subsequently, the combination of salicylaldehyde oxime, carboxylic acid groups, and pyridyl groups with uranyl ions resulted in the preparation of the uranyl imprinted PAFs with three functional groups [108]. It is worth mentioning that PAF materials have a highly stable skeleton, which bears multiple operations. This method can maintain the open pore structure of the PAF materials, thereby improving the binding efficiency for guest molecules. For example, through a multiple-step programming modification, the uranyl-specified bis-salicylaldoxime entity was combined into the porous framework. The prepared material manifested high ion selectivity and extremely high ion adsorption capacity. Its adsorption capacity is nearly 30 times higher than that of polymer-based adsorbents [109]. Besides the application for chemical recognition and adsorption, the molecularly imprinted PAFs also showed their potential usages in molecule recognition for selective catalysis. Carboxylic acid and imidazole group coordinate two zinc ions to form a hydrolysis complex for organophosphorus molecules. At the same time, zinc carboxylate ion was exploited to interact with *p*-nitrophenol for the role of the transfer complex. Both the hydrolytic complex and transfer complex were decorated to the PAF material to achieve a porous artificial enzyme with a tandem hydrolysis effect. The above materials show high binding capacity and selectivity when catalyzing the target reactions [110]. Compared with the molecularly imprinted polymer, the adsorption capacity of MIPAFs reveals a multifold increasement. More importantly, the rigid skeleton of PAFs effectively maintains the relative spatial positions of each functional group, leading to an ultra-high selectivity for ions/molecules.

2.3 Covalent organic frameworks

COFs can be regarded as crystalline porous polymers, which possess periodic and covalently linked networks along with ordered pores. Being crystalline distinguishes COFs from other amorphous POPs. According to the principles of dynamic covalent chemistry [111] and reticular chemistry [112], numerous COFs have been successfully synthesized since 2005 when COFs were first reported [17]. However, relying on the use of reversible reactions, the obtained COFs always lack adequate stability. In addition, limited by the category of reversible reactions and symmetry of building blocks, the synthetic protocols and topologies of COFs were awaited to be diversified. Furthermore, the acquirement of highly crystalline COFs, *i.e*., single-crystal COFs, was difficult because of the fast nucleation process in the synthetic systems resulting from the fast formation of covalent bonds. It is highly desired to develop new synthetic methodologies and strategies to enhance the stability and crystallinity and broaden the structural diversity of COFs.

In 2011, Wang and coworkers [18] reported the first work

of COFs in China. They constructed the first 2D imine-linked COF, denoted as COF-LZU1, to explore the application in heterogeneous catalysis. A decade later, an increasing number of research groups in China participated in the research of COFs [113–123]. The main contributions devoted by our colleagues to the development of the synthesis of COFs can be divided into four parts: new strategies, new linkages, new topologies, and chiral COFs, as highlighted herein.

2.3.1 New strategies

The most difficult thing in the synthesis of COFs is to achieve the crystallization and reaction process simultaneously. Aiming to synthesize COFs with high crystallinity and stability, the establishment of effective and general synthetic strategies is fundamentally important. Herein, we summarized the representative and influential strategies developed by the researchers in China.

Protective group strategy. In 2016, Wang and coworkers [116] reported the synthesis of imine-linked COFs from the condensation between amines and dimethyl acetals. This protective group strategy of using acetals rather than aldehydes can avoid the oxidation of aldehydes in synthetic conditions; besides, acetals have better solubility than their aldehyde counterparts, which is advantageous for the crystallization process. This work exemplified the control in crystallization by tuning the reactivity and solubility of monomers in the synthesis of imine-liked COFs. Notably, this strategy has been widely applied to explore linkage chemistry [124] and synthesize highly crystalline COFs [125].

Reformation strategy. In 2016, Guo and coworkers [117] presented an ingenious strategy to achieve the disorder-to-order reformation from amorphous networks to crystalline COFs. They first covered the Fe_3O_4 nanoclusters with disordering imine-linked organic polymer shells. Then, the amorphous-to-crystalline transformation would be realized through the thermodynamic control process with pyrrolidine as the catalyst. This reformation strategy provides a good choice for the construction and functionalization of crystalline nanoCOFs by post-treatment.

Linker exchange strategy. In 2017, Zhao and coworkers [126] achieved the COF-to-COF transformation by heterogeneous linker exchange. Linkers in pristine COFs could be replaced by other linkers *via* the dynamic exchange of covalent linkages. This strategy can help to obtain COFs which are hard to be synthesized in the one-pot construction and has been widely applied to constructing COFs with new linkages [127,128].

Modulator strategy. Growing single crystals represents the highest level of controllability on the COFs' synthesis. In 2018, Wang and collaborators [129] applied aniline as the modulator for growing high-quality large single crystals of 3D imine-linked COFs. The addition of large excess of aniline can alter the synthetic path from Schiff-base condensation to a more reversible imine exchange reaction, which is beneficial for slowing the nucleation in the crystallization process. Thus, the structural information at the atomic level of COFs, such as degree of interpenetration, arrangement of covalent bonds, identification of chiral topology, host-guest interaction, and stacking mode, could be disclosed experimentally by single-crystal X-ray diffraction data.

"Two-in-one" strategy. Screening the solvents is an indispensable procedure in the synthesis of COF. However, the conventional trial-and-error experiment is highly time-demanding and labor-consuming. The reason may lie in the different solubility of monomers which would lead to the mismatched reactivity of monomers in the crystallization process. To resolve this problem, Chen and coworkers [130] developed the "two-in-one" strategy, which combined two different reactive sites into one monomer, for the COF synthesis. The presence of these "two-in-one" monomers could make the corresponding COFs being highly crystalline and facilely synthesized in various solvents.

Cascade reactions. Reversible reactions were mainly explored to develop new linkages of COFs. However, the stability of COFs is always unsatisfactory because of the presence of these weak covalent linkages. Aiming to create the robust linkages of COFs, Wang and coworkers [118] strategically combined reversible and irreversible reactions into a cascade protocol for the one-pot construction of benzoxazole-linked COFs. The reversible steps may correlate to the crystallization process, whereas the irreversible transformation could help to form strengthened covalent linkages, so as to obtain COFs with high stability even in strong acidic or basic conditions. After this work, many robust linkages, such as furan [131] and pyrano[4,3-*b*]pyridine [119] linkages, have been developed through the cascade reactions.

Multicomponent reactions. In 2019, Wang and coworkers [118] developed an elegant strategy that exploits multicomponent reactions to construct robust COFs. They achieved the construction of imidazole-linked COFs *via* the co-assembly among diketones, ammoniums, and aldehydes. The formation of each cyclic linkage involved the formation of five covalent bonds in a one-pot protocol, which exhibited a higher level of complexity and precision in COF synthesis. Notably, benefiting from this strategy, the elaborate design of monomers could be avoided. Nowadays, many readily available compounds, *i.e.*, 2-aminopyridine [132], sulfur [133], phenylacetylene [134,135], TMSCN [134], and phosphoric acid [136], could be reticulated to yield robust COFs.

2.3.2 New linkages

The requirement in terms of high stability, high crystallinity,

and functional diversity inspired the development of linkage chemistry of COFs. Numerous new linkages of COFs were discovered through the introduction of classical organic reactions from conventional organic chemistry. It should be noted that many new linkages were discovered by Chinese colleagues for the first time (Figure 6).

Imine-derived linkages. Imine-linked COFs are the most widely explored family; however, the strong polarization of imine bonds would undermine the chemical stability of imine-linked COFs. To address this issue, researchers explored some strategies to transform the imine bonds into other chemical linkages with higher stability. In 2018, Wang and coworkers [137] reported the one-pot construction of ultrastable benzoxazole-linked COFs by developing a cascade reactions strategy. The formation of benzoxazole rings involved a cascade sequence, which combined reversible imine formation, irreversible cyclization, and oxidation between 2,5-diamino-1,4-benzenediol dihydrochloride and multitopic aldehydes. Recently, they also achieved the one-pot construction of fused-ring-linked COFs [119]. By conducting a cascade protocol involving Schiff base condensation, intramolecular [4 + 2] cycloaddition, and dehydroaromatization, a series of bicyclic pyrano[4,3-*b*] pyridine COFs were successfully constructed. In 2019, Zhao and coworkers [138] constructed aminal-linkage COFs by the condensation of piperazine with D_{2h} symmetric tetraaldehydes. The formation of aminal linkage involved Schiff base condensation and the nucleophilic attack on Schiff base by another secondary amine.

Through the integration of multicomponent reactions strategy and isocyanide chemistry, Wang and coworkers [132] synthesized a series of pyrimidazole-based COFs *via* Groebke-Blackburn-Bienayme reaction from isocyanides, aminopyridines, and aldehydes. By carrying out the three-component Povarov reaction, Yang and coworkers [139] prepared tetrahydroquinoline-linked COFs in a one-pot fashion between multitopic anilines, multitopic aldehydes, and ethyl vinyl ether. In 2020, Dong and coworkers [134] reported the one-pot construction of the α-aminonitrile-linked COF by a three-component Strecker reaction between trimethylsilyl cyanide, 1,3,5-tri(4-aminophenyl)benzene, and 2,5-dimethoxy terephthalaldehyde. Notably, they lately achieved the catalytic asymmetric synthesis of COFs for the first time [135]. Two enantiomers of COFs with chiral propargylamine linkages were constructed by applying the asymmetric multicomponent A^3 coupling reaction.

The post-synthetic modification is another powerful tool to achieve the linkage development of COFs. In 2018, Deng and coworkers [140] successfully transformed imine-linked COF-300 to secondary amine-linked COF by using $NaBH_4$ as the reducing agent. In 2020, Zhao and coworkers [141] achieved the construction of thieno[3,2-*c*]pyridine-linked COFs *via* the Pictet-Spengler reaction between imine carbons in the prepared imine-linked COFs and thienyl groups which were carefully placed at the *ortho* position of aniline-derived monomer. In 2021, Chen and coworkers [142] reported the synthesis of arylamine-linked COFs which were prepared from the ketamine-linked COFs after the post-oxidative treatment. Lately, Wang and coworkers [143] constructed the first ladder-type COFs by the post-synthetic conversion. The preintegrated alkyne groups can react with imine-derived 2-aza-1,3-dienes *via* the intramolecular Povarov reaction to afford chromenoquinoline linkages.

Olefin-based linkages. Traditional imine-linked COFs suffer from some disadvantages, such as the relatively low stability and poor electron delocalization directly related to their highly reversible dynamic covalent bond linkers, severely limiting their potential application. The carbon-car-

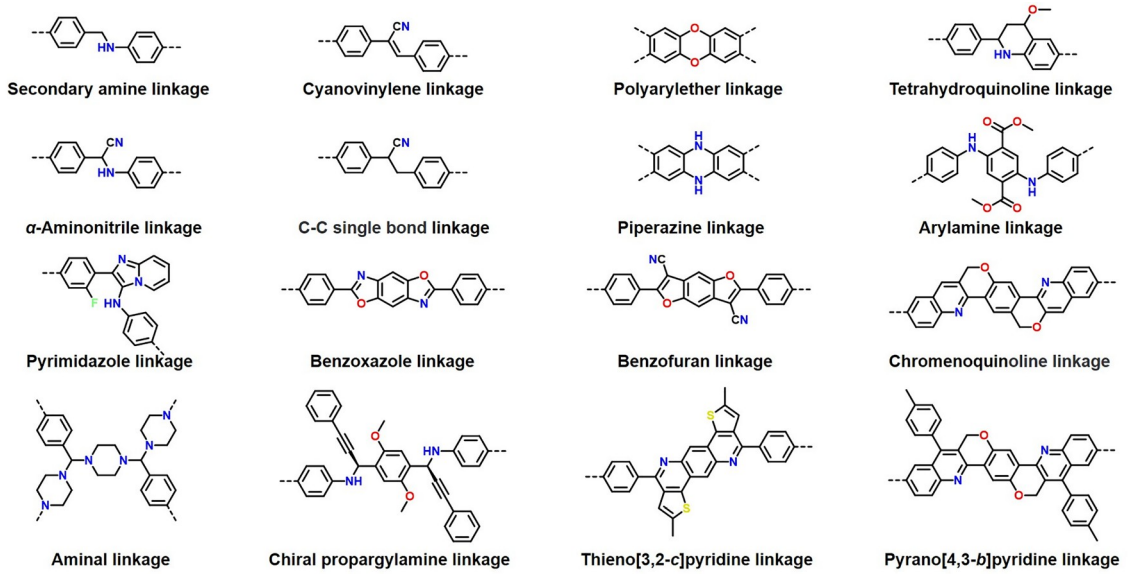

Figure 6 Chemical linkages developed in China (color online).

bon double bond formed by Knoevenagel condensation was successfully developed as linkages for the construction of COFs, exhibiting significant improvements in stability and electron communication. To date, several families of COFs reticulated by cyano-substituted vinylene or unsubstituted vinylene linkages have been successfully developed.

In 2016, the first example of olefin-linked COF, 2DPPV, was created by Zhang and coworkers [30] through Knoevenagel condensation of 1,4-phenylene diacetonitrile and three armed aromatic aldehydes through activating α-carbon atoms of cyanostilbene moieties in the presence of base catalyst. The C_2 symmetric 1,4-phenylene diacetonitrile (PDAN) as a key monomer was subsequently used for the construction of other olefin-linked COFs. For example, In 2019, Wang *et al*. [31] designed a 2D vinylene-linked COF using porphyrin muti-aldehyde units and PDAN as building blocks. Zhao and coworkers [120] utilized PDAN for the Knoevengel condensation with (2,4,6-tris(4-formylphenyl)-1,3,5-triazine (TFPT) and successfully synthesized a vinylene-linked COF. Importantly, Cao and coworkers [144] achieved the first synthesis of olefin-linked 3D COF by Knoevenagel condensation between the elaborately designed saddle-shaped aldehydes and 1,4-phenylenediacetonitrile. By combining reversible Knoevenagel condensation with irreversible cyanide migration and oxidative cyclization, Gu and coworkers [131] reported the synthesis of benzofuran-linked 2D COFs by connecting salicylaldehyde derivatives and acetonitrile-based building blocks. Cui and coworkers [145] synthesized the chiral COFs linked by the C–C single bond *via* the reduction of olefin-linked COFs by $NaBH_4$. Recently, Qiu and coworkers [146] utilized the C_3 symmetric 1,3,5-phenylene for the reaction with naphthalene-2,6-dicarbaldehyde or 2,2′,2″-(benzene-1,3,5-triyl)triacetonitrile and successfully synthesized the cyanovinylene-linked COFs (donated as NDA-TN and BDA-TN). Using a similar strategy, they also reported a triazine-based cyanovinylene-linked COF termed BTA [147].

In comparison to a cyanovinylene linkage, an unsubstituted vinylene linkage, owing to its higher geometric symmetry and less steric interference, seems to be more favorable to creating highly crystalline C=C linked COFs. Based on this knowledge, Zhang and coworkers [148] used 3,5-dicyano-2,4,6-trimethylpyridine (DCTMP), whose electron-deficient characters make it easy to generate carbon anions at its three arylmethyl carbon atoms in the presence of organic bases, to construct COFs with unsubstituted vinylene linkages by Knoevenegal condensation.

To generate COF with porous graphene analog, embedding electronegative heteroatoms into aromatic rings might be an efficient tool to generate enough electron-deficient character for activating the attached methyl carbons and facilitating Knoevenegal condensation. Zhang *et al*. have paid great effort to develop a series of vinylene linkage COFs with 1,3,5- trimethyl-2,4,6-tricyano phenyl (TCM) [149], 2,4,6-trimethyltriazine [150,151], DCTMP [152], tricyanomesitylene [153], and 2,2′,6,6′-tetramethyl-4,4′-bipyridine [154] as key monomers.

Similarly, Jiang and coworkers [155] synthesized the unsubstituted vinylene-linked COF, namely TM-TPT-COF by the reticulation of the two triazine monomers, 2,4,6-trimethyl-1,3,5-trizaine (TM) and 1,3,5-tris-(4-formylphenyl)-triazine (TPT). Zhang and coworkers [156] conducted an aldol condensation between 2,5-dimethylpyrazine (PZ) and 1,3,5-triformylbenzene (TFB) to yield a vinylene-linked COF using benzoic anhydride as acidic catalyst.

For ionic vinylene-linked COFs, the incorporation of multiple functions into a COF network represents a highly efficient strategy for the integrated and extended applications of COF materials. Zhang and coworkers [157] developed a concise approach to acquire 2D ionic vinylene-linked COF structures, in which a cationic monomer 2,4,6-trimethylpyridium was used. Along this line, they successfully synthesized the first example of ionic vinylene-linked 2D COFs.

Other linkages. In 2019, Fang and coworkers [158] synthesized polyarylether-linked COFs *via* nucleophilic aromatic substitution reactions from *ortho*-difluoro benzene and catechol-building units. The stability of polyarylether-linked COFs even can outperform zeolite materials. Recently, Huang and coworkers [159] reported the construction of piperazine-linked COFs *via* the nucleophilic substitution reaction between octaminophthalocyanines and hexadecafluorophthalocyanines.

2.3.3 New topologies

The construction of COFs with new topologies is an important way to enrich the structural diversity of COFs. Based on the synthesis of building blocks with higher symmetry and the combination of building blocks with various symmetry, numerous COFs with new topologies were discovered by researchers in China (Figure 7).

New topologies of 2D COFs. Heteropore COFs represent a class of interesting family in COFs, which were created by Zhao's group. In 2014, Zhao and coworkers [121] achieved the synthesis of a dual-pore COF *via* the condensation between D_{2h} symmetric 4,4′,4″,4‴-(ethene-1,1,2,2-tetrayl)-tetraaniline and C_2 symmetric terephthalaldehyde. This dual-pore COF possesses a novel and unique **kgm** topology. In 2019, they also constructed aminal-linked COFs with **cpi** topology [138]. They continuously enriched this family through the successful synthesis of triple-pore COFs [126] and tetrad-pore COFs [160], which greatly increased the structural complexity of COFs.

Recently, Cui and coworkers [166] achieved the construction of 2D COFs with unprecedented **cem** topology. The key is the use of a pyrrole-based monomer with pseudo-

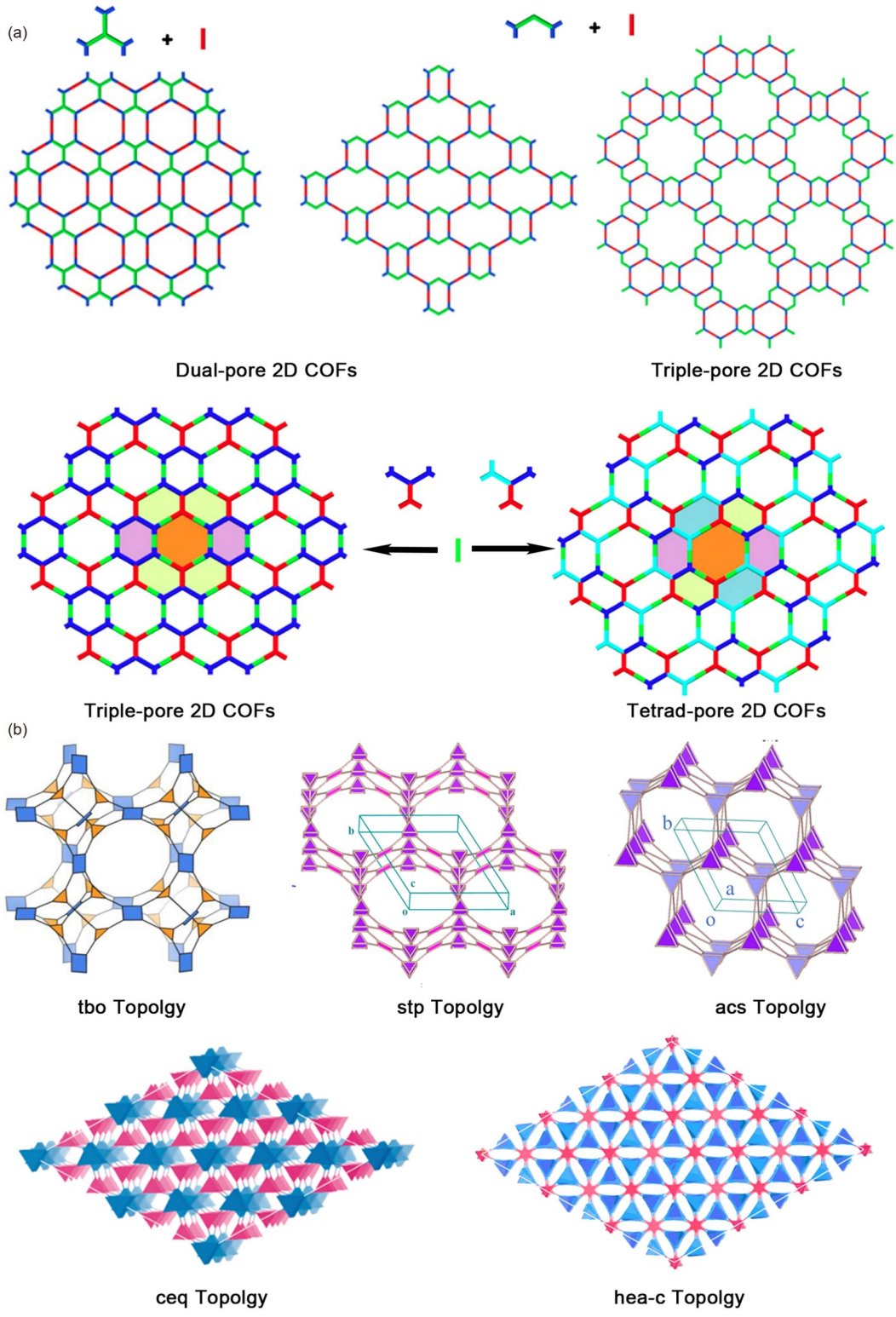

Figure 7 Some New topologies developed in China [126,160−165] (color online).

fivefold symmetry. These COFs also possessed heteropore structures.

New topologies of 3D COFs. The combination of building blocks with different symmetries is a powerful tool to discover COFs with new topologies. In 2016, Wang and coworkers [122] synthesized a novel 3D pyrene-based COF with **pts** topology from the combination of tetrahedral (T_d symmetry) and rectangle (C_2 symmetry) building blocks. Be-

sides, 3D COFs with new topologies can also be constructed through the combination of 2D building blocks. In 2018, Zhong and coworkers [167] successfully synthesized two 3D COFs with **ffc** topology by the condensation between D_{2h} symmetric 4,4′,4″,4‴-(ethene-1,1,2,2-tetrayl)tetraaniline and C_3 symmetric monomers. In 2020, Cui and coworkers [161] also constructed two novel 3D COFs with **tbo** topology by the condensation between C_4 symmetric porphyrin-based tetrotopic amine and C_3 symmetric aldehydes.

Creating the monomer with higher symmetry is important to enrich the topology of 3D COFs. In 2020, Fang and coworkers [162] reported the first synthesis of a monomer with D_{3h} symmetry, that is 2,3,6,7,14,15-hexakis(4-formylphenyl)triptycene. Taking advantage of the triptycene scaffold, this monomer can serve as triangular prismatic nodes. Accordingly, they constructed the first 3D COF with **stp** topology. The density of this 3D COF is the lowest among crystalline materials reported so far (0.108 g cm^{-3}). By applying this triptycene-based monomer, 3D COFs with **ceq** topology [163,164] and **hea** topology [165] were also reported. Lately, Zhang and coworkers [168] achieved the synthesis of building blocks with unprecedented eight valencies. They synthesized 3D COFs with **pcb** topology by using the 8-connected porphyrin-based aldehydes to react with C_2 symmetric monomers.

Note that not all topologies of COFs can be predicted according to the combination of monomers with certain symmetries. Wang and coworkers [129] discovered a rare **lon** topology of LZU-111. They obtained this important structural information from the single-crystal diffraction data of the COF. Notably, LZU-111 possessed a chiral space group. Recently, Wang and coworkers [169] achieved the synthesis of a 3D COF with unprecedented **ljh** topology through steric control. In this work, the replacement of methoxyl groups by phenyl groups in the C_2 symmetric building block would change the topologies of corresponding COFs from **pts** to **ljh**.

2.3.4 Chiral COFs

Chiral COFs, abbreviated as CCOFs, are highly attractive for their potential in various applications, such as asymmetric heterogeneous catalysis, chiral separation, chiral sensing, and chiral optics. However, it is a great challenge to construct CCOFs. The reason may lie in the intrinsic mismatch between the symmetry for crystalline structure and asymmetry for chiral moieties (Figure 8).

Strategy development. In the beginning, the synthesis of CCOFs relied on the post-synthetic strategy which incorporated the chiral moieties into achiral COFs [123]. Wang and coworkers [170] achieved the direct construction of CCOFs from a chiral building block. The elaborately designed chiral monomer integrated the symmetric and robust benzo[*d*]imidazole moiety and the chiral pyrrolidine pedant, which is the key to obtaining highly crystalline CCOFs. By following this design principle, they continuously established the library of CCOFs *via* divergent synthesis [171]. Chiral pedants, which contained hydrogen-bonding moiety, secondary amine, tertiary amine, or guanidine, can be facilely embedded into benzo[*d*]imidazole-based building blocks. Eight CCOFs with high crystallinity were constructed for screening their catalytic properties in asymmetric amination reactions.

Regarding the expansion of the library of CCOFs, Cui and coworkers [172] also proposed the multivariate approach for the construction of chiral 2D COFs. First, they developed a series of 1,3,5-tris(4-aminophenyl) benzene (TFB)-based chiral building blocks which were modified by chiral pyrrolidine or imidazolidine moiety. They synthesized a series of binary CCOFs by the condensation of TFB with dimethoxyterephthalaldehyde. The densities of TFB-based chiral monomers could be tuned by a three-component strategy by mixing with 2,4,6-tris(4-aminophenyl)benzene. Ternary CCOFs were utilized for screening asymmetric α-aminooxylation, asymmetric Aldol reactions, and asymmetric Diels-Alder reactions, which showed comparable or even superior performance in reaction selectivity in terms of stereoselectivity and diastereoselectivity when compared with their homogeneous counterparts.

The chirality of CCOFs in the aforementioned strategies originated from the molecular chirality of monomers. In 2018, Cui and coworkers [173] developed the "chiral induction strategy" for the construction of CCOFs. By using enantiopure 1-phenylethylamines as the chiral additives, the single-handedness in threefold-symmetric tris(N-salicylideneamine) cores in these CCOFs could be established. In 2020, Dong and coworkers [135] achieved the catalytic asymmetric synthesis of CCOFs. With the presence of a catalytic amount of copper salt and chiral ligands, CCOFs could be constructed *via* asymmetric A^3 coupling reaction from multitopic aldehydes, multitopic anilines, and phenylacetylene.

Structural diversity. The incorporation of privileged chiral scaffolds, such as TADDOL, Salen, and BINOL, is an important way to enrich the type of CCOFs and further explore their functionalities. In 2016, Cui and coworkers [174] successfully introduced the TADDOL skeleton into COFs. They synthesized the enantiopure TADDOL-derived tetraaldehydes. Possessing the semirigid backbone, these tetratopic TADDOL-based monomers could react with flexible 4,4′-diaminodiphenylmethane *via* the Schiff-condensation to produce corresponding chiral TADDOL-based COFs. In 2018, they [175] reported the construction of 3D CCOFs for the first time. 3D TADDOL-based COF with imine linkage was prepared from the condensation between enantiopure TADDOL-derived tetraaldehydes and tetra(4-anilyl)methane. After the post-synthetic oxidation for imine-linked

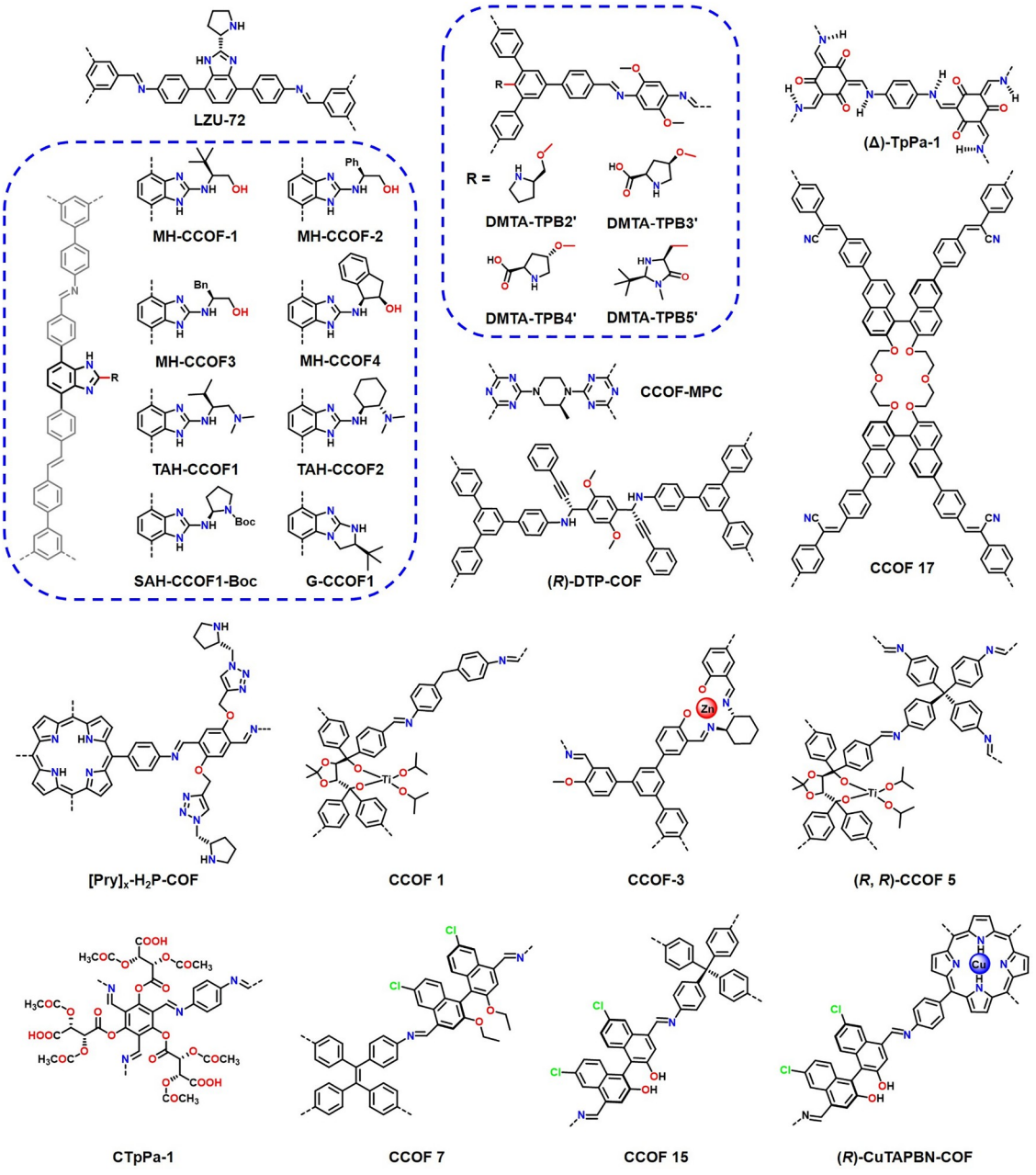

Figure 8 Chiral COFs developed in China (color online).

TADDOL-based 3D COF, the corresponding amide-linked 3D TADDOL-based COF could be obtained with retaining crystallinity, permanent porosity, and enhanced chemical stability. Both COFs can be used as chiral stationary phases for high-performance liquid chromatography to separate racemic alcohols. This case represents the first application of COFs in high performance liquid chromatography (HPLC).

In 2016, Yan and coworkers [176] achieved the one-pot construction of CCOFs from a tartaric acid-functionalized monomer with diamines. The chiral monomer was prepared from the reaction between 1,3,5-triformylphloroglucinol and enantiopure (+)-diacetyl-L-tartaric anhydride. These COFs possessed abundant hydrogen-bonding sites, which could increase the interlayer interaction for enhancing crystallinity. Besides, they also applied these COFs into capillary columns for chiral gas chiral chromatography.

Chiral Salen-based COFs were reported by Cui and coworkers [177] in 2017. By exploiting the enantiopure 1,2-diaminocyclohexane as the chiral source, the chiral zinc-coordinated Salen scaffold could be formed between the condensation of chiral 1,2-diaminocyclohexane and trisalicylaldehydes when hydrate $Zn(OAc)_2$ was the catalyst. Notably, a series of Salen-based CCOFs could be obtained by the alteration of the zinc ions with other active metal species,

such as Cr, Co, and Mn cations, *via* one-step or two-step ion exchange. These chiral Salen-based COFs could serve as excellent heterogeneous catalysts for asymmetric cyanation of aldehydes, Diels-Alder reaction, alkene epoxidation, epoxide ring-opening, and other cascade reactions.

In 2017, Dong and coworkers [178] synthesized a C–N bond-linked CCOF through the copolymerization between *S*-(+)-2-methylpiperazine and cyanuric chloride. Continuously, they reported a porphyrin-based homochiral covalent organic framework through the C–N coupling reaction between *S*-(+)-2-methylpiperazine and copper-coordinated tetrabromophenolphthalein [179]. These CCOFs could serve as robust supports for metal nanoparticles to achieve asymmetric catalysis.

In 2019, Cui and coworkers [180] first applied the enantiopure 1,1′-binaphthol (BINOL) derivative as the chiral source to achieve the synthesis of CCOFs. Recently, they [181] also achieved the construction of 3D BINOL-based CCOFs and explored their catalytic application in asymmetric acetalization of 2-aminobenzamide and aldehydes. In 2021, Dong and coworkers [182] reported the construction of CCOFs integrated by Cu-porphyrin and (*R*)-BINOL moieties. These CCOFs were applied to synthesize key drug intermediates, namely (*S*)-CIK, under the irradiation of visible light (λ=420 nm) and even sunlight. In 2022, Cui and coworkers [145] successfully incorporated the chiral crown ether into the framework of olefin-linked COFs. The chirality of the crown ether monomer was controlled by two BINOL moieties. Possessing high stability and homochirality, these COFs were packed in HPLC and GC columns for the separation of a wide range of racemic compounds and showed excellent performance [183].

2.4 Covalent triazine frameworks

Since the fabrication of CTFs *via* the ionothermal method in 2008 [19], broad interests have been triggered in exploring this kind of material in diversifying their skeletons and thermal/electric/optic properties [184–189]. The vast organic library of versatile multiarmed monomers and cross-linking methodologies afford an unlimited potential for engineering the structures and tailoring the properties of the CTFs' π-conjugated networks [190]. Elaborate tuning on the monomer structures and reaction procedures/parameters leads to effective integration of the alternating arrangement of the triazine-fused units within the skeleton towards task-specific applications.

Structure engineering of CTF materials, like monomer design, controllable functionalization, and advanced synthesis strategies, is crucial to tune the properties, such as porosity [19], crystallinity [191,192], morphology [193], and defect of the as-afforded materials, which, in turn, affect their performance in task-specific applications. Considering the pivotal role of CTFs' synthesis method in the structure-property-application, it is highly required to summarize and compare the advantages and disadvantages of different synthesis methods, which can guide monomer design and synthesis pathway selection to achieve far-reaching applications.

Here, CTFs were defined as materials constructed starting from monomers with no triazine units being involved [194]. So far, the involved synthesis methods contain ionothermal synthesis method [19], superacid (trifluoromethanesulfonic acid)-catalyzed method [195], phosphorus pentoxide (P_2O_5)-catalyzed direct condensation of aromatic amides [196], and low-temperature polycondensation method [197] (Figure 9). Firstly, we survey the development of different types of methods. We also take a critical look at the ability to design CTFs at the atomistic level, as considered from the viewpoint of individual functions; then challenges in state-of-the-art systems and potential opportunities to extend the boundary of this promising material and the synthesis method will be discussed.

2.4.1 *Synthesis of covalent triazine frameworks*

Ionothermal method. The classic, which was also the pioneering work related to CTF materials, was reported by Thomas and coworkers [19]. In 2008, the $ZnCl_2$-promoted ionothermal procedure was first demonstrated by using terephthalonitrile as the starting material to afford CTF-1. $ZnCl_2$ (melting point=283 °C) was used as both solvent and catalyst in its molten state for the trimerization of nitrile groups to form triazine units. For this strategy, the function of CTFs is limited to the structure of monomers, ionothermal temperature (400–700 °C), loading amount of $ZnCl_2$ (1–10 equivalents), and reaction time (24–72 h). This method applies to a variety of aromatic nitrile monomers by virtue of the good catalytic activity of $ZnCl_2$ for the trimerization reaction, whether electron-deficient or electron-rich monomers. Other reaction parameters including reaction temperature, loading amount of $ZnCl_2$, and reaction time could influence the quality of the as-afforded CTF products (*e.g.*, surface area, porosity, crystallinity, nitrogen content, conductivity, vacancy ratio). Because of the advantages like the easily available and cheap catalyst, good catalytic activity towards most aromatic nitrile monomers (both aromatic and aliphatic ones), high surface area/porosity of the products [198], good conductivity, and abundant defects being created, the ionothermal procedure had been widely deployed for the preparation of materials used for gas adsorption and electrochemical field. However, predesigned structures are often unavailable due to the ionothermal approach. The loss of elements like nitrogen and fluorine would happen due to $ZnCl_2$-involved decomposition. For example, the low fluorine content in perfluorinated CTFs (F-CTFs) [188] and low nitrogen content in CTF-DCBP [19],

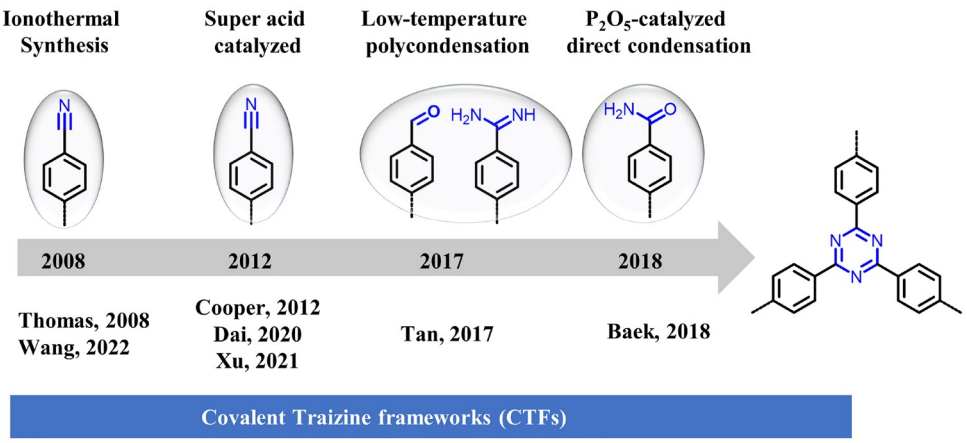

Figure 9 The reported synthesis methods of CTFs (color online).

may be due to C–F bond cleavage or a significant amount of triazine cleavage. Additionally, other challenges also existed, including inert reaction conditions (handling in glovebox and pyrex tubes) due to the hygroscopic nature of $ZnCl_2$, a required large amount of $ZnCl_2$ (more than equimolar), high temperature (≥400 °C), explosion risk due to the formation of gaseous products, unavoidable residual Zn species, semicrystalline or amorphous nature of the products, and partial carbonization of the as-prepared CTFs under the high reaction temperatures (as black powder). Recently, a low-temperature ionothermal synthesis method for CTFs was developed by Wang's group [199]. They used a ternary NaCl-KCl-$ZnCl_2$ eutectic salt mixture with a melting point of approximately 200 °C as catalyst and solvent. This temperature is lower than the melting point of pure $ZnCl_2$, thus providing milder salt-melt conditions. These conditions facilitated the polycondensation process, while avoiding carbonization of the polymeric backbone. The resulting CTF-ES_{200} exhibited enhanced optical and electronic properties, and displayed remarkable photocatalytic performance in the hydrogen evolution reaction.

Superacid-catalyzed method. In 2012, both Dai's group [195] and Cooper's group [200] found the super Brønsted acid (trifluoromethanesulfonic acid (CF_3SO_3H)) with strong acidity could be used as a catalyst to promote the trimerization of cyano groups for the construction of triazine ring (Figure 10). This method can be carried out under relatively mild conditions (0–25 °C or microwave treatment at 110 °C). Therefore, CTFs with no carbonization, visible light absorption, and adjustable bandgap positions can be obtained, which makes the potential application in photocatalysis possible. Interestingly, interfacial polymerization had been developed based on this strategy by Xu and coworkers [185,201] to prepare the few-layer CTF nanosheets, leading to good performance as a conductor or electrodes. However, the crystallinity and surface area of the CF_3SO_3H-derived products are often lower than those of ionothermal method-derived products due to the lower polymerization degree. Recently, great progress was achieved by Dai and coworkers [192] and Xu and coworkers [191]. Dai and coworkers [192] found highly crystalline and higher BET surface area CTF-1 from TPN catalyzed by strong Brønsted acids could be obtained *via* a transformation strategy from a staggered AB to eclipsed AA stacking mode. High fluorine content CTFs was achieved *via* the trimerization of fluorinated aromatic nitrile monomers. The distinguishing difference is they used a much higher temperature (250 °C) than previous work (0–25 °C or microwave treatment at 110 °C). The higher temperature may lead the polymerization reaction more complete. Xu and coworkers [191] demonstrated a scalable microwave-assisted synthetic strategy to successfully prepare a series of highly crystalline and semiconducting CTFs within 20 min. Another appealing factor of the superacid-catalyzed method is nonporous CTF-based membranes with efficient gas separations ability can be prepared, though an excessive amount of strong Brønsted acids is needed and the film is amorphous [195]. However, high temperature (250 °C) or microwave-assisted treatment is necessary if attempting to obtain high crystallinity and high specific surface area CTF materials. Besides, the use of corrosive and high-cost acid catalysts (trifluoromethanesulfonyl) makes it a great challenge for the practical application.

P_2O_5-catalyzed method. In 2018, Baek and coworkers [196] reported that CTFs could be synthesized by phosphorus pentoxide (P_2O_5)-catalyzed direct condensation of aromatic amides to form a triazine ring. Firstly, P_2O_5 catalyzed the dehydration of amides to nitriles; secondly, the triazine ring was obtained by the trimerization of nitriles. This represented the efforts to construct a CTF skeleton from non-nitrile monomers. However, it still needs a high temperature (350–400 °C) to obtain crystalline structure, so partial carbonization of the as-prepared CTFs under the high reaction temperatures is unavoidable.

Low-temperature polycondensation method. Another

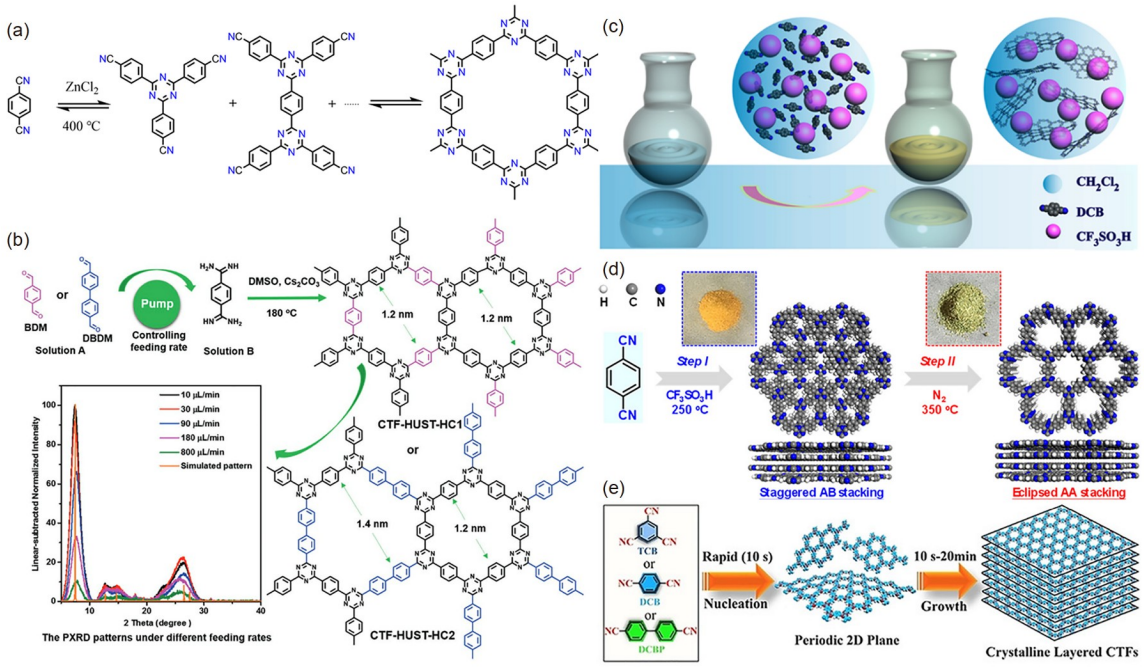

Figure 10 Synthesis of CTF-1 obtained (a) *via* the $ZnCl_2$-catalyzed ionothermal procedure [19], (b) *via* the low-temperature polycondensation method (control the feeding speed of aldehyde monomer) [203], (c) *via* polymerization at the interface of CH_2Cl_2/CF_3SO_3H [201], (d) *via* two-step transformation strategy in the presence of CF_3SO_3H [192], (e) *via* microwave-assisted strategy in the presence of CF_3SO_3H [191] (color online).

strategy to construct the CTF skeleton from non-nitrile monomers was developed by Tan and coworkers [197] in 2017. They found CTFs with layered structures could be prepared by condensation reaction between aromatic aldehydes and aromatic amidines, which underwent Schiff base formation and Michael addition successively. This reaction was conducted under the relatively mild condition: dimethyl sulfoxide (DMSO) as the solvent; Cs_2CO_3 as the base; reaction temperature of 120 °C with no requirement for the inert atmosphere. The obtained CTFs show a semicrystalline nanoporous structure and exhibit good photocatalytic activity. To improve the crystallinity of the CTF products, strategies like *in-situ* oxidation of monomer [202] and controlling the feeding speed of monomer [203] were developed. Aromatic benzylic alcohols [202,204], benzylic amines [205], or aromatic benzyl chloride [206] would be oxidized by DMSO slowly to release aldehyde *in-situ*, which then reacted with the aromatic amidines to form crystalline CTFs. Crystalline CTF structure also could be obtained by controlling nucleation speed, crystal growth rate, and reaction kinetics by changing the feeding rate of the aldehyde monomers [203]. Especially, Tan's group [207]. reported two 3D crystalline CTFs with ctn topology synthesized by this polycondensation approach using T_d symmetrical tetrahedral amidine hydrochloride and aldehyde The distinguishing feature of this strategy is the obtained CTFs are yellow, which indicates no carbonization at the mild temperature. Also, this strategy involved two kinds of monomers, and one kind of monomers could be aldehyde/benzylic alcohols/benzylic amines or aromatic benzyl chloride, and so on. This method enriched the toolbox of building blocks and extended the structural design and diversity.

2.4.2 *General advantages and disadvantages*

As mentioned above, four different classes of synthesis methods exist (Table 1), and there is no one-size-fits-all solution; it can therefore be challenging to choose the right type of method for a target structure.

Here, we survey some of the advantages and disadvantages of different types of methods. We also take a critical look at the potential to improve the existing method, as considered from the viewpoint of individual characteristics. An important challenge is to apply these approaches to practical systems, where it is invariably necessary to optimize many parameters and avoid undesirable properties. For industrial applications, the primary concerns are functionality and operational costs rather than the materials themselves. The functionality is reflected by the structure (the choice of monomer; the crystallinity; the defects; the porosity) of CTFs materials. The operational costs are reflected by the cost of monomers and catalysts, as well as the realistic feasibility of one kind of method (temperature, high pressure, explosion, toxicity…).

Crystallinity. Most of the reported CTFs are amorphous or semi-crystalline due to their ultra-strong bonds. In highly dynamic condensation reactions, the stronger the bonds are,

Table 1 General advantages and disadvantages of different synthesis methods

Method	Choice of monomers	Reaction condition	Crystallinity	Structural integrity
Ionothermal method	Limited	Harsh	Moderate to good	Partial carbonization
Super acid-catalyzed method	Limited	Relatively mild to harsh	Amorphous, moderate to good	Moderate to good
P_2O_5-catalyzed method	Limited	Harsh	Moderate to good	Partial carbonization
Low-temperature polycondensation	Broad	Relatively mild	Moderate	Good

the more difficult it is to form ordered structures. The crystalline structure shows much better performance in the photoelectric field; also, well-defined molecular and porous structures are highly desired for making full use of the features and understanding the structure-property relationship. Therefore, high crystalline CTFs are highly desirable [203]. Until now, the reported crystalline CTFs structure is very rare. High-temperature (400 °C) and long-time (40 h) reactions with excessive molten zinc chloride ($ZnCl_2$) [19,198] and phosphorus pentoxide (P_2O_5) [196] as catalysts can produce crystalline CTFs but would result in partial carbonization (black appearance) and residue of catalysts.

The polycondensation of amidine and aldehyde or benzylamine yields crystalline CTFs. Tan's group developed an *in-situ* oxidation strategy to synthesize crystalline-ordered CTFs. Alcohols can be gradually oxidized to aldehydes in the presence of air in DMSO. Aldehyde monomers as intermediates were gradually formed through the controlled oxidation of alcohol monomers, which played a key role in the control of the nucleation rate. According to this strategy, a series of crystalline CTFs, *i.e.*, CTF-HUST-C1, CTFHUST-C5, and CTF-HUST-C6, were prepared. These structures show better photocatalytic performance due to the high crystallization [202,204]. This strategy was extended to benzylic amines [205] or aromatic benzyl chloride [206] by their group. Another way to improve the crystallinity of CTFs based on a low-temperature polymerization approach was controlling the reaction kinetics including changing the feeding rate of aromatic aldehydes monomer. Owing to the better separation of photogenerated electron-hole pairs and charge transfer, the obtained highly ordered CTF-HUST-HC1 has superior performance in the photocatalytic removal of nitric oxide (NO) [203]. Two 3D crystalline CTFs can be synthesized by this polycondensation approach using T_d symmetrical tetrahedral amidine hydrochloride and aldehyde, which is the first report of 3D crystalline CTFs [207]. Usually, the crystallinity of CF_3SO_3H-derived CTFs is very low. But recently, Dai's group [192] and Xu's group [191] reported that CTFs materials with very good crystallinity could be prepared at higher temperatures (250 °C) or under microwave-assisted conditions. The full width at half maxima (FWHM) of CTF-DCB and CTF-DCBP are 0.44° and 0.4° respectively, which is almost the best results till now.

In summary, most of the reported CTFs are still amorphous or semi-crystalline; crystalline CTFs can be only prepared in a special condition or by special monomers. It may be caused by the irreversibility of the triazine-form polymerization reactions in the reaction condition. To overcome this issue, one of the strategies is to conduct the reaction at a high temperature (400 °C for the ionothermal method and P_2O_5-catalyzed method; 250 °C for the superacid catalyzed method), and encouraging results by Xu and coworkers demonstrated the crystallinity of CTFs is even comparable with most of imine COFs. Another strategy is controlling the monomer concentration in the reaction system, which had been proved to be practicable in the low-temperature polycondensation method. Tan's group [208] reported one kind of crystalline CTF (CTF-Bpy) prepared *via* the controlling feed rate strategy, and it's FWHM is about 0.76°. However, most of CTFs' FWHM are still very high (1.5°–2.5°). Inspired by Xu's and Dai's work, we speculate that better crystallinity can be achieved at a much higher temperature; however, the decomposition of solvent (*e.g.*, DMSO) also needs to be considered at high temperatures, which may cause both side reactions and safety problems.

Designability. In principle, the desired function of CTFs can be accomplished by designing and constructing CTFs at the atomic level with an adequate understanding of structure-property relationships. In practice, the major challenges including the choice of monomers, and whether the structure is well established or not (crystallinity) still limited the rational design of CTFs.

Considering the choice of monomers, the ionothermal method, superacid-catalyzed method, and P_2O_5-catalyzed method are all based on only one kind of monomer (aromatic nitriles/aromatic amide) (Figure 11), so the diversity of CTFs structures can be defined as the kinds of monomers.

On the contrary, the low-temperature polycondensation method is based on aromatic amidines/aromatic aldehydes, so the diversity of CTFs structures can be multiplied significantly (Figure 11). Typically, amidines are prepared from aromatic nitriles. However, it is tedious and difficult for the preparation of some aromatic amidine. On the other hand, aldehyde monomers are readily available and widely used in the preparation of COFs.

The function-orientated design of CTFs is very important for their applications. Especially, the conjugated network endowed CTFs with great potential in the photoelectric field, *e.g.*, photocatalytic water splitting. However, most of the

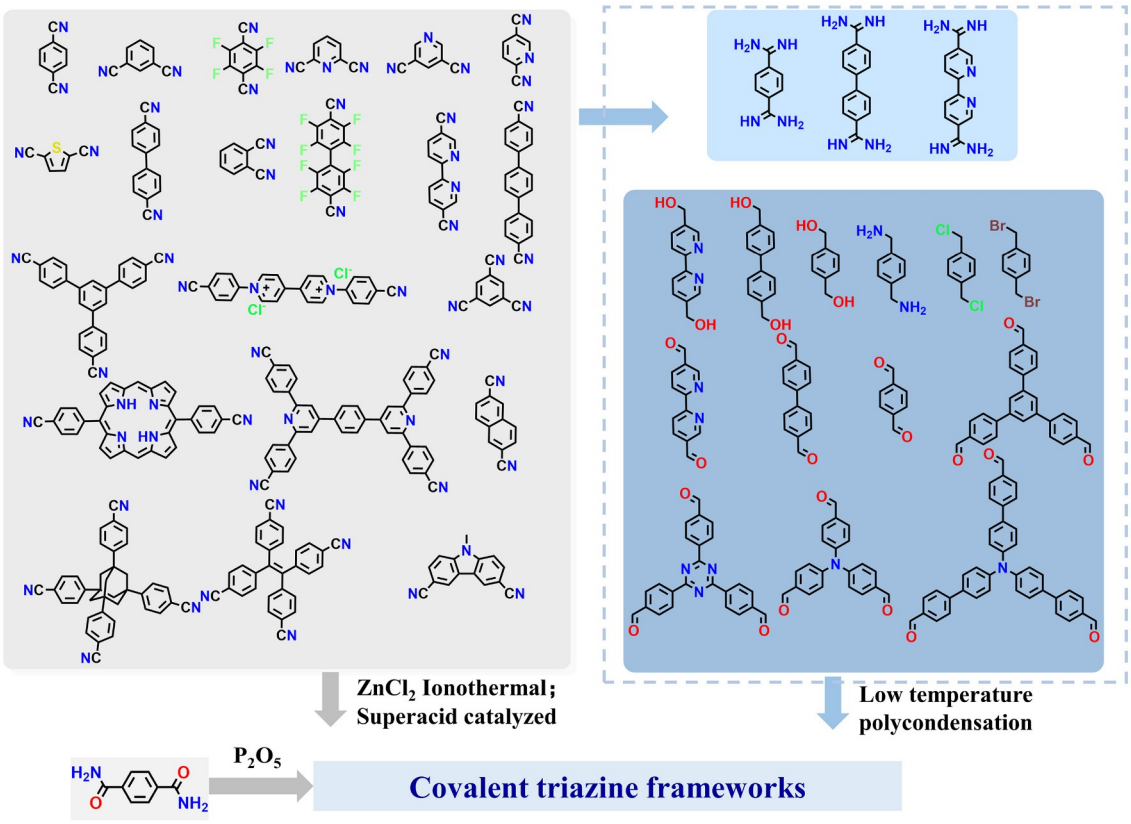

Figure 11 Representative monomer structures in the construction of CTFs (color online).

CTFs did not show satisfactory performance. In principle, a rational design of the CTFs structure is needed to enhance the exciton separation efficiency. For example, the D-A structure had been proved an efficient approach (Figure 12). The harsh condition of the ionothermal method, P_2O_5-catalyzed method could damage the intrinsic structure of CTFs, and the rational design of CTFs structure is a great challenge. On the contrary, this is much easier for the superacid-catalyzed method. Li and coworkers [209] introduced benzothiadiazole and thiophene moieties into CTFs as electron-withdrawing and electron-donating units, respectively, by a sequential polymerization strategy. The resulting hybrids exhibited much improved charge-carrier-separation efficiency. An H_2 evolution rate of 6.6 mmol g^{-1} h^{-1} was measured for the optimal sample under visible-light irradiation (λ >420 nm), which is far superior to that of the most reported conjugated-polymer photocatalysts. However, the chemical structures of the resulting materials by copolymerization from two kinds of monomers are ambiguous, so it is difficult to get a clear structure-activity relationship. Tan's group [211] also developed a series CTFs with a D-A structure. They found D-A1-A2 system can not only boost charge separation but also suppress charge recombination owing to the cascade energy levels of the comprised units and large charge delocalization structures [210]. Therefore, an apparent quantum yield of up to 22.8% at 420 nm was achieved, and the highest hydrogen evolution rate can be up to 966 μmol h^{-1} (19.3 mmol g^{-1} h^{-1}) under visible light irradiation. However, the CTFs' structure is still not very clear (is it a homopolymer or just a mixture of two kinds of polymer?).

Processability. It is uncommon for as-synthesized CTFs materials to be used in applications directly; they are typically insoluble and nonmelted powders. So, processing CTFs into a specific form, such as a pellet, a thin polymer membrane, or a surface-deposited film, are very important. The processability is therefore an important property when considering the preparation method [212]. Typically, monolithic materials were obtained by ionothermal synthesis, which may be useful for electrochemical, and gas adsorption-related applications but not suitable for photoelectric-related applications [19]. Dai's group [195] first presented a strategy for the direct facile synthesis of triazine-framework-based porous membranes for CO_2 separation through superacid-catalyzed cross-linking reactions in 2012 (Figure 13a). A solution of 4,4′-biphenyldicarbonitrile in CF_3SO_3H was poured into a flat glass dish and allowed to spread into a thin layer. A soft coating film was successfully formed after heating at 100 °C for ~20 min. The same group also reported robust CTF membranes with ionic functionalities or con-

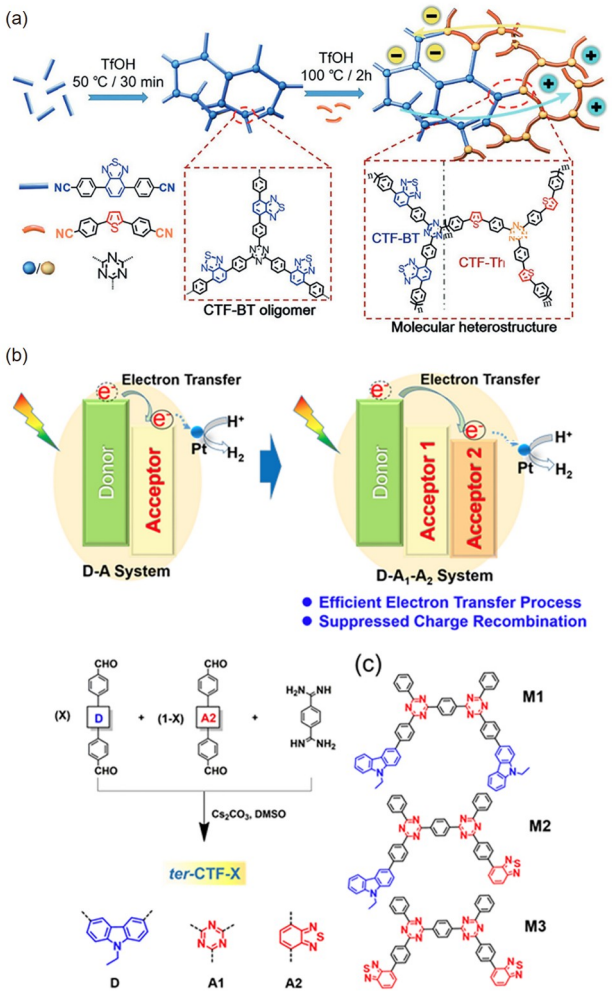

Figure 12 Synthesis of CTFs with D-A structure. (a) Sequential polymerization strategy toward covalently connected CTF-BT/Th with molecular heterostructures [209]; (b) synthesis of *ter*-CTF-X with D-A1-A2 structure by low-temperature polycondensation approach [210] (color online).

taining fluorine/ether groups that could be fabricated *via* a sol-gel approach promoted by a superacid (FSO_3H) [213,214] (Figure 13b). Xu's group [201] reported that single-layer/few-layer CTF nanosheets can be synthesized *via* the trimerization of carbonitrile at the interface of dichloromethane and trifluoromethanesulfonic acid. Moreover, these nanosheets can be assembled into mechanically strong layered free-standing films *via* filtration. Unfortunately, the films prepared *via* the sol-gel approach are amorphous, and the films prepared and assembled *via* CTF nanosheets are noncompact.

Recently, Tan's group [31] reported an aliphatic amine-mediated interfacial polymerization strategy to prepare free-standing, semi-crystalline CTF film. The thickness and lateral size of the film can be easily regulated. Simple, scalable processing routes are still a great challenge for CTFs' preparation.

2.5 Supramolecular organic frameworks

Different from COFs and CTFs, SOFs are a kind of crystalline organic porous framework material linked by noncovalent force between small organic molecules, including van der Waals force like H-bonding interactions [20], halogen bonding interactions [21], ionic interactions [22] and so on. Compared with COFs and other POPs linked by covalent bonds, SOFs possess both nano porosity and good solubility. POPs are typically in a solid state and have the characteristics of intrinsic porosity, high stability, convenient synthesis, and post-modification. To attain intrinsic porosity, the precursors are usually rigid. As a result, conventional POPs are not soluble in both water and organic solvents. The construction of water-soluble POPs is expected to extend the investigations of their properties from the solid state to aqueous media to reveal a new structure-property relationship. Moreover, water-soluble POPs are expected to display some different and valuable characteristics, including controllable and scalable preparation, good processability, controllable interior post-modification, structural diversity, reversible guest adsorption and release, as well as potentially high biocompatibility [12,13], which should be important for

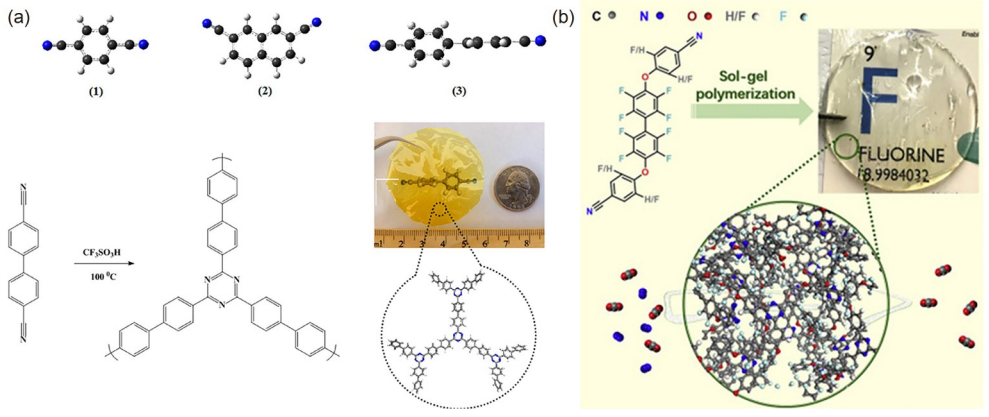

Figure 13 (a) Fabrication and photograph of flexible TFM-1 membrane from the trimerization of DCBP in CF_3SO_3H [195]; (b) synthetic route, structure, and picture of membrane F8TM-1 [214] (color online).

the development of biomaterials [13]. In the past decade, a few examples of water-soluble covalent organic frameworks have been reported [215]. Several kinds of water-soluble porous polymers have been developed, including SOFs [216], flexible organic frameworks (FOFs) [217] as well as supramolecular coordination polymers [218]. By broad definition, all these porous architectures can be regarded as water-soluble POPs. Among others, SOFs feature the utilization of hydrophobically driven encapsulation of cucurbit [8]uril (CB[8]) for homodimers of cationic aromatic units [216]. Since the first example of 2D monolayer SOF (**ml-SOF-1a**) was reported in 2013 from the co-assembly of triangular compound **1a** and CB[8] [219], a large number of SOFs has been constructed that display varying topologies and diverse functions, including photocatalysis, explosive sensing, cell imaging as well as drug delivery. Figure 14 summarizes the representative building blocks for the construction of 2D and 3D SOFs.

2.5.1 Self-assembly strategy and monomer design for SOFs

The periodic porosity of crystalline MOFs and COFs is crucially important for the maximization of many of their functions. Although in the past decades many water-soluble supramolecular polymers have been reported [220], a systematic exploration of their intrinsic porosity in solution, particularly in aqueous media, is not available. It is expected that the attainment of regular porosity for water-soluble supramolecular polymers could remarkably facilitate their guest adsorption-based functions or applications, especially for the creation of biocompatible materials. In principle, the strategy of multivalency related to rigid multitopic precursors or ligands for the generation of MOFs and COFs can also be applied to the design of water-soluble porous architectures. Nevertheless, there have not been examples of water-soluble MOFs and COFs that are prepared using established approaches for their solid-state counterparts. CB[8]

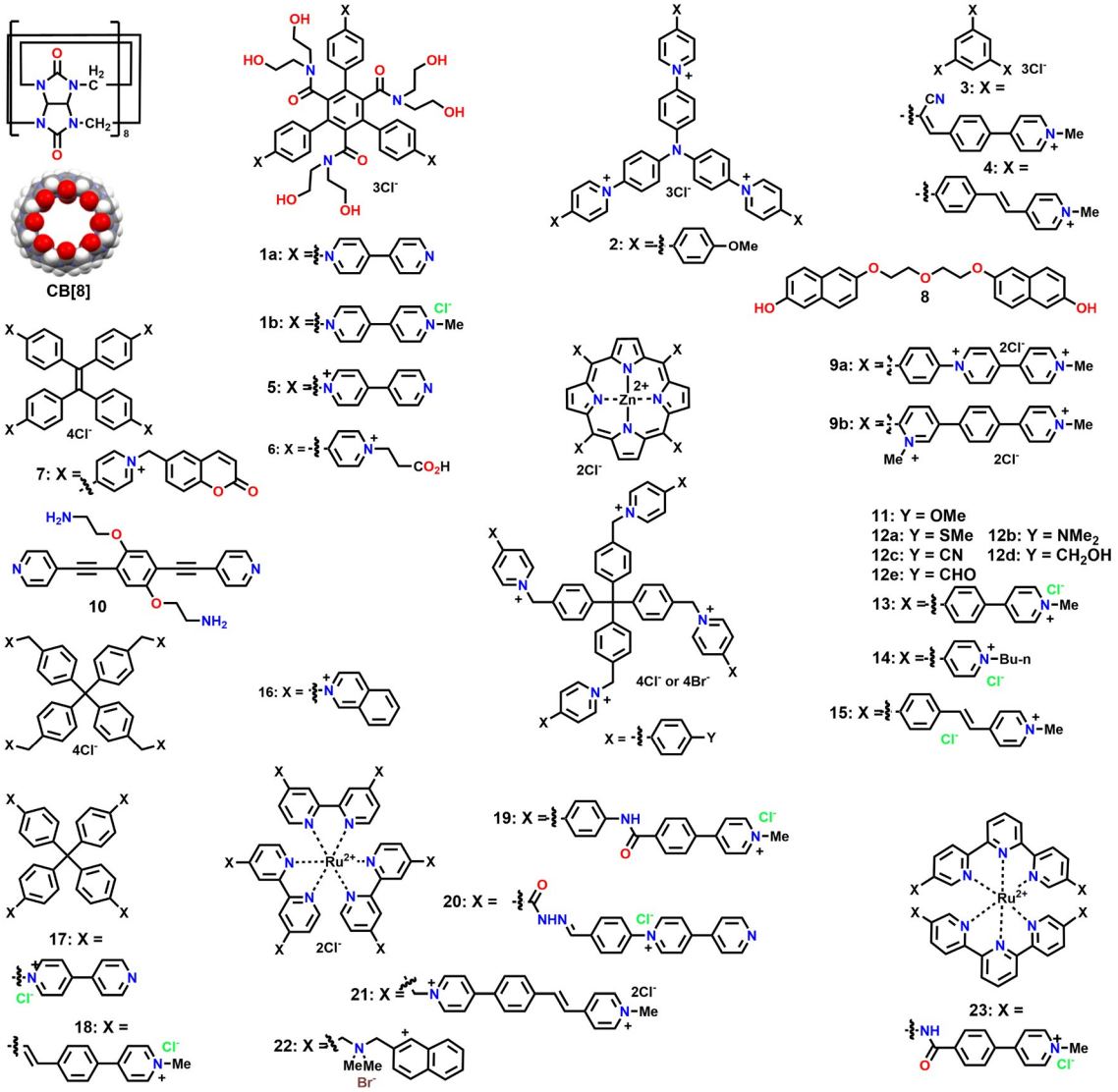

Figure 14 The chemical structure of CB[8] and multitopic building blocks **1**–**22** for the formation of 2D and 3D SOFs (color online).

encapsulation for hydrophobic aromatic homo- and heterodimers has been demonstrated as an efficient strategy for the construction of water-soluble supramolecular polymers [221,222]. However, the molecular and polymeric precursors are typically structurally flexible. Thus, rigid and preorganized precursors have been prepared to achieve supramolecular frameworks that display intrinsic regular porosity, whereas multiple pyridinium and quinolinium cationic units have been introduced to tri-, tetra-, and hexa-topic precursors to provide the resulting SOFs with good water-solubility and high stability as a result of binding multivalency.

2.5.2 2D SOFs

The first example of supramolecular organic frameworks was reported in 2013. Zhao, Liu, Li, and coworkers [219] designed and prepared rigid triangular compound **1a**, which was used to co-assemble with CB[8] to afford 2D **ml-SOF-1a**. The introduction of three pyridinium units and three hydrophilic glycol chains in **1a** endowed **ml-SOF-1a** with high water solubility. The glycol chains also force the three appended benzene rings to twist perpendicularly to the central benzene ring, which efficiently suppresses the face-to-face stacking of the whole aromatic backbone and thus facilitates the co-assembly of **1a** and CB[8] in the 2D space. The enhancement of CB[8] encapsulation for the dimerization of *N*-alkyl-4,4′-bipyridine in water was first reported by Liu *et al*. [223]. The phenyl group was attached to the bipyridine unit to produce a fully rigid backbone.

A combination of various techniques was used to characterize the structure of **ml-SOF-1**. ^{1}H NMR in D_2O and UV-vis absorption experiments confirmed the 2:3 binding stoichiometry of **1a** and CB[8]. Competition ^{1}H NMR experiments in CD_3CO_2Na-buffered D_2O also showed that the encapsulation complex formed by CB[8] and the intermolecular dimer of the *N*-phenyl-4,4′-bipyridine unit was much more stable than that formed by CB[8] and a control compound, revealing large cooperativity due to the multivalency of tritopic **1a**. Dynamic light scattering (DLS) experiments supported that their 2:3 solutions afforded supramolecular entities with D_H being more than 100 nm at large concentrations. The regularity or periodicity of **ml-SOF-1** was confirmed by a solution-phase small-angle X-ray scattering (SAXS) experiment in water, which revealed a scattering peak with a *d*-spacing of 3.61 nm. Considering the dynamic character of non-covalent self-assembly in solution, this spacing reasonably matched the pore diameter of 3.70 nm which was calculated for the monolayer honeycomb SOF formed by **1a** and CB[8] (Figure 14). The powder X-ray diffraction (PXRD) profile of the dried sample of **ml-SOF-1** exhibited a broad (100) peak with a *d*-spacing of 3.70 nm, whereas the synchrotron X-ray scattering profile of the solid sample showed a scattering peak with a *d*-spacing of 3.78 nm, both of which matched with the expected diameter of the repeating units in the honeycomb framework, further supporting the periodicity of the framework was maintained in the solid state. The monolayer feature of **ml-SOF-1** was confirmed by atom force microscopy (AFM) imaging, which revealed planar aggregates of large sizes with an average height of 1.72 nm. This height perfectly matched the diameter of CB[8] (1.75 nm) which defined the thickness of the monolayer SOF. The above methods have also been applied for the establishment of the structures of other periodic SOFs.

The CB[8] encapsulation-enhanced homodimerization of hydrophobic aromatic units has been extended to many other triangular precursors [224], including compounds **2**–**4** (Figure 14), which led to the construction of different 2D SOFs of honeycomb topology. Monolayer **ml-SOF-2** formed from **2** and CB[8] displayed porosity periodicity [225], which indicated that the formation of the framework forced the triphenylamine backbone to adopt a planar conformation. Compared with pure **2**, this compound in **ml-SOF-2** exhibited a 35-fold enhancement of fluorescence enhancement, which could be quenched selectively by picric acid and thus used to detect this explosive. Cyanostilbene derivative **3** in 2D **ml-SOF-3** formed by its mixture with CB[8] was highly fluorescent with a high quantum yield of 0.6 and a long exciton lifetime [226]. Thus, this SOF could be used as an all-organic photosensitizer for photocatalytic H_2 production from pure water. The formation of 2D **ml-SOF-4** by compound **4** and CB[8] also caused an important aggregation-induced enhancement (AIE) effect for the fluorescence of **4** [227], which was used as a fluorescent probe for intracellular DNA imaging.

Tetraphenylethene (TPE)-derived tetratopic compounds **5**–**7** were also prepared to generate parallelogram 2D monolayer SOFs through the encapsulation of CB[8] for the intermolecular dimers formed by their peripheral aromatic units. TPE is the prototypic aromatic backbone of the AIE effect [228,229]. Again [230], the TPE unit of **5** in the 2D framework **ml-SOF-5** formed by it and CB[8] exhibited this effect in the water. Interestingly, adding tetrahydrofuran to the solution promoted this effect due to the enhanced aggregation of the SOF monolayers. Monolayer 2D **ml-SOF-6** made from **6** and CB[8] could stack to form supramolecular cuboids [231]. Compared to monomer **6**, the SOF aggregates exhibited large red shifting of up to 82 nm of the maximum emission peak. Moreover, this fluorescence emission displayed stimuli-responsive turn-off/turn-on, which could be further applied in cellular imaging. The encapsulation of CB[8] for the dimers of the coumarin units of **7** led to the formation of a 2D monolayer **ml-SOF-7** [232]. Under the induction of L-/D-phenylalanine, this achiral 2D SOF showed adaptive chirality to afford anticlockwise- and clockwise-typed *M*- and *P*-structures in water, which was attributed to the dynamic rotational conformation of the TPE

unit of monomer **7**.

Apart from the above binding motif of CB[8] encapsulation for aromatic homodimers, several other binding patterns have been reported to construct 2D monolayer SOFs. For example, the naphthalene units of compound **8** and the bipyridinium units of porphyrin derivative **9a** could form donor-acceptor complexation to drive the two molecules to form 2D supramolecular networks [233]. This complexation could be greatly strengthened through the encapsulation of CB[8], which also remarkably improved the regularity of the networks. That is, the three components co-assembled to produce the first square-styled 2D monolayer framework **ml-SOF-8/9a**. Strong donor-acceptor interaction was also formed between the electron-rich naphthalene units of **8** and the electron-deficient bipyridinium units of **1b**, which led to another honeycomb 2D monolayer framework **ml-SOF-1b/8** [234]. This supramolecular network was further strengthened by the encapsulation of CB[8]. When the OH groups of **8** were replaced with two NH_2 groups, the corresponding 2D SOF could display pH-responsive formation and decomposition. The three bipyridinium units of rigid triangular compound **1b** could be readily reduced to the corresponding radical cations, which underwent strong stacking to afford the 2D monolayer framework **ml-SOF-1b** [235]. This unique conjugated radical cation dimerization could be further stabilized by CB[8]. As a result, the resulting monolayer exhibited increased regularity.

The 1:2 mixture of **9b** and CB[8] in water afforded another squared 2D framework **ml-SOF-9b** [236]. The *N*-methylation of the inner pyridine units forced the CB[8] ring to hold the intermolecular dimers of the exterior 4-phenylpyridinium units. Upon an addition of 0.5 equivalent to compound **10**, its two pyridine units strongly coordinated with the zinc porphyrin units of **9b** in the monolayers. As a result, a water-soluble bilayer 2D supramolecular architecture **bl-SOF-9b/10** was constructed.

2.5.3 3D SOFs

3D polymeric networks have the advantage of forming intrinsic porosity. The strategy of CB[8] encapsulation for aromatic dimers also works well for the construction of 3D SOFs. The first example of 3D diamondoid SOFs, **d-SOF-11** (Figure 15), was reported in 2014 from the co-assembly of tetrahedral compound **11** and CB[8] (1:2) [237]. Commercially available tetra(4-bromomethylphenyl)methane was used to prepare **11** by coupling with 4-(4-methoxyphenyl) pyridine. As a result, various 4-substituted pyridines were used to prepare other similar tetrahedral precursors, including compounds **12**–**16** (Figure 14) [215,238–242]. Their co-assembly with CB[8] (1:2) afforded the corresponding 3D SOFs that possessed the same diamondoid topology. The four methylene units in these compounds endowed the backbone with certain flexibility. However, solution-phase synchrotron radiation scattering and diffraction experiments supported that these 3D SOFs possess porosity periodicity. Fully rigid and preorganized compounds **17** and **18** could also bind CB[8] to afford the corresponding 3D SOFs [243,244].

Depending on the length of the peripheral arms of the tetrahedral precursors, these 3D SOFs have an aperture size of 2.1 nm to 3.5 nm. At [**10**]=1.5 mM, **d-SOF-11** had a hydrodynamic diameter of 91 nm [237], which further increased to 100 nm at higher concentrations. High-resolution transmission electron microscopic (TEM) imaging was able to resolve the periodic porosity with the 1.7 nm spacing, which corresponded to the (220) face, indicating that the framework maintained its periodicity in the solid state. 3D SOFs obtained from compounds **12a**–**12e** and **16** could adsorb various anionic and hydrophobic organic guests for efficient intracellular delivery [238,239]. The SOFs formed from **13**, **15,** and **17** also efficiently enriched both $[Ru(bpy)_3]^{2+}$-derived photosensitizers and various polyoxometallate (POM) photocatalysts of very low concentrations [215,240,243]. Through this strong enrichment effect, the SOFs could remarkably improve their photocatalytic efficiency for the reduction of protons to generate hydrogen gas. Compound **18** was fluorescence-silent. However, 3D framework **d-SOF-18** prepared from it and CB[8] exhibited strong fluorescence in water [244]. The fluorescence was quenched by various nitrobenzenes. Among others, picric acid displayed the largest quenching ability, which had been used to detect the acid, reaching the limit of detection of 0.024 μM. The co-assembly of **15** and CB (1:2) afforded 3D **d-SOF-15** [215]. The encapsulation of CB[8] for the per-

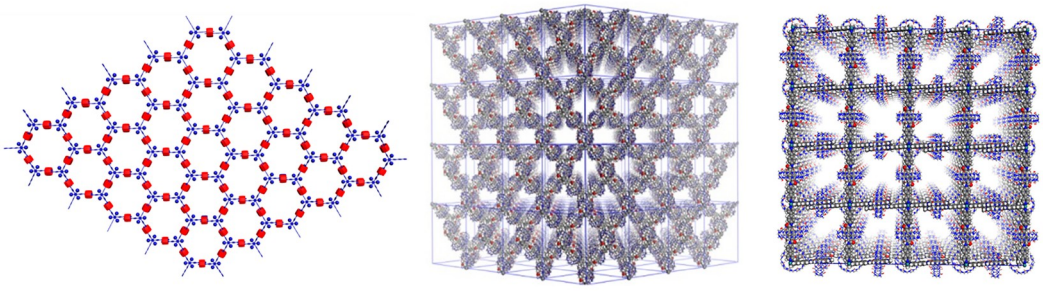

Figure 15 The structure of 2D monolayer **ml-SOF-1a** (left), 3D diamondoid **d-SOF-1** (middle), and 3D cubic **c-SOF-1** (right) (color online).

ipheral aromatic segments of **15** promoted close stacking of the styrene units. As a result, the styrene units underwent quantitative [2+2] photodimerization, which led to the generation of new water-soluble 3D COF with detectable periodicity.

The crystal structure of 3D framework **d-SOF-14** formed by compound **14** and CB[8] revealed CB[8] encapsulation of two anti-parallel *n*-butyl chains [241], instead of two pyridinium units, and 3-fold interpenetrated networks. Due to this interpenetration, this 3D SOF did not produce space for the inclusion of an organic molecule. However, the SOF did not undergo interpenetration, which was supported by efficient adsorption of nano-scaled porphyrin guests. The filling of water molecules was proposed to rationalize the absence of interpenetration in the solution. In contrast, due to the lack of water molecules, the frameworks in crystals interpenetrated to avoid the formation of large voids.

2.5.4 Coordinate and dynamic covalent 3D SOFs

$[Ru(bpy)_3]^{2+}$ complex is an ideal building block for the development of hexatopic monomers. To extend the scope of monomers for the generation of SOFs, Li and coworkers [245] prepared octacationic complex **19**, which was highly soluble in water. The 1:3 mixture of **19** and CB[8] afforded the first cubic SOFs of **c-SOF-19** in water (Figure 14). The periodicity of the cubic framework was confirmed by the solution-phase X-ray scattering and diffraction experiments. **c-SOF-19** had a pore size of 1.5 nm and could enrich polyoxometalate catalysts. The $[Ru(bpy)_3]^{2+}$ complex core functioned well as a photosensitizer. Upon the irradiation of visible light, the $[Ru(bpy)_3]^{2+}$ complex was excited to give electrons to the POMs. As a result, its photocatalytic activity for the reduction of proton to produce hydrogen gas was remarkably increased. **c-SOF-19** may be regarded as a special water-soluble metal-organic framework that can be generated through a supramolecular strategy.

Compound **20** was prepared through the formation of six hydrazone bonds from the corresponding aldehyde and acylhydrazine precursor [246]. In water, the yield was only 4.2%. With the addition of CB[8], another cubic framework **c-SOF-20** was prepared, which also promoted the formation of **20** quantitatively. That is, the formation of **c-SOF-20** greatly stabilized the hydrazone bond in water. This water-soluble porous framework may be regarded as a hybrid of SOF, MOF, and COF.

Complex **21** bears six peripheral aromatic units that are connected to the $[Ru(bpy)_3]^{2+}$ complex core through the CH_2 linker [247]. This compound is also bound with CB[8] to afford porous supramolecular polymers, which, however, did not exhibit detectable regularity. Nevertheless, cubic framework **c-SOF-22**, constructed from **22** and CB[8], displayed porosity periodicity [248], even though **22** bears flexible linkers to connect the peripheral naphthalene units. In this case, the encapsulation of CB[8] for intermolecular dimers of the naphthalene units was the driving force for the formation of the regular framework. These differences imply that the length and structure of the hydrophobic aromatic units played a key role in the regularity of the 3D frameworks. As a rigid tetrahedral complex, **23** also co-assembled with
CB[8] to afford diamondoid framework **d-SOF-22** [249], which represents a water-soluble interwoven supramolecular architecture. This 3D SOF was found to catalyze visible light-induced organic transformations.

2.5.5 SOFs for drug/biomacromolecule delivery

As a special family of water-soluble porous organic polymers, 3D SOFs feature efficient adsorption of drugs and biomacromolecules in aqueous media. Moreover, this adsorption takes place in an *in-situ* manner and the drugs or biomacromolecules can be maintained in the interior of the frameworks for hours to days. All the 3D SOFs have hydrodynamic diameters ranging from 30 to ≥200 nm, which depend on the concentrations. Although the frameworks are generated at high concentrations, their dilution-caused deassembly is quite slow due to the unique encapsulation mechanism of CB[8] for various aromatic dimers, of which the decomposition needs to overcome a high energy barrier. It has been established that the nan-scaled size of 3D SOFs enables this kind of 3D supramolecular architecture with good ability as transmembrane carriers for drug and biomacromolecules. Thus, 3D diamondoid supramolecular organic frameworks d-SOF-11, d-SOF-12a–e, and d-SOF-16 prepared from the compounds **11**, **12a**–**12e**, or **16** and CB[8] have been found to realize intracellular delivery of anti-tumor therapeutic agent pemetrexed and doxorubicin and short DNA [238,239]. *In vivo* experiments showed that the delivery of SOF-11 and d-SOF-12a–e for pemetrexed and doxorubicin could considerably improve their efficacy.

2.6 Hypercrosslinked porous polymer

HCPs are a class of permanent microporous polymer materials first described by Davankov, and they are generating a lot of attention in the scientific community. HCPs have seen a fast expansion in recent years as a result of their several features, including diversified synthesis processes, simpler functionalization, high surface area, low-cost reagents, and gentle working conditions. A well-developed polymer framework with an adjusted porosity topology was achieved thanks to appropriate monomer selection, adequate crosslinkers, and optimum reaction conditions. The integration of diverse chemical functionalities that may lead to intriguing features and boost selectivity toward a given application is facilitated by post-synthesis alteration of the already pro-

duced network.

2.6.1 *Post-crosslinking*

In the early 1970s, Tsyurupa and Davankov reported the first cases of HCPs (also known as Davankov resins), in which polystyrene-based precursors such as linear solvated polystyrene or gel-type swollen polystyrene-co-divinylbenzene (polySt-DVB) were crosslinked in the presence of an external crosslinking agent (external electrophiles). Figure 16 shows the entire description of the synthesis, in which the pre-synthesized polystyrene chains are equally dispersed in the solvent with a stoichiometric quantity of bifunctional crosslinking agent and catalyst before crosslinking. As a result, the reaction occurs swiftly, forming strong bonds between nearby benzene rings as well as rigid bridges in numerous chain segments. Moreover, solvated polystyrene was transformed into a single-phase material with a low bulk density and a large porosity structure [250]. By using a range of crosslinking agents with varied connecting units (such as modifying length and rigidity), the internal skeleton structure of the final product may be readily altered manifested by changes in surface area and porosity.

The hypercrosslinking reaction between polystyrene-based precursors and external crosslinking agents is usually a one-pot process, in which the chloromethyl of the benzene ring is converted to methylene bonds. Using commercially available chloromethylated polySt-DVB resins, a two-step followed by crosslinking *via* internal condensation of the chloromethyl group was proposed by Veverka [16]. To further understand the effect of chloromethyl content on the reaction, Sherrington and colleagues [251] prepared a series of vinylbenzyl chloride-divinylbenzene copolymers (polyVBC-DVB) with definite functional components (2% and 20% DVB content, respectively). Then the hypercrosslinking process was carried out under different conditions, such as monomer ratios, solvents, Lewis acid catalysts, and reaction times. Under the optimized conditions, the gel-type precursor containing only 2% DVB can produce the material with highest surface area of up to 2,090 $m^2 g^{-1}$. After that, Tan and colleagues [252] increased the DVB content from 0 to 10%, demonstrating the special control over the pore structure of the resulting hypercrosslinked polymers (HCP-DVB-VBC). When the DVB content was 2%, the highest surface area obtained was 2,060 $m^2 g^{-1}$, which is consistent with the previous results. Although the microporosity can be successfully controlled by changing the DVB content, it is usually difficult to regulate the mesopores. Besides, Fréchet and Svec *et al.* [253,254] prepared the monolithic poly(styrene-co-vinylbenzyl chloride-co-divinylbenzene) (poly ST-VBC-DBC) stationary phase for the high-efficiency separations of some small molecules. Seo and coworkers [255] reported the synthesis of hierarchical porous polymers with permanent micropores and three-dimensional continuous mesopores by self-assembly and post-hypercrosslinking of block copolymer.

In addition to these polystyrene-based resins, other heterochain polymers, such as polysulfone [256], polyarylates [256], polyaniline [250], and polypyrrolev [72], were also hypercrosslinked to produce highly porous networks. The hypercrosslinking of polysulfone was carried out *via* a two-step reaction in the presence of a Friedel-Crafts catalyst. Warshavsky and coworkers [32] proposed a safe method of polysulfone halomethylation that allowed the introduction of bromomethyl into each benzene ring. Fréchet and Svec developed hypercrosslinked polyaniline [250] and polypyrrole [72], and the apparent surface areas of the resulting networks were 630 and 720 $m^2 g^{-1}$, respectively. Recently, Sharma and coworkers [33] also reported the use of a simple microwave-assisted process to synthesize nanoporous hypercrosslinked polyaniline with a specific surface area of up to 1,059 $m^2 g^{-1}$.

Some other types of porous networks, even though they are not synthesized by the typical Friedel-Crafts reaction, can also be classified as hypercrosslinked species. Webster and coworkers [257,258] prepared high porous organic networks with 4,4′-dilithio-biphenyl and dimethyl carbonate at a low temperature of −80 °C and obtained a relatively high surface area of 1,167 $m^2 g^{-1}$. A hybrid arylene-bridged polysilsesquioxane network was synthesized by Loy and Shea *et*

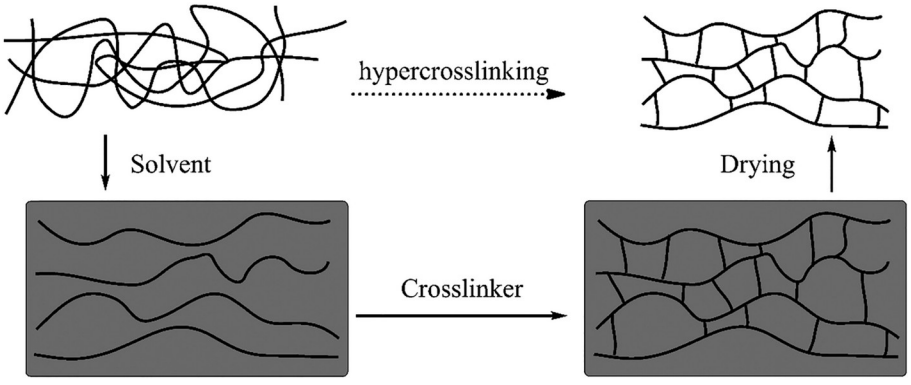

Figure 16 Schematic representation of the hypercrosslinking process.

al. [259,260], and the surface areas of 600–1,800 $m^2 g^{-1}$ could be obtained by simply changing the bridge length. Recently, Li and colleagues [261] have proposed a radical copolymerization of rigid bi-vinyl-containing monomers, bismaleimides, and divinylbenzene to synthesize novel hypercrosslinked organic microporous polymers.

2.6.2 *Direct polycondensation or one-step condensation*

The most notable benefit of post-crosslinking is that commercially accessible polymer compounds may be used as crosslinking precursors. However, polymer precursor synthesis takes time, and free radical polymerization and Friedel-Crafts alkylation processes can only choose a small number of functional monomers to match the combination conditions [256]. Cooper and coworkers [73,262] explored for the first time using small polyfunctionalized organic compounds as reaction monomers and crosslinkers to directly polymerize HCPs. In the presence of Lewis acid catalysts, chloromethyl groups can easily react with adjacent benzene rings and form highly rigid methylene bonds by eliminating hydrogen chloride molecules between small molecular components. The results show that the specific surface areas and gas adsorption performance of HCPs materials can be controlled by changing the monomer ratio. When the monomer ratio of DCX to BCMBP was 1:3, the specific surface area of HCPs up to 1,904 $m^2 g^{-1}$ could be obtained, which was comparable to that of Davankov resin. Recently, Mondal and coworkers [263] selected benzyl bibromide and triphenylamine to obtain nitrogen-rich HCPs materials through Friedel-crafts alkylation reaction, and the specific surface area of the material can reach 1,165 $m^2 g^{-1}$. The abundant N elements can be used as the metal binding sites to improve the stability of metal nanoparticles, which can be used to effectively catalyze the reduction of vegetable oil to alkane chains.

2.6.3 *External crosslinking*

Tan and colleagues [264] proposed the knitting strategy, in which a relatively active agent, formaldehyde dimethyl acetal (FDA), was used as an external crosslinker to bind simple aromatic compounds like benzene or biphenyl with rigid methylene bridges *via* a Friedel-crafts reaction catalyzed by anhydrous $FeCl_3$. Several kinds of aromatic building blocks such as benzene, biphenyl, TPB, toluene, chlorobenzene, and phenol, were knitted directly, and the resulting materials have predominant micropores and high surface areas [264–273]. In addition, by changing the molar ratio of crosslinkers to monomers, the porous structures and surface areas can be adjusted, and finally, the degree of crosslinking can be affected. When the ratio of crosslinker to benzene is 3:1, the apparent surface area of the knitted networks was the highest, up to 1,391 $m^2 g^{-1}$. Since the development of the knitting strategy, it has been widely used in the synthesis of various types of rigid building units with different structures and special functionalities of hypercrosslinked microporous materials. Tan *et al*. [274] prepared layered hypercrosslinked microporous polymer (SHCP) at low temperatures utilizing dichloroalkane as both a solvent and an external crosslinker in 2017, based on prior work on the knitting method, as illustrated in Figure 17. The pore structures and specific surface areas of these polymers can be controlled by adjusting the chain length of the solvent, the molar ratio of $AlCl_3$, and the size of the monomer. Moreover, 2D SHCP nanosheets were obtained by a new ultrasonic-assisted solvent stripping method. It is worth mentioning that the solvent knitting approach may produce an ultra-high specific surface area of up to 3,002 $m^2 g^{-1}$. This effective and low-cost approach may produce HCPs with layered structures and large specific surface areas, as well as superior gas adsorption capability (273 K, 4.82 mmol g^{-1} at 1.00 bar; the adsorption capacity of hydrogen at 77.3 K and 1.13 bar was 12.40 mmol g^{-1}). This discovery provides the possibility for the design and synthesis of previously unknown layered HCP materials.

2.6.4 *Free radical polymerization of vinyl monomers*

In addition to the method of preparing HCPs based on the Friedel-crafts alkylation reaction mechanism, the polyfunctional aromatic vinyl monomers can also be employed to synthesize HCPs through free radical polymerization. As early as 1964, Moore and coworkers [275] reported the preparation of highly crosslinked microspheres by free radical polymerization of styrene and divinylbenzene, which were widely used in commercial volumetric exclusion

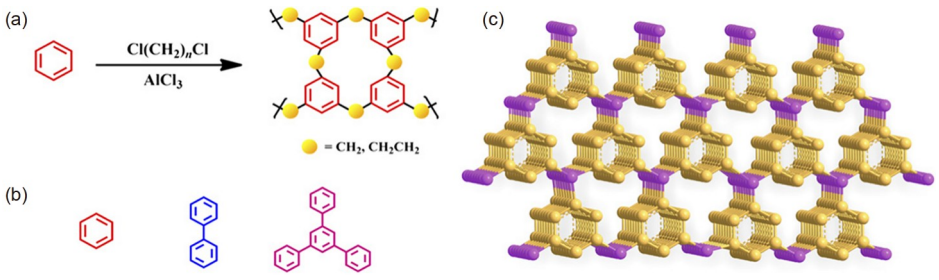

Figure 17 (a) The synthetic pathway to produce the network structure. (b) Molecular structures of the building blocks for the network. (c) The layered model of benzene-based polymer [274] (color online).

chromatographic columns. Recently, Li and coworkers [276] reported a method of free radical polymerization of vinyl monomers initiated by ultraviolet light, and the results showed that HCPs materials could be prepared by free radical polymerization without any catalyst. Among them, DVB/PET4A exhibited the highest specific surface area up to 887 $m^2 g^{-1}$. Subsequently, the ester groups in the HCP structure were hydrolyzed to carboxyl groups, which endowed the material with good hydrophilicity and demonstrated the ultra-high adsorption performance of methylene blue (485 mg g^{-1}).

Xiao and coworkers [277] used homogeneous catalyst ligands functionalized by polyvinyl as construction units to obtain HCPs porous ligands with high specific surface area through free radical polymerization. In the process of polymerization, azo diisobutyronitrile (AIBN) was selected as the initiator to initiate the free radical polymerization of vinyl groups on the monomer under hydrothermal conditions. Three kinds of HCPs were obtained, among which POL-PPh_3 had a specific surface area of up to 1,086 $m^2 g^{-1}$. Moreover, HCPs supported with Rh can be used to catalyze the hydroformylation of 1-octene with high catalytic activity and cycle stability. Subsequently, Xiao and coworkers [278] modified an organic catalyst, 2,2,6,6-tetramethylpiperidin-1-oxygen radical (TEMPO) onto vinyl functionalized monomer, and obtained TEMPO-containing porous materials (PPO-TEMPO) through free radical polymerization. The HCPs showed high surface areas, multi-stage pore structures, and good stability, which could be directly utilized for selective catalysis of alcohols to obtain corresponding aldehydes or ketones.

3 Synthesis of POP films

As mentioned above, POP materials have exhibited good physical and chemical properties and application potential. However, some practical applications are severely limited because of the poor solubility of POP materials. Therefore, direct synthesis of POP thin films has been carried out to overcome these limitations. To date, synthetic methods of the POP films have been successfully established [279], which provides great opportunity for POP application.

3.1 Interfacial synthesis of POP films

Interfacial synthesis is a powerful strategy for the fabrication of POP films. The interface provides a confined region for the covalent reactions of monomers in the POP film.

3.1.1 Synthesis on the solid surface

Synthesis of single layer POP. 2D COF materials are a kind of special POP materials with a layered structure similar to 2D inorganic materials. Inspired by the great development of graphene and other 2D materials, single layer 2D COF (sCOF) with similar structures has drawn great attention in the past few years [280]. So far, most high-quality sCOF is mainly obtained by the on-surface synthesis method. The presence of a well-defined single crystal surface contributes to the monolayer growth of sCOF in two dimensions and could support the resulting film. The achieved sCOF films on conductor surfaces could be observed by scanning tunneling microscopy (STM) with high resolution and other surface characterization techniques.

One important on-surface synthesis strategy of the sCOF is developing on a metal surface under an ultrahigh vacuum environment [281,284–288]. In this case, metal substrates can not only act as substrates to support the growth of thin films but also as catalysts to catalyze the coupling reaction. Since the first attempt based on on-surface synthesis to grow sCOF in an ultrahigh vacuum in 2007 [284], various reactions such as Ullmann radical coupling, boronic anhydridation, polyimide formation, and imine coupling have been successfully introduced into the construction of sCOF. For example, to promote the quality of sCOF, Grill and Hecht and coworkers [281] proposed a sequential activation strategy for the construction of 2D sCOF on the Au(111) surface, instead of a one-step connection (Figure 18a). With the catalysis of Au substrate, using a trans-configuration porphyrin building blocks owning two bromine and two iodine substituents, the two-step reactions were carried out at 120 and 250 °C, respectively. Based on the different thermal activation of iodine and bromine substituents, linear chain structures were firstly obtained through the reactions at the iodine sites, and then transformed to sCOF structures by the activation of the bromine sites.

In addition to the preparation in UHV, many efforts have been paid to the investigation of the on-surface synthesis of sCOF in ambient conditions [282,283,289,290]. By regulating the reaction conditions to provide a moderate reversible environment, several sCOF samples with large coverage and high quality were successfully obtained on the solid highly oriented pyrolytic graphite (HOPG) surface.

For instance, the thermodynamic equilibrium method was applied in the synthesis of boroxine sCOF by Wang and coworkers (Figure 18b) [282]. Boronic acid monomers were dispersed on the HOPG surface, and the substrates were subsequently placed in a closed autoclave. $CuSO_4 \cdot 5H_2O$ was added as a "solidified" water resource to the closed system and could release water at the reaction temperature to regulate the chemical thermodynamic equilibrium of the dehydration reaction. In the presence of $CuSO_4 \cdot 5H_2O$, the long-range ordered sCOF coverage was confirmed to cover 98% by STM, which benefitted from the improved reverse reaction environment to enhance the self-healing process of sCOF. A similar phenomenon through adding water was also

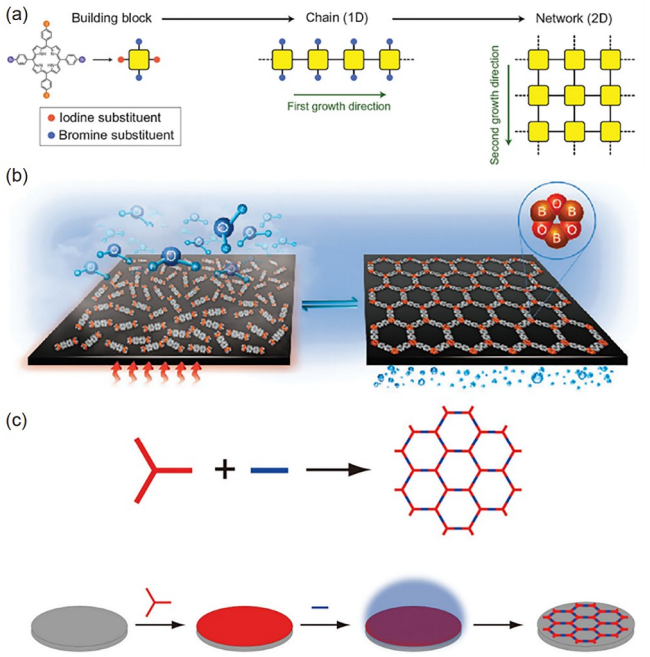

Figure 18 (a) Schematic illustration of the sequential activation strategy for the construction of 2D sCOF with trans-Br_2I_2TPP [281]. (b) The illustration of the sCOF-1 synthesis route in a water atmosphere based on the thermodynamic equilibrium method [282]. (c) Schematic illustration of the solid-gas interface strategy interface reaction for sCOF synthesis based on kinetic control [283] (color online).

observed by Lackinger and coworkers [290].

Furthermore, a solid-gas interface strategy based on kinetic control was established to obtain high-quality sCOFs using two monomers (Figure 18c) [283]. At the reaction temperature, small molecules were vaporized, and the confined polymerization of two monomers was tailored to occur at the solid-vapor interface. The gas-phase dosing of small molecules effectively promotes the attachment of small molecules to the available sCOF nuclei and thus results in the growth of high-quality sCOF.

Intriguingly, the external field has been confirmed that it can also regulate the growth of SCOF. Recently, the reversible transformation between molecular self-assembly and monolayer COF film has been realized on a solid surface (HOPG) by using the vertical electric field. At the HOPG-liquid surfaces, when changing the STM tip voltage from negative to positive, the molecular self-assembly structure transformed into boroxine-linked monolayer COF films. sCOF film grown directly on functional substrates provides an important basis for further study of the properties of COF monolayers.

Solid-liquid interface synthesis. The synthesis of the POP film based on the solid-liquid interface is a widely used strategy for the preparation of large-area POP films on substrates. Typically, the substrates (sometimes with surface modification) were directly placed into the POP precursor solution, and the POP films were deposited on the surface of the substrates during the reaction process [291]. To date, various POP films have been grown on different functional substrates [291–295].

For instance, the oriented COF films were prepared on single layer graphene (SLG) at the solid-liquid interface. Dichtel and coworkers [291] added SLG/Cu, SLG/SiC, and SLG/SiO_2 substrates to the COF-5 precursor mixture solution and collected the oriented COF-5 films samples around sub-200 nm thick after the solvothermal process (Figure 19a). The crystallinity and orientation of the obtained films were further confirmed by grazing incidence diffraction (GID) experiments. Since that, plenty of efforts have been paid to the solid-liquid interfaces on robust substrates like SiO_2 wafers, glass, and ITO for different applications. Liu and coworkers [296] reported an oriented TTF-COF film directly growing on the ITO and SiO_2 wafer. The high

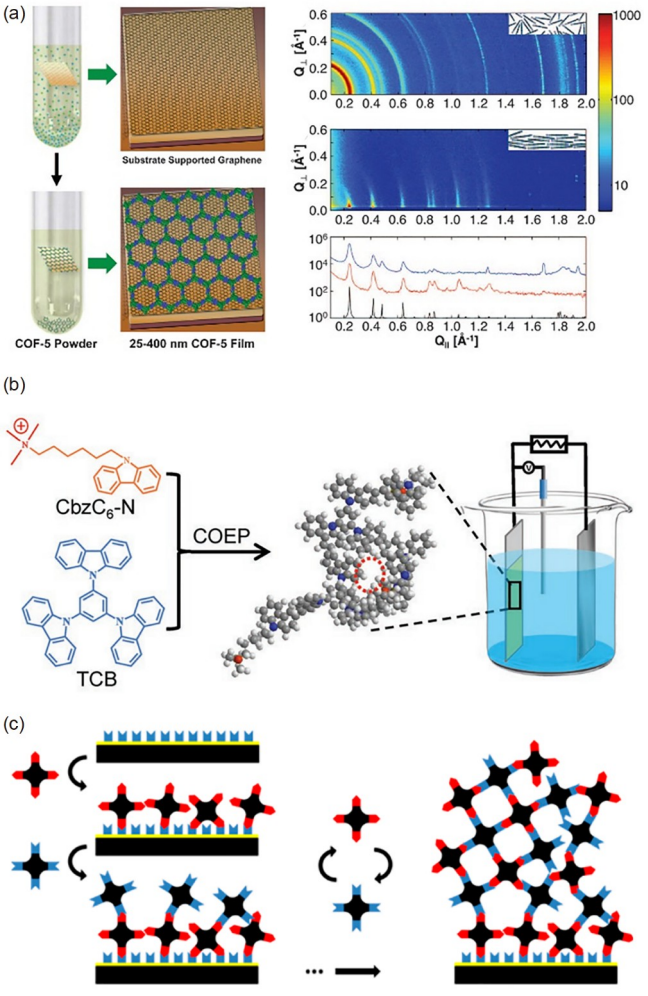

Figure 19 (a) Scheme for the synthesis of oriented COF-5 films on graphene surface by solid-liquid interface method [291]. (b) The illustration of the co-electro-polymerization of flexible ionic CMP film on the ITO electrode [294]. (c) The illustration of the layer-by-layer method for the synthesis of defect-free CMP nano-films on flat substrates [295] (color online).

crystallinity and orientation (the pores normal to the substrates) were confirmed with GIWAXS.

The poor solubility and processability of CMPs are also a problem for the synthesis of CMP films. Tang and coworkers [297] presented a solid-liquid surface-initiated polymerization strategy for the preparation of high-quality CMP films. The bromobenzene-modified Si/SiO_2 wafers were introduced as the functional substrates to the precursor solutions. The CMP films were first fabricated on the surface of the wafer by solvothermal polymerization of the building blocks and then transferred onto other porous supports for the organic-solvent nanofiltration. Similarly, the continuous PAF films were also synthesized on modified Si/SiO_2 wafers [298]. The coupling reaction occurred between the Si/SiO_2 wafer functionalized with phenyl-bromide and the building units of iPAF-5 bringing a slow generation process of PAF films.

Electropolymerization is a powerful tool for preparing POP films on the solid-liquid interface [294,299–302]. Ma and coworkers [299] reported the fabrication of POP network films electrochemically for the first time. After that, a polyborane carbazole POP film was also prepared by the concurrent polymer-film deposition-electropolymerization method [302]. The polyborane carbazole film exhibited outstanding performance in solar cells and light-emitting diodes. Lai and coworkers [294] fabricated a flexible ionic CMP film on the ITO surface through the co-electro-polymerization strategy (Figure 19b). By incorporating flexible alkyl chains and the ionic groups at the same time, the authors successfully turned the rigid CMP film into a flexible ionic CMP (i-CMP) film with excellent ion transport rate and ion sieving behavior.

LbL (layer-by-layer) method. The LbL method is also a normal film growth method at the solid-liquid. The POP films can be grown on the substrate with controllable thickness by alternately exposing the substrate surface to different building block solutions. The LbL method can be used to construct not only nanoscale thin films but also micron-scale POP films [295,303,304]. For example, Tsotsalas and coworkers [295] chose two monomers terminated with azide functional groups and alkyne functional groups respectively (Figure 19c). Then the virtual defect-free CMP-nano-films could be grown on flat substrates through the LbL method based on click reaction. While exposing porous substrate hydrolyzed polyacrylonitrile ultrafiltration membranes to the two monomers solutions alternately, the imine-linked COF films with the micron-scale thickness could be synthesized and applied in the molecular separations [304].

3.1.2 Synthesis on the liquid surface

Liquid-air interface. Liquid-air interface reactions have also been applied to the synthesis of COF thin film. As early as 2002, Michl and coworkers [305] designed a sandwich porphyrin monomer adsorbed firmly on a liquid mercury surface. For the air-water interface, Bao and coworkers [306] reported a large-area imine-linked COF film growth at the air/liquid interface. By preparing a DMF solution containing monomers TAPA, BDTA, and catalyst acetic acid as the mother solution in a covered petri dish, the polyTB POP films emerged at the air/solution interface after 2 days of reaction with a saturated H_2O atmosphere. The achieved POP film's area was as large as a petri dish, and the adjustable thickness from ~2 to 29 nm was controlled by incubation time.

Recently, Langmuir-Blodgett (LB) method was introduced to the preparation of 2D covalent organic monolayer [307]. Monomers of $CHCl_3$ solutions were spreading on the water surface, and a self-assembled monolayer was further obtained by the LB method [307]. After the addition of the acid catalyst to the water phase, a smooth, coherent, large, and freestanding polyimine monolayer was obtained by interfacial polymerization. Similarly, Feng and coworkers [308] also used the LB method to synthesize a similar 2D covalent organic monolayer by dispersing two monomer molecules on the air-water interface and water solution phase, respectively. Recently, like the LB method, Choi and coworkers [309] also prepared a POP film by dispersing monomers at the air-water interface and used a photon-assisted imine condensation reaction to get the freestanding film.

To prepare POP films with good crystallinity and uniformity at the liquid-air interface, the surfactant was introduced to the liquid-air interface (Figure 20a). Feng and coworkers [310] presented the controlled synthesis of few-layer POP films on water surfaces assisted by surfactant monolayers. The surfactants were firstly added to the water, and the monomers were added subsequently. The presence of a surfactant monolayer helps the pre-organization of monomers at the water–surfactant interface. After polymerization, micrometer-sized, few-layer two-dimensional POP films could be obtained on the liquid-air interface.

Liquid-liquid interface. The liquid-liquid interface is widely used in the preparation of POP films. One typical method for the liquid-liquid method was dispersing monomers in two immiscible solvents to synthesize films at the interface of two solvents. Banerjee and coworkers [311] prepared a series of self-standing COF films by dispersing two types of monomers (amine-PTSA and aldehyde) in H_2O and dichloromethane respectively (Figure 20b). The covalent reaction occurs at the interface to form the COF films. These COF films exhibited a large area and sub-100 nm thickness, and could self-stand on a U-shaped glass loop and easily be transferred to any substrates. Similarly, POP films [312] and SOF films [313] could also be prepared at the liquid-liquid interface. After the polymerization process, these films can be deposited on other substrates by removing the solution.

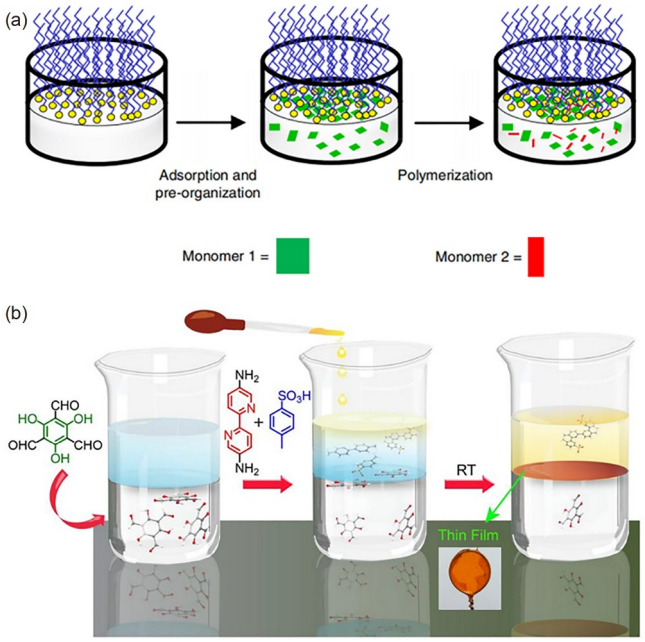

Figure 20 (a) Schematic illustration of the surfactant-assisted pre-organization synthesis of POP thin films at the water-air interface [310]. (b) Schematic illustration of the synthesis of $COF_{Tp\text{-}Bpy}$ films at the liquid-liquid interface [311] (color online).

Another method is dispersing monomers and catalysts in two immiscible solvents. For instance, both the amines and aldehydes monomers were dissolved in the mesitylene phase [314], while AcOH as catalysis for Schiff-base reaction was dissolved in the water phase. Then, the imine-linked CMP films could be synthesized at the water-mesitylene interface. Similarly, through dispersing monomers PDA and TAPB in the organic phase and catalyst $Sc(Otf)_3$ in the water phase respectively, Dicthel and coworkers [315] prepared a large area of COF film with a thickness tuned from 100 μm to 2.5 nm.

Besides, a synthesis strategy of COF films based on an oil/water/hydrogel tri-phase interface was presented by Wang and coworkers [316]. The hydrogel immersed in the oil phase could realize superspreading water layers, which could act as the confined reactor layer for the growth of COF films. Benefiting from the solid-like property and the slow-release capability of hydrogel, large-area self-standing COF films with high crystallinity, preferential orientation, and tunable thickness were successfully obtained at the tri-phase interface.

At the liquid-air and liquid-liquid interface, POP thin films with different thicknesses from monolayer to micron scale can be obtained. These POP films are always self-supporting thin films, and can also be facilely transferred to functional substrates for more applications.

3.2 Solution processing method

3.2.1 Solution processing

In general, the solubility of POP materials is always not very good. However, there are also some POPs that have good solubility in organic solvents and can be processed directly [317]. Typically, through spin coating or drop casting, the precursor solutions could be processed to POP films [318,319], and could be applied in the transport of ions and separation. Besides the linear POP, soluble CMP with a conjugated backbone has also been applied in film preparation through solution processing. Cooper and coworkers [320] designed and synthesized a soluble CMP by incorporating long alkyl groups to improve its solubility, and a uniform and transparent CMP film could be fabricated by drop casting of the obtained solution (Figure 21a). Baeg and coworkers [321] prepared a triazine-based 2D CTF film on a flexible polyimide substrate by the drop-casting method. The CTF powders were dissolved with DMF and dropped onto the substrate and left at 80 °C for 24 h to obtain CTF films. Moreover, Zhao and coworkers [322] developed several COF films by introducing auxiliary polymer poly(etherimide) (Ultem) and polybenzimidazole (PBI). The COF-NUS powders were mixed with Ultem and PDI with suitable solvents to generate suspensions. The 50–100 um NU-

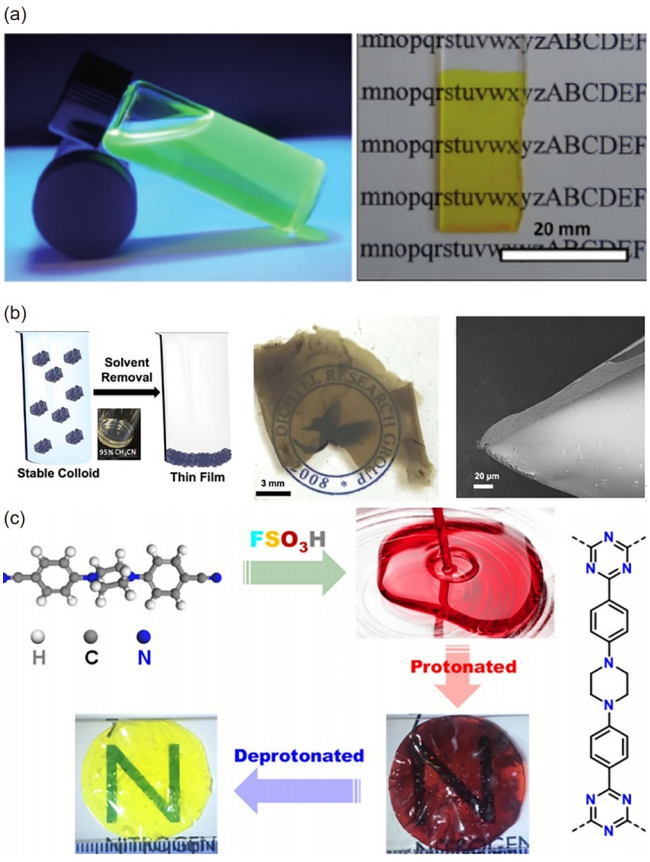

Figure 21 (a) The illustration of the synthesis of homogenous CMP films by drop casting method based on the soluble CMP [320]. (b) Scheme for the COF nanoparticles dispersion and solvent removal synthesis method for the synthesis of COF-5 films [324]. (c) Scheme for the sol-gel method for the synthesis of CTF films [213] (color online).

S@Ultem and NUS@PDI films were prepared by drop casting and a slow vaporization process.

3.2.2 Nanomaterials dispersion

Another method is to directly process the solution of POP materials (solutions or suspensions), and then make the as-prepared POP nanoparticles or powders into a solution and finally process them into thin films. Wang and coworkers [323] prepared stable suspensions of POP nanoparticles by Sonogashira polymerization. The homogeneous transparent POP films could be prepared by spin-coating subsequently. For COF, Dicthel and coworkers [324] demonstrated a novel COF film preparation from colloidal suspensions of COFs. When growing in ACN, COF-5 was found to form a stable colloidal suspension (Figure 21b). By evaporating the solvent at 90 °C, the suspension could finally turn to a free-standing COF-5 film. The high crystallinity and the preferential orientation were confirmed by GIWAXS, which may provide a new direction for the synthesis of COF films.

3.2.3 Sol-gel method

The sol-gel method is another strategy for POP film synthesis. Typically, the precursor solutions were formed as colloidal-like dispersion first, and then the POP films could be fabricated by solvent evaporation process in the second step [325]. The sol-gel method was successfully applied in the synthesis of POP, CTF, and COF films (Figure 21c) [213,325–327]. For instance, the precursor solutions were produced as a brown translucent emulsion and dropped on the substrate, and the transparent POPM films were formed through a mild thiourea-formation condensation reaction and flattened with a glass slice [327]. For CTF [213], the mixture of 4,4′-biphenyldicarbonitrile and FSO_3H was spread on a flat dish, and with the solvent evaporating, the transparent and flexible CTF films were generated on the substrate. Very similarly, COF films (TpPaSO_3H) could also be prepared by casting the mixed solution of the two monomers Tp and Pa-SO_3H on the substrate and heating them in the oven for 6 days.

3.3 Nanosheet synthesis

2D POP materials, stacked by weak interaction forces like hydrogen bonding, π-π stacking, and van der Waals forces between monolayers, can also be exfoliated into nanosheets with similar methods. In general, by first preparing bulk POP powders, then nanosheets can be effectively synthesized through chemical-related exfoliation and physical-related mechanical delamination.

3.3.1 Exfoliation

Similar to the exfoliation of 2D inorganic materials, with the help of suitable solvents, the weak interlayer interactions between the layers of COFs can be destroyed to obtain CONs [330]. For example, in dioxane, water, and DMF, the bulk 2D hydrazone-linked COF-43 powders could be exfoliated to CONs (Figure 22a) [328]. Similarly, CTF nanosheets (CTFN) could also be prepared by put bulk CTF in a solvent (like acetonitrile or THF) for sonication methods [331,332].

By adding other chemicals to disrupt the interlayer interaction, it is advantageous to realize the exfoliation for the synthesis of nanosheets. For example, by adding strong protonic acid methanesulfonic acid to break the interactions between the POP networks, the NDI-TFP polymer can be further exfoliated by ultrasound sonication to prepare nanosheets [333]. Also, Banerjee and coworkers [334] proposed two methods for the exfoliation of bulk COF by the covalent reaction. Through Diels-Alder cycloaddition reactions, the *N*-hexylmaleimide-functionalized CONs were exfoliated from anthracene-based COF DaTp. With the addition of *N*-hexylmaleimide to the backbone of COF DaTp, the π-π stacking between COF layers was weakened, and thus CONs were obtained.

3.3.2 Mechanical delamination

Mechanical delamination is another potential method to destroy the interlayer interaction between COF layers and prepare CONs. For instance, five imine-linked CONs were synthesized with a solvent-free mild manual grinding (Figure 22b) [329], which were confirmed by PXRD, AFM, and TEM characterization. The high chemical stability of COFs was believed to mainly contribute to the delamination process, while the π-π interlayer interaction could be easily

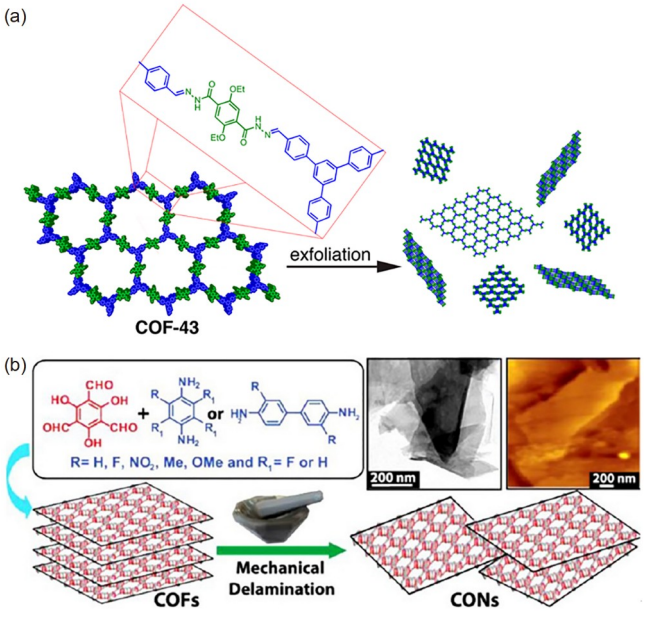

Figure 22 (a) Scheme for the solvent-assisted exfoliation of COF-43 to CONs [328]. (b) Scheme for the mechanical delamination of COFs to CONs [329] (color online).

destroyed by mechanical force without losing the ordered structure of COF.

3.4 Other strategies

Bein and coworkers [335] prepared BDT-COF and COF-5 films through room temperature vapor-assisted conversion method. Clean glass slices were coated with COF precursor solutions containing monomers and subsequently put into a desiccator with a vessel filled with a mixture of mesitylene and 1,4-dioxane. The presence of the vessel provided an atmosphere for the reaction solvent vapor in the desiccator, which was confirmed very important to the growth of COF films. With the help of vapor, 7.5 um BDT-COF and 300 nm COF-5 films with high crystallinity were successfully synthesized.

COF thin film could also be synthesized under continuous flow conditions [336]. Through pumping precursor solution through a 90 °C reservoir into a flow cell equipped with a quartz crystal microbalance (QCM) substrate, COF films could be obtained on the QCM, while the growth process could be monitored by the small mass changes on QCM. Benefiting from the nearly constant deposition rate, the introduction of continuous flow could prevent the concurrent generation of COF precipitates and improve control of film thickness.

4 Application of POP materials

4.1 Adsorption

Adsorption, including gas, dye, organic solvent, and chemical substance adsorption, is one of the largest research areas for POP applications so far. The synthetic tunability of porosity, structure, and functionality enables POPs and their composite materials as promising candidates for adsorption. In addition, owing to their good thermal and chemical stability, POPs are insoluble in common organic solvents and show great recyclability as adsorbents.

4.1.1 Gas adsorption

Based on their many characteristics, such as open pore structure, adjustable pore size, and modified skeleton, POP materials have shown good performance in vast applications. One of the most promising applications is the adsorption and storage of gases. There are some prerequisites that should be met to achieve efficient adsorption and storage of gas molecules. For example, for low-pressure gas adsorption, a suitable polar surface or adsorption group must be used to endow proper heat of adsorption. As to high-pressure gas storage, a large pore surface and open space are necessary for high volumetric capacity. Many POP materials that achieve the above-desired goals have been reported, and thus have great applications in the adsorption and storage of gas molecules (Table 2).

H_2 is a kind of clean energy gas with high energy density, and its storage is meaningful for industry and manufacturing. Owing to the high specific surface area values and tunable pore sizes, POPs meet the requirements for H_2 storage and become a competitive candidate as H_2 storage material. The permanent porosity enables POPs to show promising performance toward H_2 storage. Porous aromatic framework (PAF-1) with a S_{BET} up to 5,460 $m^2 g^{-1}$, possesses an H_2 storage capacity as high as 7.0 wt% at 77 K and 48 bar. Qiu and coworkers [91] introduced Si and Ge heteroatoms into the frameworks of PAF-1, and the resulting materials PAF-3 and PAF-4 with S_{BET} of 2,932 and 2,246 $m^2 g^{-1}$ show 2.07 wt% and 1.50 wt% of hydrogen adsorption capacity at 77 K and 1 atm, respectively. Because of the crystalline structures and the predetermined pore size, COFs have unique advantages in terms of the size effect of hydrogen storage. By simulation, the designed COFs based on tetrakis(4-aminophenyl) silsesquioxane with accessible surface area for H_2 molecule (6,755 $m^2 g^{-1}$) show the hydrogen adsorption capacity up to 51.43 wt% at 77 K and 8.58 wt% at 298 K [337]. In order to increase the heat of H_2 adsorption, post-synthesis modification is a feasible strategy to introduce metals into the polymer. Deng and coworkers [338] showed that after introducing 0.5 wt% lithium into the CMPs produced from 1,3,5-triethynylbenzene, the H_2 storage capacity increases from 1.6 wt% for the CMP to 6.1 wt% for the Li-CMP at and 77 K and 1 atm. The storage capacity of CMP can be increased by nearly four times by introducing only 0.5 wt% lithium. Due to the advantages of narrow pore size distribution and high specific surface area, POPs exhibit their competitiveness in H_2 adsorption. However, because H_2 adsorption performance data are measured generally at low temperatures and the research on controlled H_2 release is still lacking in recent works, there is still a long way for POPs' industrial applications.

With the massive consumption of fossil fuels, CO_2 is in large quantities, resulting in the serious greenhouse effect. Effectively capturing and separating carbon dioxide can greatly reduce the impact of the greenhouse effect. The adsorption of CO_2 was studied by using POPs as adsorbents through physical adsorption. POPs not only have high specific surface areas and good porosity to meet the requirements of CO_2 physical adsorption, but could also be easily modified to introduce heteroatoms to increase the heat of CO_2 adsorption. Generally, heteroatoms (N, P, S, Si, *etc*.) contained functional groups (imine linkers, triazine rings, carbazoles, porphyrins, *etc*.) are most commonly introduced into POPs to improve the CO_2 adsorption performance [339–341]. For example, the N-containing heterocyclic structures of polycarbazole materials greatly improve the adsorption abilities of CO_2. Han and coworkers [49] synthesized a polycarbazole material with S_{BET} as high as 2,200 $m^2 g^{-1}$ by

Table 2 POPs for gas adsorption

Material	Gas	Pressure (bar)	*T* (K)	Uptake (wt%)	Reference
PAF-1	H_2	48	77	7.0	
PAF-3	H_2	1	77	2.07	[91]
PAF-4	H_2	1	77	1.50	
Li-CMP(0.5%)	H_2	1	77	6.1	[338]
CPOP-1	CO_2	1	273	21	[49]
P-PCz-3	CO_2	1	273	25	[342]
FCTF-1-600	CO_2	1	273	24	[188]
5%_Li@PAF-1	CO_2	1.22	273	39	[345]
DHF_PAF-1	CO_2	1	298	40	[346]
DArE@PAF-1	CO_2	1	273	26	[347]
FcTz-POP	I_2	1	348	396	[348]
BpTz-POP	I_2	1	348	216	[348]
AzoPPN	I_2	1	350	290	[349]
CMHPs-5	I_2	1	353	261	[350]
K-PAF-1-750	CH_4	1	77	3.06	[352]
COF-10	NH_3	1	298	25.5	[353]
[CaOOC]17-COF	NH_3	1	283	33.6	[358]
Cu@PIP-X	NH_3	1	298	17.3	[359]
$CaCl_2$@COF-34%	NH_3	1	298	45.0	[360]
TpBD-$(SO_3H)_2$	NH_3	1	298	19.6	[361]

using 1,3,5-tri(9-carbazolyl)-benzene as the monomer, whose adsorption capacity for CO_2 is about 21 wt% under the condition of 1.0 bar and 273 K. Under the same measurement conditions, the value of adsorption capacity for CO_2 increases to about 25 wt% by using polycarbazole derived from 2,6-di(9*H*-carbazol-9-yl)pyridine as the monomer [342]. Besides polycarbazole materials, CTFs, as another kind of N-rich POPs, are a kind of competitive candidates for CO_2 adsorption. Han and coworkers [188] reported the value of CO_2 adsorption is up to 24 wt% by using a perfluorinated covalent triazine-based framework, which benefits from electrostatic interactions between polar C–F bonds and CO_2. In order to improve affinity towards CO_2, Yu and coworkers [343,344] developed a series of modifications of the pore surface for POPs by anchored carboxylic acid groups and amide derivatives. Although the introduction of metal elements reduces the S_{BET}, the introduced metal is conducive to the further conversion of the adsorbed CO_2. Furthermore, porous polycarbazole is employed as rhenium support and improves light absorption abilities for photocatalytic CO_2 conversion [54].

In order to achieve high adsorption capacity at low CO_2 concentration (the CO_2 concentration in the atmosphere is below 400 ppm), the pore chemistry of PAF materials needs to be regulated to strengthen the dipole-quadrupole interactions. Hill and coworkers [345] decorated lithium atoms on the pore surface of PAF-1 (Li@PAF-1) to improve the polarity of the pore surface. Based on the delocalized charged surface, the resulting Li@PAF-1 exhibited high capacities for various gas molecules, with an increase of 22% for H_2, 71% for CH_4, and 320% for CO_2 (20%) as compared to the parent PAF-1. Subsequently, different functional groups, including methoxyl, amine, and dihydrofuran, have been proposed for the decoration of the PAF inner surface [346]. The introduction of such functional groups can effectively increase the adsorption capacity of carbon dioxide and other gases. At the same time, the open cavities of the PAF can be utilized to physically incorporate simulated-responsive molecules, like diarylethene (DArE). Due to the open framework of PAF-1, the DArE loading amount of 5% mass ratio has led to a significantly enhanced CO_2 capacity at 1 bar (Figure 23) [347].

Besides H_2 and CO_2, POPs were also reported in the adsorption of other vapors, such as I_2 and CH_4. The performance of iodine capture of the ferrocene-functionalized POP (named FcTz-POP) and the ferrocene-free reference POP (named BpTz-POP) was measured by Yu and coworkers [348]. By adding the ferrocene building block, FcTz-POP shows the value of I_2 adsorption capacity as high as 396 wt%, which is much higher than that of BpTz-POP at 348 K and atmospheric pressure. Han and coworkers [349] constructed a porous azo-bridged porphyrin-phthalocyanine network (AzoPPN) by a catalyst-free coupling reaction between free-base 5,10,15,20-tetrakis(4-nitrophenyl)-porphyrin and nickel tetraaminophthlocyanine. AzoPPN displays excellent adsorption of iodine vapor up to 290 wt% because of a per-

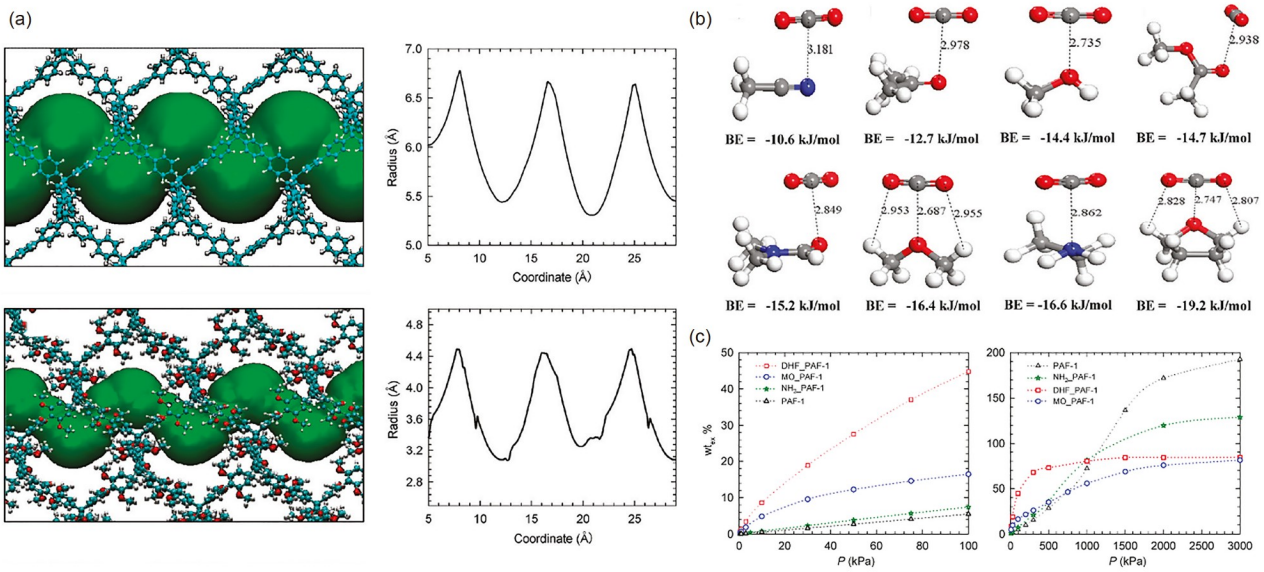

Figure 23 (a) Channel morphologies and radius of the channel along the *XY* plane in the crystalline model: PAF-1 and MO_PAF-1. (b) Optimized conformations and binding energies (BE, defined as the energy of the complex minus the energy sum of CO_2 and the functional group) of CO_2 with model functional groups: acetonitrile, acetone, methanol, methyl acetate, dimethylformamide, dimethyl ether, ethylamine, and tetrahydrofuran, calculated at the MP2/TZVP level of theory. The bond lengths are in units of angstroms. Key: C, gray; O, red; N, blue; H, white. (c) CO_2 adsorption isotherms at 298 K in PAF-1 and the three functionalized PAF-1 based on the crystalline model [347]. Copyright 2011, American Chemical Society (color online).

manent porous structure and plenty of porphyrin and phthalocyanine units in the skeleton as effective sorption sites. Owing to extended π-conjugation, and inherent porosity, conjugated mesoporous hypercrosslinked polymers prepared by Hu and coworkers [350] *via* silicon-promoted cationic polymerization show an adsorption capacity of 133.5 wt% for dibenzothiophene and 261 wt% for I_2.

Methane has a high hydrogen mass ratio, serving as an ideal clean gaseous fuel. Based on the grand canonical Monte Carlo calculation, PAF materials (PAF-1 derivatives) were determined to be an excellent candidate for the accommodation of methane molecules [351]. An excellent adsorbent material was prepared by a KOH-activated PAF-1 precursor, named as K-PAF-1-600 [352]. The carbonized PAF-1 implements a high isosteric heat of adsorption (Q_{st}) with a value of 18.9 kJ mol^{-1}, leading to an excellent capacity for CH_4 molecules.

Ammonia (NH_3) is a commonly used industrial gas that can lead to both environmental and industrial concerns. The capture of NH_3 is also studied by taking POPs as adsorbents. Yaghi and coworkers [353] prepared COF-10 to realize the highest uptake capacity (15 mol kg^{-1}) at that time, through the generation of classical ammonia-borane coordinative bond. Afterwards, some POP materials were also presented to capture NH_3 for environmental protection [354–357]. Recently, many efforts have been made by Chinese researchers. Zhu and coworkers [358] designed a series of metal-COF, named as [MOOC]17-COF (M=Ca^{2+}, Mn^{2+}, and Sr^{2+}). These M-COF realized excellent adsorption capacities of NH_3 (as high as 19.8 mol kg^{-1}) through synergistic multivariate and open metal site approaches. Similarly, metal-PAF (Cu@PIP-X) [359], and metal-COF ($CaCl_2$@COF) [360] were also prepared. The $CaCl_2$@COF-34% prepared by Wang and coworkers exhibited record ammonia adsorption ability (26.5 mol kg^{-1}), due to the homogeneous dispersion of $CaCl_2$ in the COF structure, and the interaction between NH_3 and Ca^{2+}, and NH_3 and Cl^-. Furthermore, Li and coworkers [361] synthesized an ultra-stable sulfuric acid COF (named as TpBD-$(SO_3H)_2$) that showed great ammonia capture ability in harsh environments.

4.1.2 Chemical substance adsorption

The adsorption capability of POPs for various chemicals at room temperature shows the industrial application prospects. For some solvent molecules, the hydrophilicity/hydrophobicity provided by modifying POPs with functional groups can affect the adsorption performance of POPs. In the report by Tan and coworkers [362], owing to a large degree of retained porosity after suitable solvent evaporating, a soluble porous organic polymer (S_{BET} of up to 646 m^2 g^{-1}) synthesized by polymerization of dichlorodiphenylmethane show high drug loading efficiency (1.91 g per gram of ibuprofen), which is much higher than that of traditional non-soluble POPs.

Pollutant adsorption is another important application of POPs. Highly branched PAF-P5 was prepared by Wen and coworkers [363] for adsorbing and removing organic pollutants (short-chain alkyl derivatives including *n*-BuOH, *n*-$BuNH_2$, and *n*-$ProCO_2H$; pesticide molecules including methomyl, omethoate, and trichlorfon) from water with high

removal efficiency. Furthermore, there are some impressive examples that POPs can be utilized in the adsorption of hormones, which are produced in personal daily necessities and food processing and become emerging pollutant molecules recently [364].

The large specific surface area, high porosity, and feasible modifiability of POPs show obvious advantages for dye adsorption, such as methyl blue, Rhodamine B, and methyl orange. Planar monomers with multiple phenolic hydroxyl groups promote the formation of POPs (named as CTT-POP) with porous structure, flake morphology, good surface wettability, and high functionality. These structural features of the CTT-POP adsorbent provide the rapid adsorption of methylene blue dye from water [365]. By using ethanolamine- and amine-functionalized porous cyclodextrin polymers, Zhang and coworkers [366] demonstrated that size and hydrophilicity matching between porous skeletons and dye molecules improves the adsorption performance. In addition, in order to increase the electrostatic interaction between the dye molecules and the pores, Zhang and coworkers [367] developed an ionized aromatization approach to charged porous polymers, thus enhancing the adsorption performance of various kinds of dye molecules.

4.2 Separation

POPs dominated by micropores generally show a narrow pore size distribution, which possesses good application prospects in gas phase separation and liquid phase separation in the form of powders or membranes. POPs in powder form are simple to prepare and easy to be functionalized, which endows POPs with a high potential to be applied in gas separation. In addition, meeting the requirements of reusability and low energy consumption, membrane separation represents one of the most advanced separation technologies. The pore size distribution of POP membranes can be customized through the design of monomers' shapes and sizes, which makes POP membranes become promising porous membranes for separation. POPs in the forms of both powder and membrane provide important references for the development of separation materials owing to their stability and long cycle life.

4.2.1 Gas phase separation

The purification of gases is of great significance for industrial applications. Physical separations for N_2, CO_2, H_2, CH_4, *etc*. are related to the pore size distribution of the porous materials owing to the sizes of the gas molecules. In fact, most POPs with a high S_{BET} value and a large micropore volume generally show the ability to adsorb light gases. Nevertheless, the selective adsorption, that is separation, of these mixed gases requests narrow pore size distribution and precise functional sites for POPs. So far, practical strategies including the design of regular building blocks, synthesis of topological networks, and the modification of functional groups have been reported on POP separation materials (Table 3).

As a type of ideal clean energy gas, only H_2 with high purity is safe in practical application. The separation of H_2 with the smallest size from mixed gases may rely on the molecular sieve effect. A flexible-tuned rigid network strategy has been reported by Wang and coworkers (Figure 24a) [65]. In detail, rigid monomers and flexible monomers were selected to produce flexible and independent molecular

Table 3 POPs for gas separation

Material	Gas type	Pressure (bar)	*T* (K)	Separation Selectivity	Reference
P33DT-ThC$_4$	H_2/CO_2	1	298	50	[65]
[COF-300]- [Zn_2(bdc)$_2$(dabco)]	H_2/CO_2	1	298	12.6	[368]
[COF-300]-[ZIF-8]	H_2/CO_2	1	298	13.5	[368]
C1M2-Al	CO_2/N_2	1	273	32.3	[370]
pCage-1	CO_2/N_2	1	273	17.6	[371]
pCage-2	CO_2/N_2	1	273	19.8	[371]
CMP–CSU13	CO_2/N_2	1	273	223	[372]
MAPDA	CO_2/N_2	1	298	18.9	[373]
MAPDA/PIM-1	CO_2/N_2	1	298	23.9	[373]
MMP-3/mPSf	CO_2/N_2	1	298	78	[374]
PIM-TPFC–CH_2NH_2–15 MMM	CO_2/N_2	1	273	45.9	[375]
	CO_2/CH_4	1	273	36.4	
IUPs	C_2H_2/C_2H_4	1	298	474.4	[376]
CTF-PO71	C_2H_2/C_2H_4	1	298	246	[377]
PAF-120	C_2H_2/C_2H_4	1	298	4.8	[378]
	CO_2/N_2	1	298	52	

sieve membranes through electropolymerization. The separation performance of these membranes for H_2/CO_2, H_2/N_2, and H_2/CH_4 exceeds the Robeson upper limit. Among these applications, H_2/CO_2 separation selectivity reaches 50 with 626 barrer of H_2 permeability. Long-term service life and chemical stability tests reveal that these POP materials have the potential for industrial applications. In order to meet the processing requirements of high-performance H_2 separation membranes, coordination polymer glasses have also been developed with machinability and self-healing ability [294]. In addition, the introduction of POPs into composite materials is considered a promising approach for the separation of H_2. In a work reported by Ben and coworkers [368], the interlayer was formed by amorphous MOF between crystalline COF and MOF as shown in Figure 24b. The amorphous layer possesses a pore size similar to that of the corresponding crystalline MOF and occupies the gaps of the COF nanocrystals and the interface between COF and MOF crystalline layers. Thus, COF-MOF composite membranes demonstrate higher separation selectivity of H_2/CO_2 gas mixtures than the individual COF or MOF membrane due to the synergy between two porous materials.

POP membranes used in gas separation are also impressive in CO_2 separation. The selective separation of CO_2 from N_2, CH_4, *etc*. is extensively studied. The difficulty in the selective capture of CO_2 is led by their small kinetic diameter (0.33 nm). Therefore, a feasible strategy in principle is the design and synthesis of POPs with corresponding pore size distribution. A series of HCPs with excellent physical/chemical stability have been designed and prepared by Yuan and coworkers [370]. The optimized polymer (named as C1M2-Al) with BET-specific surface area up to 1,783 $m^2 g^{-1}$ possesses the best CO_2/N_2 (15/85) selectivity at 273 K and 1 bar. In order to prepare ideal CO_2 separation materials, the design of POPs with controllable porosities and gas adsorption properties is a feasible strategy. Zhang and coworkers [371] synthesized organic cage frameworks with fixed pore sizes to tune porous properties and improve CO_2 capture *via* molecular engineering. Besides reasonable pore size distribution, the enhancement of interaction between POPs and CO_2 is another strategy for CO_2 separation. Yu and coworkers [372] introduced thiophene and triazine units to enhance host-guest interactions so that the functionalized POPs show high CO_2 selectivity adsorption. In short, size selectivity and the interaction between CO_2 molecules and POPs work mostly on selective separation for CO_2 purification.

To synthesize CO_2 separation membranes, Zou and coworkers [373] selected melamine and 1,4-piperazine dicarboxaldehyde to prepare a POP (named as MAPDA) with an S_{BET} of 548 $m^2 g^{-1}$ and a pore diameter of about 1.0 nm. Subsequently, the MAPDA (15 wt%) was blended with the PIM-1 soluble matrix to prepare MAPDA/PIM-1-mixed matrix membranes. A single gas permeation experiment shows that the CO_2 permeability increases significantly from 3,694.5 barrer for MAPDA to 7,861.9 barrer for MAPDA/PIM-1 and the CO_2/N_2 selectivity increases from 18.9 for MAPDA to 23.9 for MAPDA/PIM-1. High porosity and molecular affinity are the main factors to improve CO_2 permeability and CO_2/N_2 selectivity. Zhong and coworkers [374] synthesized a porous polymer by a polymer-oriented

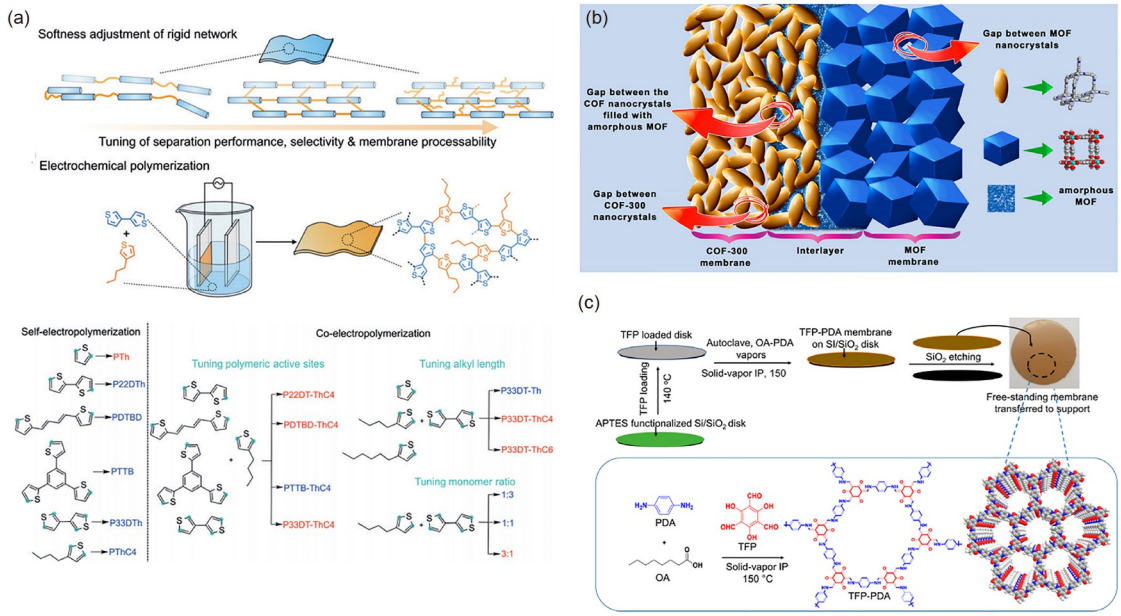

Figure 24 (a) Tuning of processability by incorporating softness into a rigid network *via* co-electropolymerization, and lists of monomers with different rigidity, softness, and polymeric active sites [65]. (b) Schematic illustration of the interlayer formed by amorphous MOF between crystalline COF and MOF [368]. (c) Schematic illustration of solid-vapor method for membrane growth and HF etching step to obtain free-standing membrane [369] (color online).

chemical synthesis method with good crystal and framework size controllability and hydrolytic stability. Specifically, small organic connectors were first matched with metal ions, and the resulting units then self-assembled along the extension of the polymer chains to construct 3D frameworks. The microporous polymer dispersion was coated on a modified polysulfone substrate to prepare a microporous polymer/polysulfone membrane with an ultra-thin selective layer with a thickness of less than 50 nm and a surface area of more than 100 cm^2. Under humid and dry gas feed conditions, microporous polymers show promising CO_2 membrane separation performance with high CO_2 permeability (3,000 gas permeance units) and stable CO_2/N_2 selectivity (78). Generally, traditional POPs exhibit insoluble and infusible characteristics, thus lacking processability. Luckily, the successful preparation of PIMs membranes has allowed POPs to become processable. According to the report of Liu and coworkers [375], a series of mixed matrix membranes based on the PIM-1 matrix for CO_2 separation were prepared. The measurement results show that mixed matrix membranes possess CO_2 permeability of 7,730 barrer, and the selectivity of CO_2/N_2 and CO_2/CH_4 gas pairs are 45.9 and 36.4, respectively.

Another important challenge in gas separation is the selective separation between alkynes, alkenes, and alkanes. Owing to the similar molecular sizes and interactions with POPs during separation, it is particularly difficult to separate the specific gas from the mixed gases including alkynes, alkenes, and alkanes with high selectivity. However, several kinds of POPs still exhibit promising results in this application field. An ionic ultra-microporous polymer (named as IUPs) with high-density inorganic salt distribution was polymerized by Xing and coworkers [376] through the ionic double cross-linking strategy. The gas diffusion isotherms and experimental curves prove that IUPs own exceptional selectivity (474.4) for separating acetylene from ethylene along with high thermal and hydraulic stability. The electric charge effect plays a vital role in the separation process. A new type of CTF (named as CTF-PO71) was designed and prepared for high-efficiency gas separation by Han and coworkers [377]. The functionalized sites with different electrostatic potentials on the pores of CTF-PO71 propel it to show a strong interaction with acetylene (C_2H_2), thereby making C_2H_2 adsorbed preferentially than ethylene (C_2H_4). Furthermore, capturing trace amounts of C_2H_2 from the gas mixture by using CTF-PO71 is also effective. The crystalline framework and uniform pore size distribution are meaningful for gas separation. In this respect, the 2D polyimide POPs (named as PAF-120) were constructed by Ren and coworkers [378], which show significant selective adsorption of C_2H_2 over C_2H_4 and CO_2 over N_2. These results provide the guiding suggestion for designing POPs for separation between alkynes, alkenes, and alkanes.

POPs can also be used as the stationary phases of gas chiral chromatography. Yan and coworkers [176] reported a method for the direct growth of chiral COFs (named as CTpPa-1, CTpPa-2, and CTpBD) in the capillary columns of gas chromatography. The chiral COF-bonded columns exhibited high resolution for the separation of enantiomers, in which chiral COFs showed stronger interaction with (+)-enantiomers rather than (−)-enantiomers. Thus, the chiral separation was realized by the driving of enthalpy. A β-cyclodextrin COF (β-CD-COF) was also designed by Luo and coworkers [379] for gas chiral chromatography. The COF functional capillary column exhibited good resolution of chiral alcohols, aldehydes, ethers, and amino acid derivatives, with good repeatability and reproducibility.

4.2.2 Liquid phase separation

Similar to gas separation, the physical separation of mixed liquids by using POPs as separation materials is another promising direction for achieving industrial applications. The high efficiency of liquid phase separation depends on not only pore size distribution but also the interaction between the purified liquid and the POPs. Notably, POPs are generally applied to liquid phase separation in the form of membranes.

Liquid phase separation based on shape and size effects is the most common strategy. POP membranes with designable pore size exhibit advantages for utilization in this separation method. A series of CMP membranes were prepared through Sonogashira-Hagihara reaction between 1,3,5-triethynylbenzene and three different dibromobenzenes *via* surface-initiated polymerization strategy by Tang and coworkers [297]. The main chains of the membranes are composed of a fully rigid conjugated skeleton, and thus the membrane possesses high resistance to organic solvents. The results of separation measurements show that the CMP membrane with a thickness of 42 nm based on polyacrylonitrile has good solute retention and broad-spectrum nanofiltration performance in both non-polar *n*-hexane and polar methanol, and the permeability reaches 32 and 221 L m^{-2} h^{-1} bar^{-1}, respectively. Both experiments and simulations verify that the property of the CMP film is derived from the open and interconnected voids formed in the highly rigid network. The aromatic porous polymer network membranes (*p*-PPN, *m*-PPN, and *tri*-PPN) were prepared *via* the *in-situ* Aldol three-condensation cross-linking method by Fang and coworkers and show high stability, permeability, and obvious selectivity for Rhodamine B in organic solvent nanofiltration. Benefiting from the aromatic nature of the main chains, high S_{BET} (up to 1,235 m^2 g^{-1}), and narrow pore size distribution, they have high permeability to organic solvents. In terms of dye separation for Rhodamine B over Bromothymol Blue, Congo Red, and Brilliant Blue, the molecular weight cut-off value and molecular weight retention value of the *p*-PPN are 600

and 350 g mol^{-1}, respectively. Due to the high stability of the aromatic skeleton, these films still maintain structural integrity and organic solvent nanofiltration performance in the presence of strong acids or bases for more than 50 h [47].

Interfacial polymerization is the synthesis method of most POP membranes. A lot of works were reported on the synthesis of POP membranes at the liquid-liquid interface, the solid-liquid interface, and the gas-liquid interface. For example, a highly crystalline 2D COF membrane with 120 nm thickness was prepared using solid-gas interface engineering in 9 h by Jiang and coworkers [369] (Figure 24c). Owing to the ultra-thin thickness and the ordered pores, the membrane exhibits ultra-high permeability (411 L m^{-2} h^{-1} bar^{-1} for water, and 583 L m^{-2} h^{-1} bar^{-1} for acetonitrile), and good rejection for dye molecules with size greater than 1.4 nm. The interface growth of the membrane still has several processing problems to be solved before practical application, such as membrane transfer and substrate selection.

Post-synthesis modification to enhance the interaction between POPs and solvent molecules is a common strategy for liquid phase separation. In this regard, to develop membrane distillation membranes composed of vertically arranged hydrophilic gradient channels, imine bonds of a COF membrane (synthesized by covalently linking 2,5-dihydroxy-1,4-benzenedicarboxaldehyde and 1,3,5-tris(4-aminophenyl)-benzene) were removed partially by Wang and coworkers [293]. This functionalized change including pore size and hydrophilicity in a single channel achieves selective water transport paths and precise liquid-vapor phase change interfaces. In addition to the anti-pollution and anti-wetting ability of the COF membrane on the support layer, the membrane flux is 600 L m^{-2} h^{-1} at a feed temperature of 85 °C and absolute pressure of 16 kPa. It is three times the most advanced membrane distillation membrane used for seawater desalination. POPs with a layered structure, such as 2D COFs, can be exfoliated into membranes with a thickness of several nanometers [380]. These nanosheets can be used to prepare pure membranes and mixed matrix membranes for separation applications. Jiang and coworkers [381] prepared the COF nanosheets (named CON TpHz, CON TpPa, and CON TpBD) with pore structure by exfoliation. Subsequently, transition metal ions are loaded on the pore walls to promote the transportation process of ordered channels. The optimized transport membrane shows separation performance for gasoline desulfurization with a permeation flux of 21.6 kg m^{-2} h^{-1} and an enrichment factor of 6.29. The long-term operational stability and enhanced anti-swelling performance indicate the excellent stability of the resulting membranes.

The cations and anions can be separated according to the electrostatic forces between POPs and various ions. According to Liu and coworkers [382], crosslinked polyethyleneimine was grafted on a carboxylated carbon nanotube intermediate layer incorporated into the macroporous cellulose acetate substrate to form the composite POP membrane. A hydrophilic and positively charged POP membrane is functionalized by the inorganic modification through the *in-situ* surface reaction of zinc nitrate and superfluous ammonium hydroxide. Therefore, the functionalized POP membrane enhances the interaction between the polymers and the carbon nanotube interlayers, thereby giving them mechanical strength and maintaining the membrane pore structure during the pressure-driven filtration process. The functionalized POP membrane possesses pure water flux up to 16.5 L m^{-2} h^{-1} bar^{-1}. Meanwhile, the membrane shows good nanofiltration performance for divalent cations due to the electrostatic repulsion generated by the repulsion effect. The mechanism of ion separation could inspire the investigation of material design and synthesis to meet the separation requirements in different application scenarios.

4.2.3 Extraction of radioactive substances

Compared to other porous materials, PAF materials are distinctive for their outstanding structural stability. This feature allows it to perform well in many extreme operating conditions. Uranium is an important raw material for the nuclear industry. With the continuous development of the nuclear energy industry, the demand for raw materials is gradually increasing. However, the land reserve is running out in the foreseeable future. In comparison, the seawater contains the largest amount of uranium on earth. The efficient extraction of uranyl ions from seawater could meet the energy needs for nearly thousands of years. At present, the widely used polymer adsorbents cannot meet the demand for uranium extraction because of the relatively low embedding of adsorption sites. To increase accessible adsorbing sites, Ma's research group [383] used PAF-1 as the scaffold and decorated the amidoxime groups on the porous network. The amidoxime-functionalized PAF-1 exhibited an ultra-high ion adsorption capacity of 304 mg g^{-1}. In seawater, the uranium content is below 3.3 ppb and many interfering elements existed. To improve the selectivity of uranium, the molecular imprinting strategy is capable of constructing PAF architecture with selective U-binding sites. Due to the synergistic interactions of salicylaldoxime, carboxylic, and pyridine groups, MIPAF materials presented a high capacity and ultra-large selectivity coefficient for uranyl ion capture [109]. Further improvement to accelerate the U species diffusion was achieved by introducing conductive polymer chains into the channels of PAF materials, namely PPA@MISS-PAF-1. After the electric field was applied as an external driven force, the conductive polymer chains enriched a large number of metal ions into the porous material, thereby increasing the local concentration of the uranyl ions by 150%–250%. The PPA@MISS-PAF-1 showed 100–1,000 fold improve-

ment in kinetics as compared with the polymer adsorbents, achieving the highest uranyl ion extraction performance at that time (Figure 25) [384]. Recently, in order to avoid the defect that the pore channels are blocked by polymer chains, a porous graphene-based adsorbent was constructed. Based on the synergistic effect of electrostatic attraction and nanofluidic channels, the graphene-based adsorbent implemented a massive extraction of uranyl ions from natural seawater (~16 mg g^{-1} in 56 days) [385].

Qiu *et al*. [146] presented two COFs, NDA-TN, and BDA-TN, with corresponding BET surface areas of 1,124.3 and 1,070.4 $m^2 g^{-1}$, respectively. Afterward, NDA-TN and BDA-TN were further post-functionalized by the treatment with $N(CH_2CH_3)_3$ and $NH_2OH{\cdot}HCl$ to convert cyano groups to amidoxime groups, the functionalized COFs were denoted as NDA-TN-AO and BDA-TN-AO, respectively. The PXRD patterns exhibit similar diffraction patterns to the original COFs, suggesting preserved crystallinity. However, the surface areas declined to 820.9 and 789.3 $m^2 g^{-1}$, respectively, reasonably associated with the addition of larger substituents in the pores. Besides, the as-prepared COFs show remarkable chemical stability under harsh conditions like acid, base, or γ radiation. Due to the excellent semiconductive properties of NDA-TN-AO and BDA-TN-AO, they were applied for selective photo-induced uranium adsorption from seawater. In a typical photo-induced process, COFs can efficiently release electrons from the scaffold, reducing U(VI) to insoluble U(IV). Simultaneously, this process renders a positive surface electric field which forms intensive electrostatic interactions with $[UO_2(CO_3)_3]^{4-}$. Especially, the NDA-TN-AO significantly outperformed BDA-TN-AO in the photoreduction of uranium, which can be rationally attributed to its fully conjugated skeleton and more efficient pathways for the transfer of photoinduced electrons. Particularly, the remarkable photocatalytic activity of NDA-TN-AO enables the effective extermination of bacterial and biological entities by generating biotoxic reactive oxygen species (ROS), thus facilitating a more efficient reduction of uranium by the photoelectrons. Upon a similar strategy, they also reported a triazine-based cyanovinylene-linked COF termed BTA, and its derivative COF treated with $NH_2OH{\cdot}HCl$, showing good absorption to UO_2^{2+} with a high capacity of up to 427 mg g^{-1} [147].

4.3 Chemocatalysis

We highlight herein the application of POPs-based catalysts in representative organic transformations, such as coupling

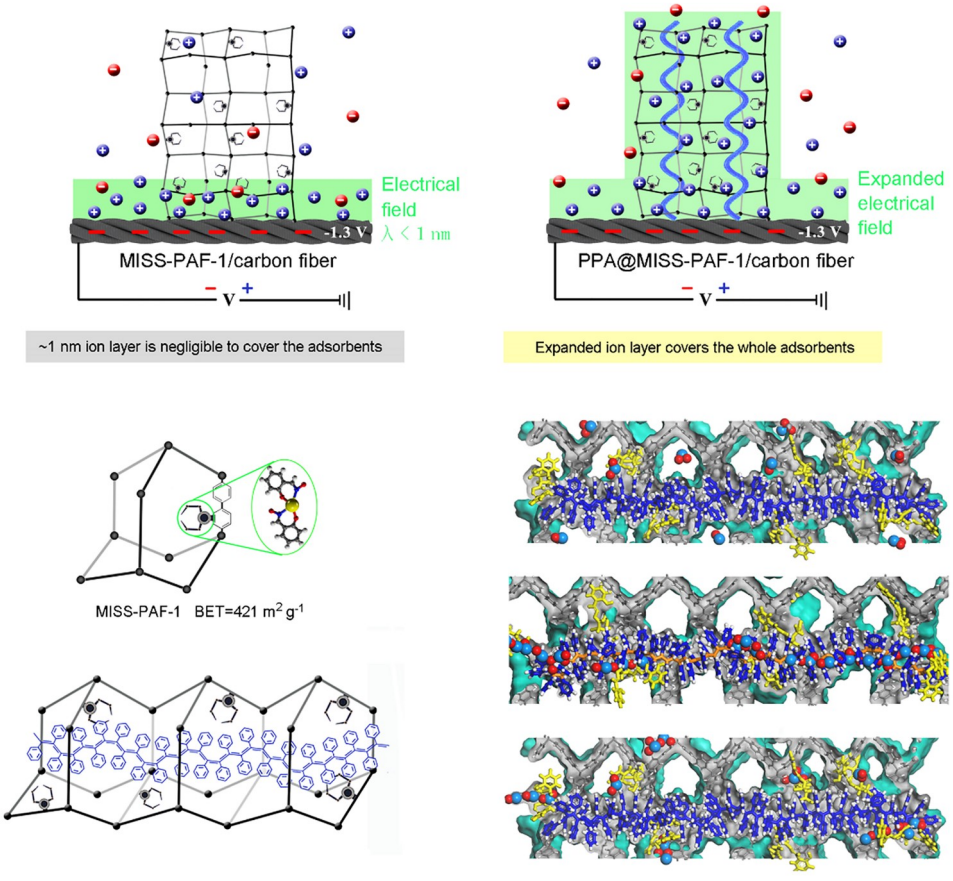

Figure 25 Design and synthesis of PPA@MISS-PAF-1 and adsorption process in asymmetrical alternating current electrochemical (AACE) extraction [384] (color online).

reactions, catalytic asymmetric reactions, alkene and alkyne transformation, and CO_2 fixation. Coupling reactions and catalytic asymmetric reactions represent the highest controllability of catalytic activity and selectivity in modern catalysis. The activation and selective transformation of alkene, alkyne, and CO_2 lie at the frontiers of catalysis research because of their academic and industrial value, *i.e.*, these raw materials are always inert and easily available. However, the development of efficient heterogeneous catalysts is still highly expected for industrial applications. In this context, the flourishing of POPs research has provided new opportunities for the innovation of heterogeneous catalysis.

In the past two decades, the rapid emergence of new knowledge and expertise to explore POPs for heterogeneous catalysis indicates that the field is stepping to maturity. Researchers in China have made great contributions to this field by exploring important POPs-based catalytic systems (Figure 26).

4.3.1 Coupling reactions

Transition metal-catalyzed coupling reactions represent the most direct protocol to build the scaffold of organic molecules. To illustrate, C–C, C–X (X=O, S, N, *etc.*) coupling reactions are particularly relevant in organic synthesis. POPs-based organometallic catalysts for coupling reactions have been widely explored by researchers in China (Figure 27).

Suzuki-Miyaura coupling reaction. Palladium-catalyzed Suzuki-Miyaura cross-coupling reactions have been recognized as efficient and practical methods to construct C–C bonds between arylboronic acids and aryl halides. POPs can be the idealized platform for the heterogenization of these palladium catalysts in Suzuki-Miyaura cross-coupling reactions.

In 2011, Wang and coworkers [18] achieved the first case of catalytic application in COFs. Based on the construction of the first 2D imine COF, that is COF-LZU1, palladium acetate was successfully introduced into COF-LZU1 for the formation of the catalyst, namely, Pd/COF-LZU1. Notably, the crystalline structure of COF-LZU1 allowed for confirmation of the location of $Pd(OAc)_2$, which is coordinated with two nitrogen atoms (distance of ~3.7 Å) from adjacent layers of COF-LZU1. Pd/COF-LZU1 showed good performance in catalyzing the Suzuki-Miyaura coupling reaction. The broad scope of reactants can be transformed with excellent yield (up to 98%). Pd/COF-LZU1 showed high stability and good recyclability. The catalytic activity and crystallinity of Pd/COF-LZU1 can be retained after five runs.

Guo and coworkers [386] synthesized a highly dispersed spherical CMP material (CNPCs) in microemulsion. The presence of micropores and mesopores in CNPCs is conducive to the uniform isolation and dispersion of palladium nanoparticles (Pd NPs) in CNPCs. The as-prepared Pd@CNPC catalyst showed excellent catalytic activity (TOF=44,100 h^{-1}) for the Suzuki-Miyaura coupling reaction and can be recycled five times without a decrease in catalytic

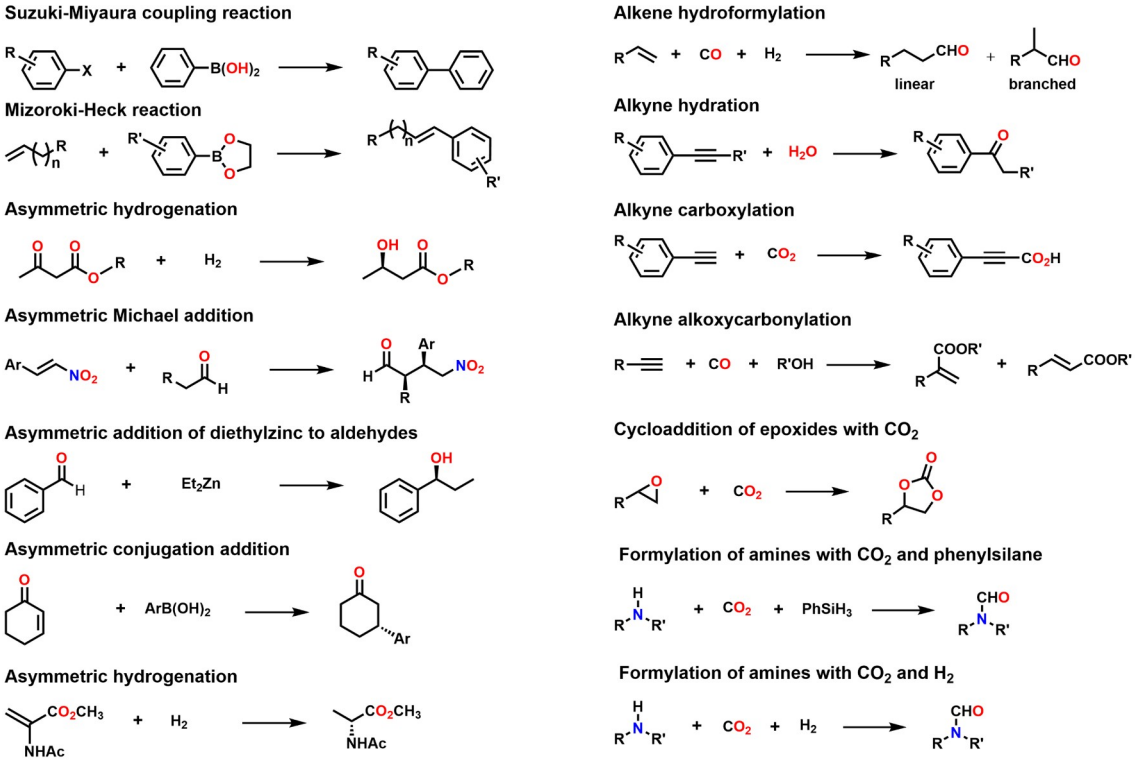

Figure 26 Representative reactions catalyzed by POP catalysts (color online).

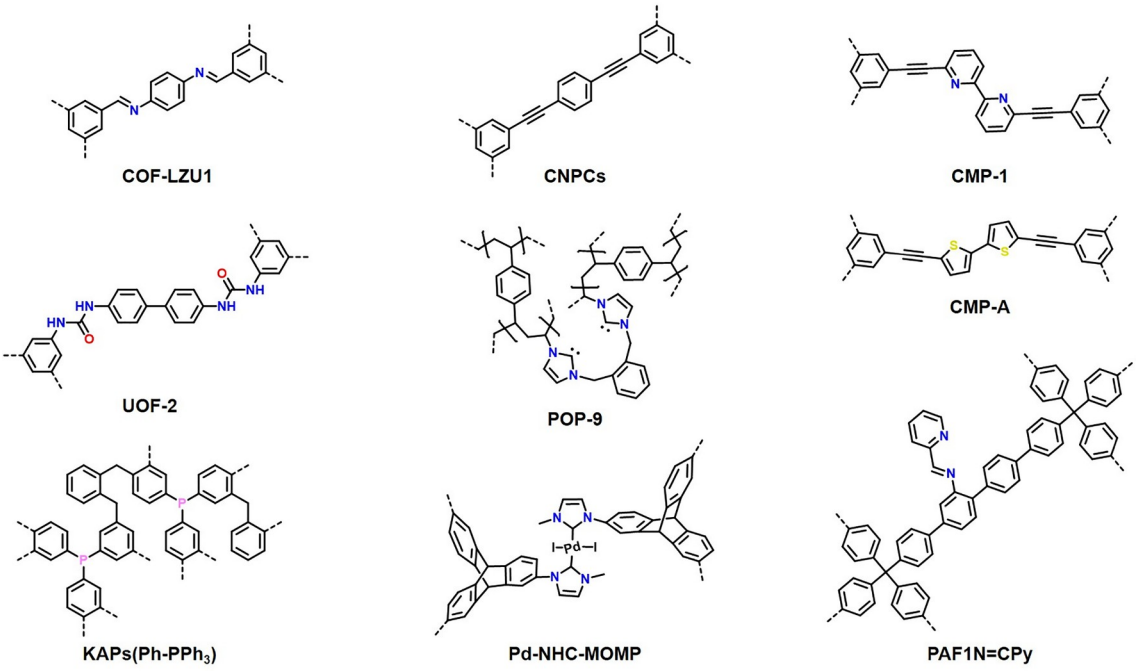

Figure 27 POP catalysts developed in China for coupling reactions (color online).

activity. Wang and coworkers [387] embedded the Pd NPs into urea-functionalized POPs. The presence of urea moiety can help to anchor Pd NPs and increase the hydrophilicity of the catalyst, so as to conduct Suzuki-Miyaura cross-coupling reactions in pure water at room temperature. The catalyst exhibited high activity (up to quantitative yield) and can be recycled four times.

In 2013, Zhang and coworkers [388] prepared a Pd-NHC-MOMP catalyst where palladium species was coordinated to *N*-heterocyclic carbene (NHC)-functionalized POP. The catalyst could efficiently conduct Suzuki-Miyaura coupling reaction with high activity (up to 97% conversion).

In 2018, Zhu and coworkers [389] successfully synthesized PAF70-Pd by introducing $Pd(OAc)_2$ into PAF70-NH_2. PAF70-Pd could catalyze the Suzuki-Miyaura coupling reaction with excellent yields (up to >99%) and high TOF ($\geq$14,700 h^{-1}). The excellent catalytic property of PAF70-Pd could be attributed to its abundant pore space which could facilitate substance diffusion.

The aryl halides applied in the Suzuki-Miyaura coupling reactions mentioned above involved aryl bromides and aryl iodides. The use of aryl chlorides is more promising in the Suzuki-Miyaura coupling reaction because they are more easily available and economical than aryl bromides and aryl iodides. However, the activation of aryl chlorides is particularly challenging as the low reactivity of C–Cl bonds of aryl chlorides in transition-metal-catalyzed systems. Aiming to explore the POPs-based catalytic systems for the use of aryl chloride in Suzuki-Miyaura coupling reactions, it is key to introduce arylphosphine functional groups into porous organic polymers as binding sites for Pd species. The arylphosphine groups can help to realize the high dispersion of Pd active sites to obtain higher catalytic activity.

Therefore, Tan and coworkers [390] accordingly constructed triphenylphosphine-functionalized POP which is cross-linked by benzene and triphenylphosphine (PPh_3) *via* the "knitting" strategy. The enriched and isolated PPh_3 moiety can make Pd species efficiently dispersed, and the strong coordinating ability of the phosphorous atom can help to prevent the loss of Pd. The as-prepared KAPs(Ph-PPh_3)-Pd exhibited excellent activity (up to 99% yield) in catalyzing Suzuki-Miyaura cross-coupling reaction between aryl chlorides and arylboronic acids under the mild conditions and aqueous media. Notably, the catalytic activity of KAPs (Ph-PPh_3)-Pd is much higher than that of the homogeneous catalyst (<20% yield) and can be maintained after five runs.

Mizoroki-Heck reaction. The Mizoroki-Heck reaction provides a powerful strategy to convert vinylic C–H bonds into C–C bonds in the presence of Pd catalysts. The control of regioselectivity for the insertion of C=C double bonds is a key and challenging issue of Mizoroki-Heck reactions.

In 2017, Zhan *et al*. [391] explored a series of bipyridine-based CMPs to serve as support for Pd species. One of the catalysts, denoted as $Pd(OAc)_2$/CMP-1, was prepared *via* the coordination of $Pd(OAc)_2$ in alkyne-linked bipyridine-based CMP. This catalyst showed remarkable regioselectivity in catalyzing the Mizoroki-Heck reaction of electronically unbiased olefins; in detail, the ratio between linear and branched products is up to 100:1, which is significantly higher than that of the homogeneous analogue for CMP-1. The

theoretical calculation revealed that the formation of a linear product is much more preferable than the formation of the branched one. Thus, the confinement effect in the pore structure of CMP-1 should contribute to the high regioselectivity in this catalytic system. Furthermore, they continuously synthesized alkyne-linked thiophene-based CMPs [392]. By coordinating the Pd species, they found that CMP-A, which contained bithiophene and adjacent alkyne skeletons, showed the highest regioselectivity (up to 99% over linear products) in conducting Mizoroki-Heck reaction of electronically unbiased olefins. The synergistic effect in POPs between different coordinating sites (bipyridine or thiophene with alkyne) should be responsible for these efficient and selective transformations.

In 2019, Ding and coworkers [393] reported an elegant example of a reusable heterogeneous catalyst (Pd@POP-9) for controlling the regioselectivity of Heck reactions. Pd@POP-9 was witnessed as a stable mononuclear Pd-based catalyst and featured with fixed chelation angle between the Pd center and NHC ligand. These structural features of Pd@POP-9 would help to prevent the aggregation of Pd species, and to afford the high reactivity and selectivity, *i.e.*, the ratio of the linear products to branched products can be reached 100:1. Besides, Pd@POP-9 can be reused for ten times without the activity loss, which exhibited the high stability of this catalytic system.

4.3.2 *Catalytic asymmetric reactions*

Asymmetric catalysis is a key route to obtaining chiral compounds. However, molecular chiral catalysts are expensive and hard to reuse, limiting the industrial applications of many efficient catalysts in homogeneous systems. Developing highly efficient and easily recycled chiral heterogeneous catalysts is, therefore, an important task to tackle these problems. POPs are featured with high surface area, adjustable pore size, easily modified pore environment, and precise structural modification, which are crucial to incorporate chiral catalytic sites to achieve efficient asymmetric transformation in the heterogeneously catalytic system. Notably, the confinement effect of the pore structure would be conducive to enhancing the steric control for the chirality transfer process. Recently, the rise of COFs endowed more opportunities for the development of asymmetric heterogeneous catalysis; the abundant porosity and periodic pore structure of COFs are commonly regarded as indispensable add-ons for improving the efficiency and selectivity of asymmetric synthesis. Nowadays, scholars in China play a significant role in the research of POPs in asymmetric heterogeneous catalysis (Figure 28).

Asymmetric Michael addition. In 2012, Wang and coworkers [394] achieved the one-pot construction of a chiral porous polymer, that is JH-CPP, which is functionalized by the Jørgensen-Hayashi catalyst. Constructed by a "bottom-up" strategy, JH-CPP possessed a high BET surface area of 881 $m^2 g^{-1}$ and well-dispersed active sites. When conducting the asymmetric Michael addition of aldehydes to nitroalkenes, JH-CPP could give the desired products in good to excellent yield (67%–99%), high enantioselectivity (93%–99% ee), and high diastereoselectivity (d.r. of 74:26 to 97:3).

In 2019, Wang and coworkers [395] further synthesized a

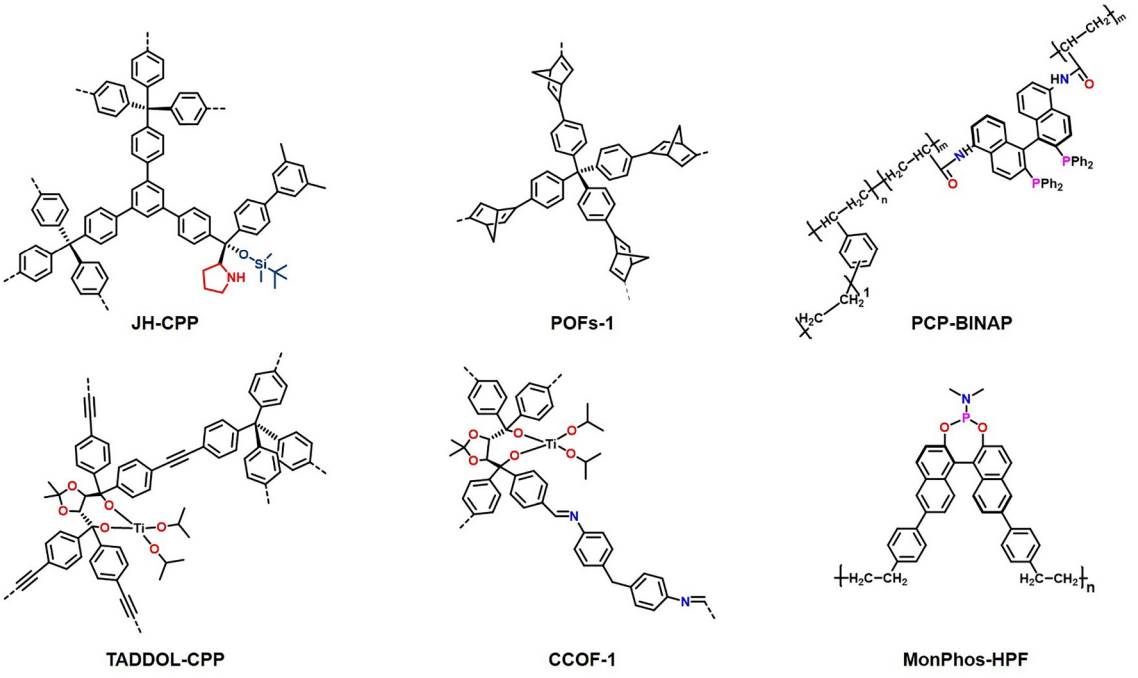

Figure 28 POP catalysts developed in China for catalytic asymmetric reactions (color online).

pyrrolidine-based chiral porous polymer, denoted as Py-CPP, *via* Sonogashira-Hagihara coupling reaction between pyrrolidine-based monomer with tetrakis(4-ethynylphenyl)methane. Py-CPP was applied to catalyze asymmetric Michael addition of aldehydes to nitroalkenes in pure water and showed good performance (up to 98% yield and up to 99% ee). Notably, possessing a three-dimensional pore structure, Py-CPP exhibited much higher activity than that of its linear analog, which reinforced the potential of POPs in asymmetric heterogeneous catalysis. Recently, Cui *et al*. [396] applied the pyrrolidine-based COFs to catalyze the same reaction. It can also give a good yield (up to 96%) and ee value (up to 86%).

Asymmetric hydrogenation. In 2012, Xiao and coworkers [397] incorporated chiral BINAP backbone into POPs through the copolymerization between divinylbenzene and vinyl-functionalized BINAP monomer. After the coordination with ruthenium species, the prepared Ru/PCP-BINAP could serve as a chiral catalyst for asymmetric hydrogenation of β-keto esters with good activity (>99% conversion) and high enantioselectivity (up to 94% ee). The Ru/PCP-BINAP showed good stability and can be recycled six times without obvious activity loss.

Later, Ding and coworkers [398] also achieved the construction of chiral BINAP-based POP through the "knitting strategy". The prepared chiral catalysts, namely, Ru/KAP-1, could give up to >99.5% yield and 98.7% ee for the asymmetric hydrogenation of *β*-keto esters. Ru/KAP-1 can be reused four times without a decrease in activity and with a slight decrease in ee value.

In 2017, Xiao and coworkers [399] successfully introduced chiral BINOL-based phosphoramidite ligands into POPs. The isolation of phosphoramidite moieties in POPs could prevent the self-quenching of active sites. Indeed, Rh/MonPhos-HPF, as one case of these representative catalysts, showed high activity (>99.5% conversion) and high enantioselectivity (up to 97.7% ee) in catalyzing the asymmetric hydrogenation of methyl 2-acetamidoacrylate to afford chiral amino acid derivatives. Notably, when the catalyst loading was in a low concentration (*e.g*., substrate/catalysts=2,000), the activity of Rh/MonoPhos-HPF is at least 5 times higher than that of the homogeneous analogue, which exemplified the superiority of this heterogeneous catalytic system. Rh/MonoPhos-HPF could be recycled at least five times with maintaining the activity and enantioselectivity.

Asymmetric addition of diethylzinc to aldehydes. In 2014, Wang and coworkers [400] synthesized a chiral TADDOL-based CMP, denoted as Ti/TADDOL-CPP, as the catalyst for asymmetric addition of diethylzinc to aldehydes. Ti/TADDOL-CPP exhibited good catalytic performance (up to 96% yield and 94% ee) and could be recycled at least 11 times without obvious performance loss. Through the mechanistic investigation by ssNMR, they found that the building blocks, cooperative catalysis, local chiral environment, and hierarchical porous structure could impact the performance of the catalyst. At almost the same time, Cui and coworkers [401] also reported the construction of chiral TADDOL-based POPs for the same reaction, and also showed good performance.

In 2016, Cui and coworkers [174] achieved the construction of TADDOL COFs, namely, CCOF-1 and CCOF-2, from the condensation of enantiopure TADDOL-derived tetraaldehydes with flexible 4,4′-diaminodiphenylmethane. After the coordination with $Ti(O^iPr)_4$, both CCOF-1 and CCOF-2 showed impressive catalytic activity and enantioselectivity for catalyzing asymmetric addition of diethylzinc to aromatic aldehydes. Specially, CCOF-1 displayed comparable performance with their homogeneous analogue. CCOFs could be reused five times with a slight decrease in yield and enantioselectivity.

Asymmetric conjugation addition. In 2014, Cui and coworkers [402] introduced the chiral diene moiety, that is (1*R*,4*R*)-bicyclo[2.2.1]hepta-2,5-diene, to construct chiral POP catalysts. These chiral diene-based POPs could serve as good supports for Rh species. The Rh-coordinated POP, denoted as 1-Rh, was applied to catalyze the asymmetric conjugation addition of arylboronic acids to 2-cyclohexenone and showed moderate to good yield and enantioselectivity.

4.3.3 Transformation of alkenes and alkynes

Alkenes and alkynes are important and easily available raw materials in the petrochemical industry. Because of the rich reactivity of C–C multiple bonds, the transformation of alkenes and alkynes is highly anticipated to synthesize high-value-added chemicals. It is crucial to develop efficient catalytic systems to increase the activity and control the selectivity of the key transformation. However, to achieve these goals, the use of noble metals and the laborious synthesis of ligands are always unavoidable in homogeneous catalysis [403,404]. Covalently attaching these privileged catalysts to POPs is helpful to stabilize and recycle these expensive catalysts and reduce the expense of separation, which is extremely important for industrial applications. Besides, the tunable pore structure and high surface area of POPs would be beneficial for increasing the activity and controlling the selectivity of such important transformations. In the past decade, scholars in China did many important works in this research direction (Figure 29).

Alkene hydroformylation. The hydroformylation of olefins is one of the largest industrial processes for the synthesis of aldehydes and alcohols. Involving the addition of syngas (the mixture of CO and H_2) to olefins, alkene hydroformylation can be regarded as a 100% atom-economical process. In general, rhodium-based (Rh-based) catalysts are

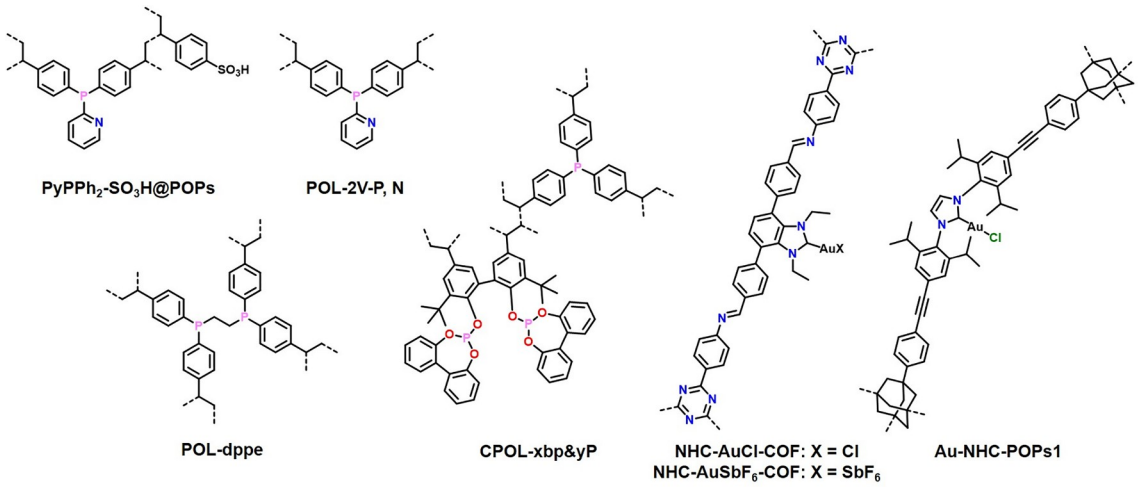

Figure 29 POP catalysts developed in China for the transformation of alkenes and alkynes (color online).

widely used in the laboratory because of their high activity and high catalytic selectivity; however, cobalt-based catalysts are more welcomed due to the low expense in industrial production even though the lower efficiency and higher energy consumption compared with Rh-based catalytic systems [405].

To overcome the limitation of Rh-based catalysts in homogeneous systems, Xiao, Ding, and their collaborators [277] developed a series of POPs as porous organic ligands (POLs) for producing stable and recyclable Rh-based heterogeneous catalysts. These POLs possessed hierarchical pore structure, high surface area, and pore volume; besides, heteroatoms, such as phosphorous, nitrogen, and oxygen, can be easily and precisely incorporated into POLs to serve as abundant coordinating sites. Importantly, the pore size, BET surface area, density of reactive sites, *etc*. of POLs can be finely tuned by the selection of monomers [406–408], and the change of monomer ratios [407]; such a modification plays a vital role to impact the catalytic performance.

Through introducing 1,2-bis(diphenylphosphino)ethane (dppe) into POLs, Xiao and coworkers [409] developed an efficient Rh-based catalytic system for the hydroformylation of olefins. The prepared Rh/POL-dppe catalyst exhibited high activity, high chemoselectivity (nearly quantitative aldehydes yield), and moderate regioselectivity (up to 93.5% on branched product for styrene, and 70% on linear product for 1-octene) on the hydroformylation of styrene and 1-octene. The Rh/POL-dppe catalyst can be recycled at least ten times without obvious performance loss. They verified that the excellent performance of Rh/POL-dppe over alkene hydroformylation should be attributed to the swelling property and high ligand concentration of POLs, which exemplified the advantages of POPs in key industrial processes.

Regioselectivity is a key issue to measure the performance of alkene hydroformylation. Ding and coworkers [406] introduced vinyl-functionalized biphephos ligand with high steric hindrance and tris(4-vinphenyl)phosphane for the synthesis of copolymer-based POLs (CPOLs). The ratio between biphephos ligand (bp) and trisphenylphosphane moiety (P) can greatly influence the porosity of as-prepared CPOLs, so as to impact the catalytic performance of Rh/CPOL-*x*bp&*y*P catalysts (*x* and *y* represent the mass (gram) of bp and P, respectively, used in the synthesis of CPOLs). They witnessed that the presence of biphephos ligand with high steric hindrance could help to improve the regioselectivity of the hydroformylation of various long-chain olefin; the ratio of linear aldehydes to branched aldehydes could reach 98:2. Interestingly, the internal olefins can be converted to corresponding linear aldehydes with high regioselectivity (up to 93%) after a tandem isomerizing hydroformylation process. It should be noted that they successfully conducted the hydroformylation of propene in the fix-bed reactor, which lays the foundation for industrial production [407]. When Rh/CPOL-1bp&10P was developed as the catalyst in propene hydroformylation, the TOF reached as high as 1,209.0 h^{-1}, the chemoselectivity to aldehydes was up to 93%, and the regioselectivity to linear aldehydes was up to 96%. The catalyst can maintain its outstanding performance for 1,000 h in the fix-bed reactor, which exhibited the robustness of the Rh/POLs catalytic system. It is a piece of influential news that the successful pilot scale production for the hydroformylation of propene was achieved by Ding and coworkers [410] in 2020, which is a great achievement and encouragement for the development of POPs in heterogeneous catalysis.

Alkyne hydration and carboxylation. *N*-heterocyclic carbene (NHC)-gold complexes are regarded as highly efficient catalysts to conduct alkynes transformation. Li and coworkers [411] prepared a series of Au-NHC-POPs from Au-NHC complex-based monomer for catalyzing alkyne hydration. The BET surface areas of these Au-NHC-POPs can

be tuned by changing the reaction conditions. Au-NHC-POPs1 with the highest BET surface areas (up to 798 $m^2 g^{-1}$) could afford a higher yield (up to 86%) of alkyne hydration at 120 °C. And the catalyst could be reused six times without significant activity loss. Lately, Dong and coworkers [412] achieved the direct construction of Au-coordinated NHC-based COF catalyst, namely, NHC-AuCl-COF, from NHC-AuCl-decorated monomer. After a simple anion exchange step, the Cl^- could be replaced by SbF_6^- to form a new catalyst named as NHC-AuSbF$_6$-COF. Both NHC-AuCl-COF and NHC-AuSbF$_6$-COF exhibited high crystallinity, good BET surface area, and narrow pore size distribution. Besides, the Au loading of NHC-AuCl-COF and NHC-AuSbF$_6$-COF could be maintained at a high level (23.40 wt% and 18.99 wt%,respectively). NHC-AuSbF$_6$-COF was used to carry out alkyne hydration. NHC-AuSbF$_6$-COF gave a high yield (up to 99%) of alkyne hydration at 90 °C.

Dong *et al*. [412] also used NHC-AuCl-COF to catalyze the carboxylation of phenylacetylene with CO_2, which is an important protocol to produce 3-phenylpropiolic acid *via* the co-conversion of alkynes and CO_2. NHC-AuCl-COF gave a high yield in the carboxylation of phenylacetylene (up to 99% yield) under mild conditions and can be recycled five times without activity loss.

Ding's group [413] developed a series of Pd@POLs catalytic systems for catalyzing the alkoxycarbonylation of alkynes. By incorporating diphenyl-2-pyridylphosphine moiety as the coordinating sites, the prepared POL-2V-P,N can support $Pd(OAc)_2$ to conduct the transformation from methyl acrylate from acetylene, CO, and methanol to methyl acrylate. They also prepared the SO_3H-decorated POL-2V-P,N, that is Pd-PyPPh$_2$-SO$_3$H@POPs, for organizing the Pd centers and acidic sites in the pore structure of POPs [414]. Pd-PyPPh$_2$-SO$_3$H@POPs exhibited a higher activity (TON>1,000) than its homogeneous analogue (TON<50) in catalyzing the methoxycarbonylation of phenylacetylene and acetylene.

4.3.4 CO_2 fixation

CO_2 emission is an important environmental issue. CO_2 is also a type of sustainable, nontoxic, abundant, and inexpensive carbon source. Using CO_2 as a C_1 building block to achieve the synthesis of high-value-added chemicals is extremely significant to reduce the greenhouse effect and achieve carbon neutralization. Featured with abundant porosity, good chemical stability, and structural tenability, POPs have attracted extensive interest in the chemical fixation of CO_2 (Figure 30).

Cycloaddition of epoxides with CO_2. Xiao and coworkers [415] constructed a series of metalloporphyrin-incorporated POPs for the cycloaddition of epoxides with CO_2 to afford cyclic carbonates. They found that cobalt-coordinated porphyrin-based POP, that is Co/POP-TPP, displayed high catalytic activity (up to 96% conversion) and selectivity (up to 99% selectivity) under 1 atm CO_2 and 29 °C, which is higher than that of its homogeneous analogue. Even under a low concentration of CO_2 (15%), Co/POP-TPP also showed high activity (45% conversion) and high selectivity (89%). Co/POP-TPP also exhibited high stability and can be recycled 18 times without obvious activity loss.

Ding and coworkers [416] integrated the multiple reactive sites, that is ionic liquids, zinc halides, and PPh_3, into POPs. The obtained catalysts, denoted as PPh_3-ILBr-$ZnBr_2$@POPs,

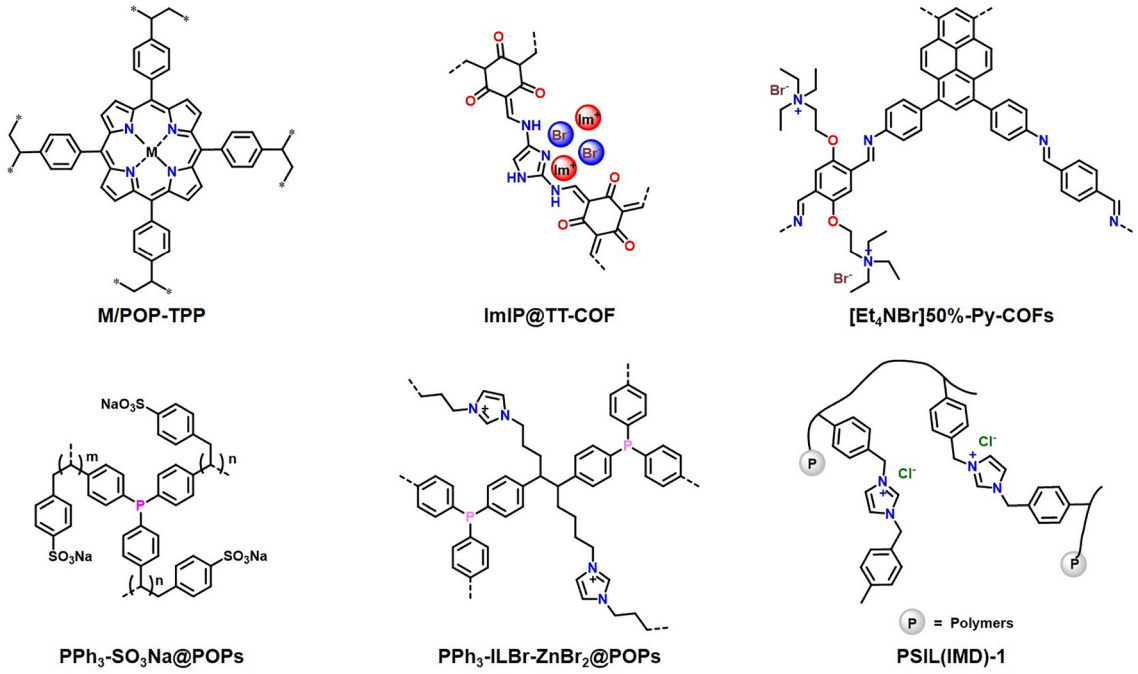

Figure 30 POP catalysts developed in China for CO_2 fixation (color online).

showed remarkable catalytic activity in conducting the cycloaddition of propylene oxide with CO_2. The TOF of PPh_3-ILBr-$ZnBr_2$@POPs could reach as high as 5,200 h^{-1} at 160 °C, and the TON of the catalyst could reach 2,120 and 720 at 40 and 25 °C, respectively. The excellent activity of PPh_3-ILBr-$ZnBr_2$@POPs should be attributed to the synergistic effect of multiple catalytic sites in POPs. Recently, they constructed a series of ionic liquids-based cross-linked polymers [417]. The PSIL(IMD)-1 shows high catalytic efficiency (up to 99.9% yield of propylene carbonate) in the cycloaddition of CO_2 (2 MPa) with propylene oxide at 130 °C. More importantly, PSIL(IMD)-1 exhibited stable performance in a continuous-flow fixed-bed reactor for 130 h.

Recently, Wang and coworkers [418] synthesized ImIP@TT-COF, which integrated nitrogen-rich covalent organic framework (TT-COF) and imidazolid-based ionic polymer (ImIP). The synergistic reactive sites make its catalytic activity significantly better than that of ImIP, TT-COF, and its physical mixtures when conducting the cycloaddition of epoxides with CO_2. Notably, ImIP@TT-COF can catalyze the cycloaddition of electron-deficient 2-(chloromethyl)oxirane with CO_2 to afford the corresponding product in a quantitative yield at 110 °C and 1.0 MPa CO_2 pressure for 1h.

N-Formylation. Gao and coworkers [419] covalently linked (2-bromoethyl)triethylammonium bromide ionic liquid (Et_4NBr) to the hydroxyl groups-modified $[HO]_{x\%}$-Py-COFs *via* post-synthetic strategy. The as-obtained $[Et_4NBr]_{50\%}$-Py-COF exhibited excellent activity in catalyzing *N*-formylation between CO_2 (1 bar) and *N*-methylanilines. The reaction gave a high yield (up to 94%) under the condition of 30 °C, 1 bar CO_2 for 48 h when phenylsilane was the reductant. These COFs could be recycled four times.

Ding and coworkers [420] synthesized a bifunctional Ru-PPh_3-SO_3Na@POP catalyst, which immobilizes metals and bases simultaneously, for catalyzing the *N*-formylation reaction of amine, H_2, and CO_2. Without the addition of alkali, Ru-PPh_3-SO_3Na@POP showed high activity to afford *N*-formylated products with high yields (up to 92%) at 100 °C, p_{CO_2}=p_{H_2}=3 MPa. The catalyst could be reused at least five times without the obvious decrease in catalytic performance.

4.4 Photocatalytic CO_2 reduction

The CO_2 photoreduction reaction (CO_2PRR) converts CO_2 with the use of ecologically beneficial solar energy. Under moderate and pollution-free environments, this reaction can produce high-value-added chemicals (C1 to C4) catalyzed by sunlight. Despite the fact that this field has a wide range of applications, existing photocatalysts have low CO_2 adsorption, conversion efficiency, and selectivity, as well as fast electron-hole recombination and a poor active site structure, which has become the most significant barrier to carbon resource conversion [421]. As CO_2 could be converted to carbon monoxide (CO), methanol (CH_3OH), formic acid (HCOOH), methane (CH_4), and even higher-order hydrocarbons, one of the major issues in photocatalytic CO_2 reduction is the CO_2 adsorption capacity and selectivity of the reduction products [422]. As a result, developing photocatalysts with high activity and selectivity is critical for achieving high CO_2PRR performance. For most photocatalytic CO_2 reduction systems, a light-harvesting reagent transforms visible light into chemical energy by creating electron-hole pairs, which drive the redox process [423]. In photocatalytic CO_2 conversion, semiconductors are widely employed materials. Nevertheless, their performance is limited by a combination of photogenerated electrons and holes, a poor CO_2 uptake capacity, and a poor specific surface area [424]. POPs have a broader visible light absorption range, a larger specific surface area, and tunable valence band (VB) and conduction band (CB) locations than inorganic semiconductor materials. While converting CO_2 into high-value-added compounds, these properties allow POPs to own high efficiency, selectivity, and durability. The catalytic effectiveness of CO_2PRR is determined by the CO_2 adsorption capacity, light absorption range, and charge separation efficiency of POPs in these procedures [425,426]. POPs with metals, metal-free POPs, and POPs combined with inorganic semiconductors are all promising candidates for CO_2 photocatalytic reaction.

4.4.1 Metal-free POPs for CO_2 photoreduction

POPs that do not include metals are more in keeping with the notion of green chemistry. They are more cost-effective and successfully prevent metal deactivation, giving them a competitive advantage in the industry. By the condensation of hexachlorocyclotriphosphazene with barbituric acid, Guo and coworkers [427] developed porous polymers enriched with N, O, and P (named NOP-COP). NOP-COP has superior photocatalytic CO_2 reduction capability, and NOP-COP can selectively convert CO_2 to CH_4 with an output of 22.5 mol g^{-1} h^{-1} and selectivity of over 90%, according to the studies. By introducing carbon vacancies into the material and employing the carboxyl intermediates created by CO_2 to maintain carbon vacancy, Yang and coworkers optimized the reaction kinetics [428]. The CO_2PRR efficiency of the polymer has been considerably enhanced compared to the original polymer without carbon vacancy, which is 45 times greater. Eosin Y functional POPs, that could adsorb and activate CO_2 and H_2O molecules, were designed by Yu and coworkers [429]. CO_2 could well be transformed into the single carbonaceous molecule CO with an efficiency of 33 μmol g^{-1} h^{-1} and a selectivity of 92% without the use of a sacrificial reagent. In typically, photocatalytic CO_2 reduction operations must be performed in a solvent. Chen and cow-

orkers [430] constructed an ionic liquid [P4444][p-2-O] as a catalyst for CO_2 reduction, and ionic liquids typically have high CO_2 and H_2O adsorption properties. The material exhibits good selectivity and CO production under the simultaneous action of an ionic liquid and a porous conjugated framework. COFs' crystalline structure efficiently avoids electron-hole recombination and charge quenching at defects, and their light absorption ability is superior to amorphous POPs. Wang and coworkers [431] incorporated bromine into COF to increase the electron delocalization of the framework, and the resulting material TAPBB-COF was able to selectively convert CO_2 to CO with an output of 295.2 μmol g^{-1} and a selectivity of 95.6% in just 12 h. Owing to the high quantity of nitrogen sites, suitable band structure, and broadly visible light capture region, Lei and coworkers [432] built donor-acceptor imine-based CT-COF, which demonstrated good CO_2PRR activity with visible light irradiation. To summarize, the major product of metal-free POPs as a CO_2PRR catalyst is CO, and metal-free POPs have improved catalytic selectivity and durability, providing them with a favorable application possibility. Their catalytic efficiency, nevertheless, is still poorer than metal-based POPs. It is still a difficult task to increase their catalytic performance.

4.4.2 Metal-loaded POPs for CO_2 photoreduction

It is simpler to capture CO_2 and produce intermediates in the active sites when noble metals (Rhenium (Re), Iridium (Ir), and others) with an empty d band are incorporated into POPs. Employing the ionic thermal synthesis approach, Xu and coworkers [433] constructed a porous structure using 2,6-dicyphenylpyridine as the building block and anchored the Re-carbonyl compound $Re(CO)_3Cl$ on it to construct the N-rich composite system Re-CTF-py. The observations reveal that the constructed Re-CTF-py converts CO_2 to CO with exceptional performance, with the system's CO_2 to CO photoreduction approaching 353.05 μmol g^{-1} h^{-1} after 10 h. Orchanian and coworkers [434] determined that the amount of Re active sites impacts CO_2PRR catalytic activity and that the amount of Re active sites has an ideal level which drives the TON of CO to achieve 70 in 5 h. Liang and coworkers [54] generated the relevant POPs from bipyridine and phenanthroline, respectively, and then treated them with Re $(CO)_5Cl$ to establish metal complexes, yielding the CPOP-30-Re and CPOP-31-Re, respectively. The bipyridine-based CPOP-30-Re possessed better photocatalytic conversion capability than the phenanthroline-based CPOP-31-Re, according to the studies. The reduction rate of CO_2 into CO with CPP-30-Re under visible light irradiation was as high as 623 μmol g^{-1} h^{-1}, with a selectivity of 97.8%. The finely ordered crystallized COFs exhibit a regular structure and π-π stacked structure, and their ordered pore structure considerably enhances active site usage as well as charge separation and transfer efficiency. Yang and coworkers [426] investigated the connection between charge separation efficiency and CO_2PRR catalytic activity. They developed an Re-carbonyl compound with an imine-linked COF (Figure 31). The experimental and simulated results demonstrate that in the CO_2PRR step, there exist three important intermediates that determine charge separation, induction period, and the rate-limiting phase in the catalytic reaction. Fu and coworkers [435] designed Bpy-sp^2c-COF, which is a completely conjugated COF connected by –HC=CH–. In the catalytic process, Bpy-sp^2c-COF possesses strong chemical stability, and charge separation and transfer rate are improved. The photocatalytic reduction activity of CO_2 is improved much more by the metal active centre in the skeleton, with CO yield and selectivity reaching 1,040 μmol g^{-1} h^{-1} and 81%, respectively. The CO production was elevated to 1,400 μmol g^{-1} h^{-1} when dye components were integrated as photosensitizers into the framework of the COF, and the selectivity was enhanced to 86%. Tan and coworkers [436] employed porphyrin-based CTF as the substrate, then added Fe_2O_3 nanoparticles and $Ru(bpy)_3Cl_2$ as the photosensitizer *in situ* to generate a ternary organo-inorganic combination system that serves as an electron transfer relay. With a performance of 8.0 μmol g^{-1} h^{-1} and a selectivity of 93%, the ternary-element complex is advantageous in preventing the reverse electron transfer process and speeding up the forward

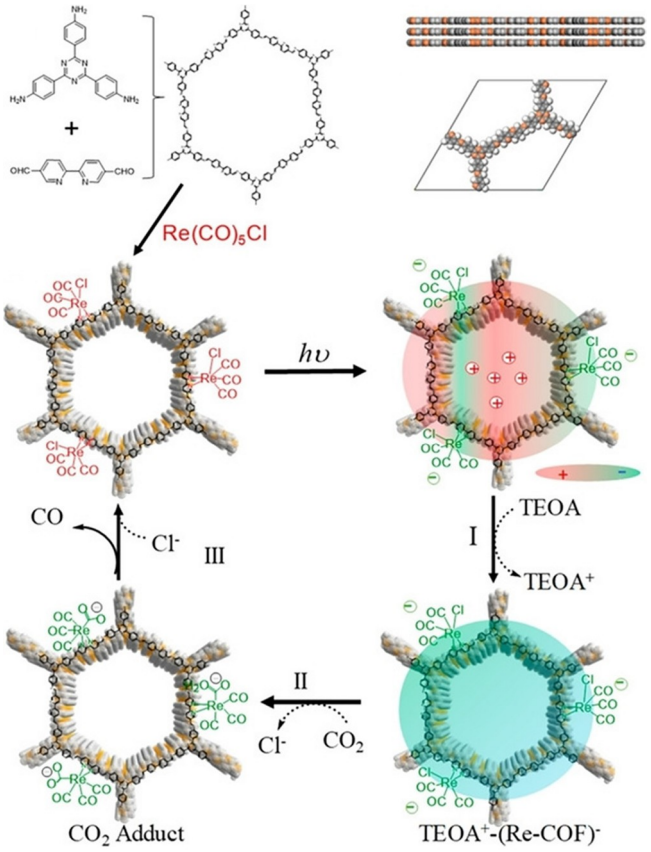

Figure 31 The synthesis route to Re-COF and proposed catalytic mechanism for the CO_2 reduction reaction [435] (color online).

electron transfer rate, considerably enhancing the photocatalytic efficiency of CO_2 conversion to CO. By covalently coupling C_{60} with pyrene, Yadav and coworkers [437] synthesized a polymer film as the photocatalyst. CO_2 was preferentially converted to formic acid (HCOOH) when the polymer film was coupled with Rh complex and nicotinamide adenine dinucleotide (NADH) with visible light (239.46 μmol). Wisser and coworkers [438] developed Cp*Rh@PerBpyCMP by conjugating a conjugated microporous polymer built on pyrene and bipyridine with the rhodium compound. Electrons migrate from the highest occupied molecular orbital (HOMO) in pyrene to the lowest unoccupied molecular orbital (LUMO) in the photosensitizer Ru and then to the Rh active site when exposed to light.

Furthermore, the incorporation of inexpensive and plentiful non-noble metals including cobalt (Co) and nickel (Ni) into porous organic polymer-carriers possesses greater practical application potential. For the development of CO_2 PRR, Yang and coworkers [439] developed three triazine-based CMPs doped with cobalt active units. The electron-donating and electron-withdrawing compounds of the framework were modified to change the band gap and redox potential. The polymer containing the D-A structure had the highest CO_2PRR activity among the three catalysts, with a CO_2 photoreduction efficiency of 1,210 μmol g^{-1} h^{-1} and a selectivity of 81.6%. The D-A structure impacts the photogenerated electron transfer capacity as well as the optical band gap of the material. POPs with a minor quantity of $[Ru(bpy)_3]^{2+}$ are nevertheless referred to as POPs containing non-noble metals. The incorporation of the sensitizer $[Ru(bpy)_3]^{2+}$ can broaden the light absorption range and enhance charge separation, boosting photocatalytic CO_2 reduction efficiency. To improve the interlayer gap, Liu *et al*. utilized significant quantities of 2,4,6-trimethylbenzaldehyde and loaded porphyrin COF nanosheets with cobalt compound and sensitizer $[Ru(bpy)_3]^{2+}$ [440]. Upon light irradiation, the polymer has a remarkable conversion efficiency of 10,162 μmol g^{-1} h^{-1} and a selectivity of 78% for converting CO_2 to CO. The kind of cobalt complex may be adjusted to control the CO_2PRR product type. Sarkar and coworkers [441] employed $Co(dmg)_2$ as a co-catalyst to react with the ketamine COF framework and reduce CO_2 to HCOOH in the presence of visible light. Tan and coworkers [208] reported one kind of crystalline CTF with bipyridine sites prepared *via* the controlling feed rate strategy for photocatalytic CO_2 reduction. This system could achieve a high CO production of 120 μmol and CO/H_2 selectivity of 83.8% over 10 h irradiation using $[Ru(Bpy)_3]Cl_2$ as a visible-light photosensitizer and triethanolamine as an electron donor in acetonitrile/aqueous solution under visible light. Nickel (Ni) complexes have also been demonstrated to possess strong catalytic activity, making the separation of photogenerated electron-hole pairs in porous frameworks much easier. In the bipyridine group of a porous polymer structure, Zhong and coworkers [442] inserted a single nickel site. CO_2PRR has high catalytic activity in pure CO_2 or diluted CO_2 environments, with a production of 4,057 μmol g^{-1} throughout 5 h and a selectivity of 96% for CO_2 conversion to CO.

4.4.3 POPs combined with inorganic semiconductors for CO_2 photoreduction

Many inorganic semiconductors have been developed as CO_2PRR photocatalysts. However, the combination of photogenerated electrons and holes hinders their effectiveness in CO_2PRR, and they can only absorb ultraviolet light. As a result, the coupling of an inorganic semiconductor with a porous organic polymer has garnered a lot of interest. This strategy integrates POPs' outstanding light absorption capacity, pore structures for transmitting electrons, and uniform dispersion of active centers with inorganic semiconductors' catalytic performance. Dai and coworkers [443] synthesized Bi_2WO_6 hollow microspheres and coated them with conductive polymers (polyaniline, polypyrrole, *etc*.) for photocatalytic CO_2 reduction underneath visible light as Bi_2WO_6 have excellent photocatalytic water splitting capability under visible light. The photocatalytic efficiency of the produced composite is remarkable, and it can transform CO_2 into methanol and ethanol. Sato and coworkers [444] developed a dual photocatalyst by integrating a p-type semiconductor with a Ru-based polymer and TiO_2 nanoparticles, as well as an electron transport mechanism. The experiments reveal that the compound can selectively reduce CO_2 to $HCOO^-$ with a selectivity of more than 70% employing this material as a catalyst for CO_2PRR and water as an electron donor and proton supplier. HCP-TiO_2-FG ternary hybrid materials (Figure 32) were also generated by Tan *et al*. [445]. To graft the benzene ring, TiO_2 is first attached to graphene to create TiO_2-G, and then the surface functionalization of graphene is performed. Finally, the benzene ring and aromatic compounds containing triphenylbenzene are hypercrosslinked to form a porous network layer. The CO_2 adsorption ability, light capture range, and charge separation efficiency are all boosted by employing the ternary system. With light irradiation, the obtained photocatalyst HCP-TiO_2-FG of CO_2PRR exhibited a high BET specific surface area (988 m^2 g^{-1}) and CO_2 adsorption capacity (12.87 wt%), allowing for the reduction of CO_2 to CH_4 and CO without the need of additional sacrificial agent or co-catalyst. The production of CH_4 in particular could approach 27.62 μmol g^{-1} h^{-1}. Recently, Tan and coworkers [446] developed a strategy for directly grafting hypercrosslinked polymers (HCPs) on the TiO_2 surface to construct Pd-HCPs-TiO_2 composite for efficient photocatalytic reduction of CO_2. Benefited from the enhanced charge transfer of photogenerated electrons and improved CO_2 adsorption dedicated by HCPs, the well-designed composite with surface area of 373 m^2 g^{-1} exhibits

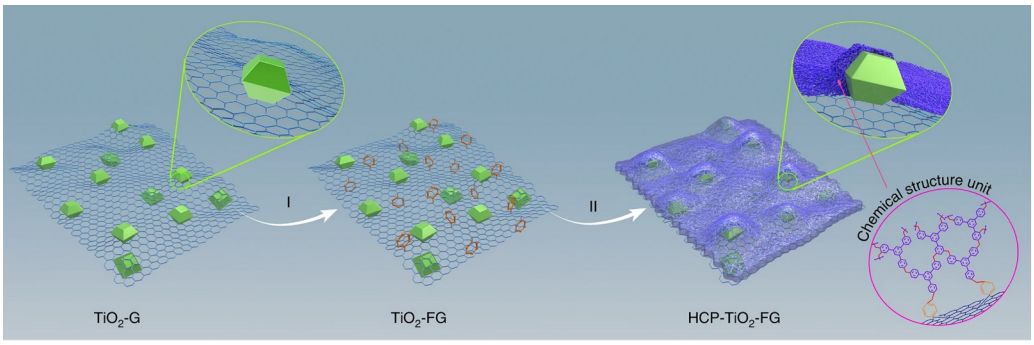

Figure 32 Construction of a well-defined porous HCP-TiO_2-FG composite structure [445] (color online).

high CO_2 photoreduction efficiency with a CH_4 evolution rate of 237.4 μmol g^{-1} h^{-1} and selectivity of more than 99.9%. Wang and coworkers [447] reported a composite photocatalyst Pd-HPP-TiO_2 prepared by hyper-crosslinking porphyrin-based polymers on hollow TiO_2 surfaces and subsequently coordinating with Pd(II). Pd-HPP-TiO_2 shows photocatalytic activity even in air with a CO_2 conversion yield of 12% and the CH_4 production of 24.3 μmol g^{-1} after 2 h UV-visible light irradiation. Guo and coworkers [448] created SnS_2/S-CTFs by designing a CTF with a unique structure (a sulfur bridge) and integrating it with SnS_2. The separation of electron-hole pairs was efficiently facilitated by SnS_2/S-CTFs, and the reduction rate of CO_2 and CH_4 with visible light was 123.6 μmol g^{-1} h^{-1} and 43.4 μmol g^{-1} h^{-1}, respectively. In summary, despite the fact that there are few studies on POPs combined with inorganic semiconductors for CO_2PRR, fairly high catalytic efficiency has been attained so far. However, combining the fantastic performance of POPs and semiconductors in a synthetic material, as well as controlling the thickness of each component to avoid the active center from becoming embedded, remain significant hurdles.

4.5 Electrochemistry and photocatalysis

Electrochemistry applications. As mentioned above, olefin-based COFs have shown good electrical properties and have been successfully applied in the fields such as electrocatalysis, capacitors, and cells. For example, the first example of olefin-linked COF, 2DPPV exhibits typical semiconducting properties and excellent thermal stability, as verified by being facilely converted into sharp-persistent porous carbon nanosheets with high specific surface areas of up to 880 m^2 g^{-1}, releasing an excellent electrochemical performance as supercapacitor electrodes and electrocatalysts for the oxygen reduction reaction. This result preliminarily manifested the reversible behaviors of the C=C double bond in the formation of long-range order structures, providing a bottom-up synthetic strategy toward porous materials and graphene analogues (Figure 33a, b) [30].

Later, Zhang's group [153] developed a highly-symmetric vinylene-linked COF with octupolar-conjugated characters g-$C_{54}N_6$-COF and a less-symmetric g-$C_{52}N_6$-COF. They found such a non-centrosymmetric polar structure in the case of octupolar COF endowed it with more promising semiconducting behavior as compared with the less-symmetric COF, for instance, the enhanced light-harvesting and excellent photo-induced charge generation and separation. Along with the matched energy level, this octupolar COF enabled the two-half reactions of photo-catalytic water splitting with an average O_2 evolution rate of 51.0 μmol h^{-1} g^{-1} and H_2 evolution rate of 2,518.9 μmol h^{-1} g^{-1}, overwhelmingly better than those of the less-symmetric one. Theoretical calculation rationally demonstrated the significant influence of the topological structure on the polarity of such π-extended 2D structures, as well as their electrical characteristics. Jiang and coworkers [155] also synthesized the unsubstituted vinylene-linked COF TM-TPT-COF for ORR application. By the incorporation of Pt nanoparticles on the COF skeleton, the as-synthesized Pt@COF exhibited high ORR activity in an acid electrolyte with an onset potential of 1.05 V *versus* reversible hydrogen electrode and a half-wave potential of 0.89 V, which are more positive than those of commercial Pt/C and other reported catalysts.

For supercapacitors, Zhang and coworkers [152] constructed a vinylene-linked g-$C_{34}N_6$-COF with a high crystalline honeycomb-like structure and a specific surface area of 1,003 m^2 g^{-1}. The SEM and TEM images revealed its nanofibrous morphology with relatively uniform diameters of around 100 nm, allowing for being easily composited with carbon nanotubes to form the free-standing COF/CNT hybrid thin film with excellent mechanical properties. Moreover, such a composite could be smoothly fabricated into the interdigital electrode for microsupercapacitors (MSCs). As the first example of COF-based MSC, the as-manipulated device offered an aerial capacitance of 15.2 mF cm^{-2}, an energy density of 7.3 mW h cm^{-3}, and remarkable rate capability (Figure 33c).

Similarly, two vinylene-linked 2D COFs g-$C_{30}N_6$-COF and g-$C_{48}N_6$-COF were also prepared for MSCs. The re-

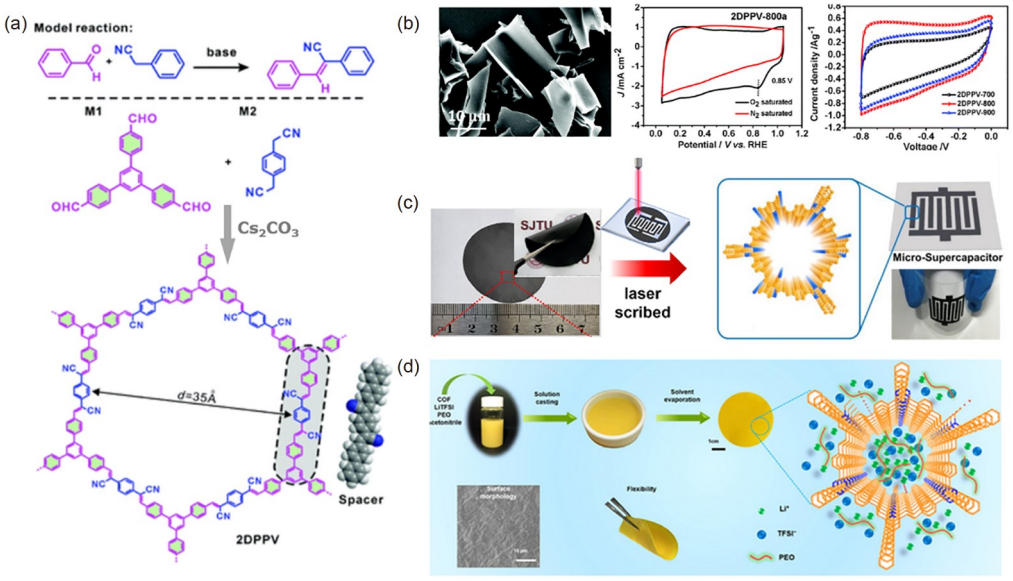

Figure 33 (a) Synthetic scheme of 2DPPV. (b) Electrochemical properties of 2DPPV [30]. (c) Microsupercapacitors based on the 3,5-dicyano-2,4,6-trimethylpyridine-derived COFs [152]. (d) Solid electrolyte film based on the ionic vinylene-linked COFs [157] (color online).

sulting COFs exhibit highly crystalline honeycomb-like structures stacked from hexagonal-latticed polymeric layers and display well-defined nano fibrillar morphologies with uniform diameters of ca. 80 nm and ultra-lengths up to several micrometers as revealed by their high resolution transmission electron microscope (HRTEM) images. By compositing it with carbon nanotubes under simple ultrasonication, the flexible thin films with varying thicknesses formed, which are facile to be processed to interdigital microelectrodes upon laser scribing. Such electrodes were fabricated to COF-based MSCs, releasing high areal capacitances of up to 41.4 mF cm^{-2}, a high volumetric energy density of up to 38.5 mWh cm^{-3} among the highest values for state-of-the-art MSCs, indicative of excellent compatibility of vinylene-linked COFs with nanocarbons. Although the exact mechanism for the formation of such COF nano fibrillar morphologies is still not clear, such unique characters make triazined-containing COFs suitable for the composition with CNTs, and being further fabricated to thin-film devices with outstanding flexibility and integration capability, holding an exceptional perspective in the development of high-performance portable and wearable electronic systems [151].

COFs could also be applied to cells. Recently, Zhang and co-workers [156] reported highly crystalline vinylene-linked COFs (denoted as NKCOF-10). The applicability of NKCOF-10 for proton conductive membranes was explored. They anchored the proton carriers, H_3PO_4, in the pores of NKCOF-10 through pyrazine functionalities and synthesized the composite material, H_3PO_4@NKCOF-10. It exhibited both ultrahigh proton conductivity (9.04×10^{-2} S cm^{-1}) and ultralow activation energy (0.06 eV). Ultimately, they fabricated a practical proton exchange membrane fuel cell utilizing H_3PO_4@NKCOF-10 as the solid electrolyte. The maximum power and current density thereof reached up to 135 mW cm^{-2} and 676 mA cm^{-2}, respectively, which was the best record for COF materials.

The incorporation of multiple functions into a COF network represents a highly efficient strategy for the integrated and extended applications of COF materials. For this purpose, to search a key monomer with dual or more roles in activating reaction and establishing some functions that are extremely desired for the development of a COF with promising properties, pyridinium-based monomers stand out among the desirable groups. In this regard, Zhang and coworkers [157] developed the first example of ionic vinylene-linked 2D COFs. The resulting COFs exhibited honeycomb-like 2D structures with quite large surface areas (up to 1,343 m^{-2} g^{-1}) and regular open channels (diameters centered at 1.4 and 1.9 nm). The regularly shape-persistent nanochannels and positively charged polymeric frameworks make such kinds of COFs available for many applications. Actually, the excellent compatibility of these ionic vinylene-linked COFs with organic/polymeric components and inorganic salts inspired that they can be uniformly incorporated with PEO and lithium salt to enhance ionic conductivity, which can be promisingly used in lithium-ion batteries. Upon a simple solution-casting fabrication, high-quality and flexible free-stand composite films were fabricated. Their promising electrical behaviors were preliminarily revealed, exhibiting good ion conductivities of up to 2.72×10^{-3} S cm^{-1} at 100 °C with 10 wt% of COF content (Figure 33d).

Photocatalysis applications. Olefin-based COF materials with organic semiconductor properties have also been successfully applied in photocatalysis and photoelec-

trochemistry. In 2019, Wang *et al*. [31] designed the Por-sp2c-COF. The ordered porous framework of Por-sp2c-COF was demonstrated by PXRD and HRTEM. The BET surface area of it reached 689 m^2/g. Besides, Por-sp2c-COF well retained its crystallinity under harsh acidic or basic conditions, as demonstrated by the PXRD spectrum, exhibiting its high chemical stability. This material was effectively used as a heterogeneous photocatalyst for the aerobic oxidation of amines to imines. For the transformation reaction of benzylamine to *N*-benzylidenebenzylamine, Por-sp2c-COF showed excellent photocatalytic activity, with a transformation rate reaching over 99%, which is even comparable to some metal-containing heterogeneous photocatalysts. However, the analogous imine-linked Por-COF showed no photocatalytic activity due to the reaction between the imine-linkages with benzylamine, which leads to the collapse of the ordered framework under the reaction substrate. To better illustrate the superior photocatalytic reactivity of Por-sp2c-COF, it was utilized for another reaction, the transformation of dibenzylamine to *N*-benzylidenebenzylamine. It also exhibited good photocatalytic performance with an ultrahigh conversion rate of over 97%, while the imine-linked Por-COF only facilitated a much lower conversion rate of 44%. Since the imine linkages are stable under the substrate of this reaction, the exceedingly better performance of Por-sp2c-COF is rationally assigned to its fully conjugated skeleton, which renders a more efficient pathway for electron transfer (Figure 34a).

In another case, Zhao and coworkers [120] synthesized a vinylene-linked TP-COF. Noteworthily, the electron-withdrawing triazine units in TFPT can effectively tune the electronic structure of the 2D COF while the incorporation of the olefin (–C=C–) linkage as the sp^2-carbon bridges provides conjugation with enhanced electron delocalization. The combination of these two motifs led to the excellent semiconducting property of TP-COF, which bears an LUMO of −3.23 eV and a band gap of 2.36 eV. TP-COF was then applied in artificial photosystem I for coenzyme-assisted photosynthesis and showed excellent photocatalytic activity. Finally, unprecedented coenzyme regeneration efficiency and a record-high coenzyme-assisted L-glutamic synthesis yield of 97% in 12 min were obtained with the TP-COF PSI (Figure 34b).

Zhang's group [148] has also paid great effort to the investigation of photo-responsive COFs. Three pyridine-cored COFs with unsubstituted vinylene linkages were achieved. Meanwhile, the appropriate band energy levels could be finely tuned by changing the aldehyde building blocks for matching the water-splitting driving force. Such kinds of unsubstituted vinylene-linked COFs also show remarkable photocatalytic activities and enable driving two half-reac-

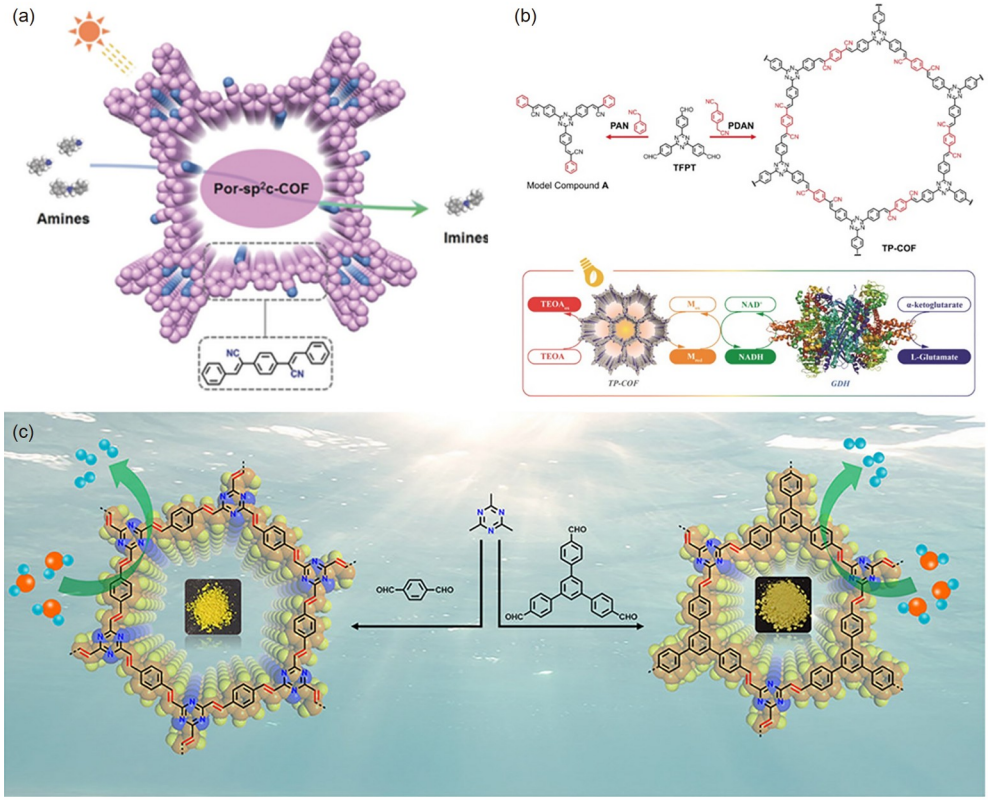

Figure 34 (a) The symbolic pattern was indicative of the photocatalytic activity of Por-sp2c-COF [31]. (b) The synthesis of TP-COF and its photocatalytic activity for boosting the coenzyme-assisted synthesis of L-glutamate of TP-COF [120]. (c) Photo-electrochemical activities of the unsubstituted vinylene-linked COFs arising from 2,4,6-trimethyl-1,3,5-triazine monomer [150] (color online).

tions of water splitting separately under visible light irradiation, comparable to graphitic carbon nitride (g-C_3N_4) derivative. They also developed COF-p-3ph, COF-p-2ph and COF-m-3ph which showed high crystallinity with AA stacking mode of honeycomb-like 2D sheets and high porosity with surface areas of up to 1,231 m^2/g, as indicated by PXRD and BET analyses. UV-vis spectroscopic studies revealed that the conduction band minimum (E_{CB}) of the as-prepared three COFs is higher than the potential of $O_2/O_2^{\bullet-}$ (−4.16 eV), which allows for the molecular oxygen to a superoxide radical anion under photo-induced conditions. Therefore, these COFs were applied to the photocatalytic transformation of a wide series of arylboronic acids to corresponding phenols in high efficiency and excellent recyclability [149]. In 2019, they reported g-$C_{18}N_3$-COF and g-$C_{33}N_3$-COF. Owing to the excellent semiconducting properties of these materials and the highly conjugated skeletons which endow themselves with good performance in electron transfer, they were utilized for photoelectrodes and exhibited remarkable photocurrents and rapid charge transfer rates (Figure 34c) [150].

4.6 Biomedical application

As a special family of water-soluble porous organic polymers, 3D SOFs feature efficient adsorption of drugs and biomacromolecules in aqueous media. Moreover, this adsorption takes place in an *in-situ* manner and the drugs or biomacromolecules can be maintained in the interior of the frameworks for hours to days. All the 3D SOFs have hydrodynamic diameters ranging from 30 nm to ≥200 nm, which depend on the concentrations. Although the frameworks are generated at high concentrations, their dilution-caused de-assembly is quite slow due to the unique encapsulation mechanism of CB[8] for various aromatic dimers, the decomposition of which needs to overcome a high energy barrier. It has been established that the nano-scaled size of 3D SOFs enables this kind of 3D supramolecular architecture with good ability as transmembrane carriers for drug and biomacromolecules. Thus, 3D diamondoid supramolecular organic frameworks d-SOF-11, d-SOF-12a–e, and d-SOF-16 prepared from the compounds 11, 12a–12e, or 16 and CB[8] have been found to realize intracellular delivery of anti-tumor therapeutic agent pemetrexed and doxorubicin and short DNA [238,239]. *In vivo* experiments showed that the delivery of SOF-11 and d-SOF-12a–e for pemetrexed and doxorubicin could considerably improve their efficacy.

5 Summary and outlooks

As described above, POPs always possess low densities, large surface area, permanent pore structures, tunable porosities, good chemical stabilities, and rich designability. Through the composition and structure design, functional POPs have shown superior performance and the great application potential in many fields. In this review, we have discussed the recent progress of POP materials in China, including the design and preparation of POP materials and film, and the application of functional POPs for adsorption, separation, catalysis, and electrochemistry. Despite the great effort and contribution to the synthesis of POPs with excellent properties, to further promote the development of POP materials remains worthwhile.

Although there are already many kinds of POP materials, it is still very important to further develop new POP materials with different types and functions to meet different application requirements. For example, introducing new chemical reactions to construct POPs with new covalent bonds; designing COFs with new topological structures; or exploring new functional molecular building blocks.

There are also some challenges to the characterization of POPs, and especially the understanding of the synthesis process deserves great attention. For example, appropriate imaging techniques and structural models should be developed to more accurately describe the structure of amorphous POPs. For crystalline POPs, such as COF, CTF, and SOF, the synthesis involves the establishment of chemical bonds and crystallization. It is valuable to develop new imaging technology to understand this complicated process.

Moreover, the large-scale synthesis of POPs is an important step toward the practical application of POPs. Most POP materials are synthesized in solvothermal conditions. The development of a green, scalable, industrial-compatible synthesis method is very attractive. By taking advantage of the designability and the porous properties of POPs, the large-scale practical application in the fields of gas phase and liquid phase adsorption and separation, chemical catalysis, photocatalysis, as well as electrocatalysis and energy storage of POPs is very promising.

Conflict of interest The authors declare no conflict of interest.

1 Yang XY, Chen LH, Li Y, Rooke JC, Sanchez C, Su BL. *Chem Soc Rev*, 2017, 46: 481–558
2 Das S, Heasman P, Ben T, Qiu S. *Chem Rev*, 2017, 117: 1515–1563
3 Shi R, Han X, Xu J, Bu X. *Small*, 2021, 17: 2006416
4 Zheng H, Gao F, Valtchev V. *J Mater Chem A*, 2016, 4: 16756–16770
5 Lan Y, Wang XHY, Zhen Zhao. *Acta Phys Chim Sin*, 2017, 33: 2359–2376
6 Boissiere C, Grosso D, Chaumonnot A, Nicole L, Sanchez C. *Adv Mater*, 2011, 23: 599–623
7 Lee JSM, Cooper AI. *Chem Rev*, 2020, 120: 2171–2214
8 Xu Y, Jin S, Xu H, Nagai A, Jiang D. *Chem Soc Rev*, 2013, 42: 8012–8031
9 Ji W, Wang TX, Ding X, Lei S, Han BH. *Coord Chem Rev*, 2021, 439: 213875

10 Díaz U, Corma A. *Coord Chem Rev*, 2016, 311: 85–124
11 Ben T, Qiu S. *CrystEngComm*, 2013, 15: 17–26
12 Yang B, Wang H, Zhang D, Li Z. *Chin J Chem*, 2020, 38: 970–980
13 Li ZT, Wang H, Zhang DW. *Chem J Chin Univ*, 2020, 41: 1139–1150
14 Davankov VA, Rogoshin SV, Tsyurupa MP. *J Polym Sci C Polym Symp*, 1974, 47: 95–101
15 Davankov VA, Timofeeva GI, Ilyin MM, Tsyurupa MP. *J Polym Sci Polym Chem*, 1997, 35: 3847–3852
16 Veverka P, Jeřábek K. *React Funct Polyms*, 1999, 41: 21–25
17 Cote AP, Benin AI, Ockwig NW, O'Keeffe M, Matzger AJ, Yaghi OM. *Science*, 2005, 310: 1166–1170
18 Ding SY, Gao J, Wang Q, Zhang Y, Song WG, Su CY, Wang W. *J Am Chem Soc*, 2011, 133: 19816–19822
19 Kuhn P, Antonietti M, Thomas A. *Angew Chem Int Ed*, 2008, 47: 3450–3453
20 Yu B, Geng S, Wang H, Zhou W, Zhang Z, Chen B, Jiang J. *Angew Chem Intl Ed*, 2021, 60: 25942–25948
21 Feng L, Yuan Y, Yan B, Feng T, Jian Y, Zhang J, Sun W, Lin K, Luo G, Wang N. *Nat Commun*, 2022, 13: 1389
22 Wei P, He X, Zheng Z, He D, Li Q, Gong J, Zhang J, Sung HHY, Williams ID, Lam JWY, Liu M, Tang BZ. *Angew Chem Int Ed*, 2021, 60: 7148–7154
23 Liu X, Xu Y, Jiang D. *J Am Chem Soc*, 2012, 134: 8738–8741
24 Wang M, Zhang H, Guo L, Cao D. *Sens Actuat B-Chem*, 2018, 274: 102–109
25 Xu Y, Zhang C, Mu P, Mao N, Wang X, He Q, Wang F, Jiang JX. *Sci China Chem*, 2017, 60: 1075–1083
26 Xu Y, Mao N, Feng S, Zhang C, Wang F, Chen Y, Zeng J, Jiang JX. *Macromol Chem Phys*, 2017, 218: 1700049
27 Totten RK, Olenick LL, Kim YS, Chakraborty S, Weston MH, Farha OK, Hupp JT, Nguyen SBT. *Chem Sci*, 2014, 5: 782–787
28 Sonogashira K, Tohda Y, Hagihara N. *Tetrahedron Lett*, 1975, 16: 4467–4470
29 Ding X, Han BH. *Angew Chem Int Ed*, 2015, 54: 6536–6539
30 Zhuang X, Zhao W, Zhang F, Cao Y, Liu F, Bi S, Feng X. *Polym Chem*, 2016, 7: 4176–4181
31 Chen R, Shi J, Ma Y, Lin G, Lang X, Wang C. *Angew Chem Int Ed*, 2019, 58: 6430–6434
32 Warshawsky A, Deshe A, Gutman R. *Bri Polym J*, 1984, 16: 234–238
33 Sharma V, Sahoo A, Sharma Y, Mohanty P. *RSC Adv*, 2015, 5: 45749–45754
34 Huang N, Day G, Yang X, Drake H, Zhou HC. *Sci China Chem*, 2017, 60: 1007–1014
35 Liao Y, Weber J, Faul CFJ. *Chem Commun*, 2014, 50: 8002–8005
36 Jiang JX, Su F, Trewin A, Wood C , Campbell N, Niu H, Dickinson C, Ganin A, Rosseinsky M, Khimyak Y, Cooper A. *Angew Chem Int Ed*, 2007, 46: 8574–8578
37 Dawson R, Laybourn A, Khimyak YZ, Adams DJ, Cooper AI. *Macromolecules*, 2010, 43: 8524–8530
38 Mane S, Li YX, Liu XQ, Yue MB, Sun LB. *ACS Sustain Chem Eng*, 2018, 6: 17419–17426
39 Ma L, Liu Y, Liu Y, Jiang S, Li P, Hao Y, Shao P, Yin A, Feng X, Wang B. *Angew Chem Int Ed*, 2019, 58: 4221–4226
40 Zhuang X, Gehrig D, Forler N, Liang H, Wagner M, Hansen MR, Laquai F, Zhang F, Feng X. *Adv Mater*, 2015, 27: 3789–3796
41 Xu J, Yu F, Hua J, Tang W, Yang C, Hu S, Zhao S, Zhang X, Xin Z, Niu D. *Chem Eng J*, 2020, 392: 123694
42 Zhang Q, Yu S, Wang Q, Xiao Q, Yue Y, Ren S. *Macromol Rapid Commun*, 2017, 38: 1700445
43 Lu G, Yang H, Zhu Y, Huggins T, Ren ZJ, Liu Z, Zhang W. *J Mater Chem A*, 2015, 3: 4954–4959
44 Yuan S, Dorney B, White D, Kirklin S, Zapol P, Yu L, Liu DJ. *Chem Commun*, 2010, 46: 4547–4549
45 Zhao YC, Zhou D, Chen Q, Zhang XJ, Bian N, Qi AD, Han BH. *Macromolecules*, 2011, 44: 6382–6388
46 Guo ZH, Wang C, Zhang Q, Che S, Zhou HC, Fang L. *Mater Chem Front*, 2018, 2: 396–401
47 Wang C, Li C, Rutledge ERC, Che S, Lee J, Kalin AJ, Zhang C, Zhou HC, Guo ZH, Fang L. *J Mater Chem A*, 2020, 8: 15891–15899
48 Jiang JX, Su F, Niu H, Wood CD, Campbell NL, Khimyak YZ, Cooper AI. *Chem Commun*, 2008, 486–488
49 Chen Q, Luo M, Hammershøj P, Zhou D, Han Y, Laursen BW, Yan CG, Han BH. *J Am Chem Soc*, 2012, 134: 6084–6087
50 Chen Q, Liu DP, Zhu JH, Han BH. *Macromolecules*, 2014, 47: 5926–5931
51 Chen Q, Liu DP, Luo M, Feng LJ, Zhao YC, Han BH. *Small*, 2014, 10: 308–315
52 Chen Q, Han BH. *Macromol Rapid Commun*, 2018, 39: 1800040
53 Zhang W, Tang J, Yu W, Huang Q, Fu Y, Kuang G, Pan C, Yu G. *ACS Catal*, 2018, 8: 8084–8091
54 Liang HP, Acharjya A, Anito DA, Vogl S, Wang TX, Thomas A, Han BH. *ACS Catal*, 2019, 9: 3959–3968
55 Zhang W, Li S, Tang X, Tang J, Pan C, Yu G. *Appl Catal B-Environ*, 2020, 272: 118982
56 Gu C, Dong W, Yao L, Lv Y, Zhang Z, Lu D, Ma Y. *Adv Mater*, 2012, 24: 2413–2417
57 Zhou Z, Li X, Guo D, Shinde DB, Lu D, Chen L, Liu X, Cao L, Aboalsaud AM, Hu Y, Lai Z. *Nat Commun*, 2020, 11: 5323
58 Park H, Bang E, Hong JJ, Lee S, Ko HL, Kwak HW, Park H, Kang KW, Kim R, Ryu SR, Kim G, Oh H, Kim H, Lee K, Kim M, Kim SY, Kim J, El-Baz K, Lee H, Song M, Jeong DG, Keum G, Nam J. *Angew Chem Int Ed*, 2020, 59: 11540–11549
59 Gu C, Huang N, Wu Y, Xu H, Jiang D. *Angew Chem Int Ed*, 2015, 54: 11540–11544
60 Liu H, Wang Y, Mo W, Tang H, Cheng Z, Chen Y, Zhang S, Ma H, Li B, Li X. *Adv Funct Mater*, 2020, 30: 1910275
61 Xia J, Yuan S, Wang Z, Kirklin S, Dorney B, Liu DJ, Yu L. *Macromolecules*, 2010, 43: 3325–3330
62 Sun CJ, Zhao XQ, Wang PF, Wang H, Han BH. *Sci China Chem*, 2017, 60: 1067–1074
63 Sun CJ, Wang PF, Wang H, Han BH. *Polym Chem*, 2016, 7: 5031–5038
64 Gu C, Huang N, Chen Y, Qin L, Xu H, Zhang S, Li F, Ma Y, Jiang D. *Angew Chem Int Ed*, 2015, 54: 13594–13598
65 Zhang M, Jing X, Zhao S, Shao P, Zhang Y, Yuan S, Li Y, Gu C, Wang X, Ye Y, Feng X, Wang B. *Angew Chem Int Ed*, 2019, 58: 8768–8772
66 Li Z, Wang J, Chen Q, Ai K, Lu L. *Sci China Chem*, 2021, 64: 1389–1400
67 Han J, Zhu Z, Li N, Chen D, Xu Q, Li H, He J, Lu J. *Appl Catal B-Environ*, 2021, 291: 120108
68 Chen J, Yan W, Townsend EJ, Feng J, Pan L, Del Angel Hernandez V, Faul CFJ. *Angew Chem Int Ed*, 2019, 58: 11715–11719
69 Li H, Lyu W, Liao Y. *Macromol Rapid Commun*, 2019, 40: 1900455
70 Kou Y, Xu Y, Guo Z, Jiang D. *Angew Chem Int Ed*, 2011, 50: 8753–8757
71 Lin J, Bi S, Fan Z, Fu Z, Meng Z, Hou Z, Zhang F. *Polym Chem*, 2021, 12: 1661–1667
72 Germain J, Fréchet JMJ, Svec F. *Chem Commun*, 2009, 1526
73 Wood CD, Tan B, Trewin A, Niu H, Bradshaw D, Rosseinsky MJ, Khimyak YZ, Campbell NL, Kirk R, Stöckel E, Cooper AI. *Chem Mater*, 2007, 19: 2034–2048
74 Budd PM, Ghanem BS, Makhseed S, McKeown NB, Msayib KJ, Tattershall CE. *Chem Commun*, 2004, 230
75 Ben T, Ren H, Ma S, Cao D, Lan J, Jing X, Wang W, Xu J, Deng F, Simmons J, Qiu S, Zhu G. *Angew Chem Int Ed*, 2009, 48: 9457–9460
76 Holst JR, Cooper AI. *Adv Mater*, 2010, 22: 5212–5216
77 Tian Y, Zhu G. *Chem Rev*, 2020, 120: 8934–8986
78 Ren H, Ben T, Sun F, Guo M, Jing X, Ma H, Cai K, Qiu S, Zhu G. *J Mater Chem*, 2011, 21: 10348
79 Zhao H, Jin Z, Su H, Jing X, Sun F, Zhu G. *Chem Commun*, 2011, 47: 6389–6391
80 Yuan R, Ren H, Yan Z, Wang A, Zhu G. *Polym Chem*, 2014, 5: 2266

81 Pei C, Ben T, Cui Y, Qiu S. *Adsorption*, 2012, 18: 375–380
82 Garibay SJ, Weston MH, Mondloch JE, Colón YJ, Farha OK, Hupp JT, Nguyen SBT. *CrystEngComm*, 2013, 15: 1515–1519
83 Hei ZH, Huang MH, Luo Y, Wang Y. *Polym Chem*, 2016, 7: 770–774
84 Lu W, Yuan D, Zhao D, Schilling CI, Plietzsch O, Muller T, Bräse S, Guenther J, Blümel J, Krishna R, Li Z, Zhou HC. *Chem Mater*, 2010, 22: 5964–5972
85 Jing X, Sun F, Ren H, Tian Y, Guo M, Li L, Zhu G. *Microporous Mesoporous Mater*, 2013, 165: 92–98
86 Yan Z, Ren H, Ma H, Yuan R, Yuan Y, Zou X, Sun F, Zhu G. *Microporous Mesoporous Mater*, 2013, 173: 92–98
87 Sun L, Liang Z, Yu J. *Polym Chem*, 2015, 6: 917–924
88 Zou X, Ren H, Zhu G. *Chem Commun*, 2013, 49: 3925–3936
89 Jiang L, Tian Y, Sun T, Zhu Y, Ren H, Zou X, Ma Y, Meihaus KR, Long JR, Zhu G. *J Am Chem Soc*, 2018, 140: 15724–15730
90 Shen X, Faheem M, Matsuo Y, Aziz S, Zhang X, Li Y, Song J, Tian Y, Zhu G. *J Mater Chem A*, 2019, 7: 2507–2512
91 Ben T, Pei C, Zhang D, Xu J, Deng F, Jing X, Qiu S. *Energy Environ Sci*, 2011, 4: 3991
92 Yuan D, Lu W, Zhao D, Zhou HC. *Adv Mater*, 2011, 23: 3723–3725
93 Li M, Ren H, Sun F, Tian Y, Zhu Y, Li J, Mu X, Xu J, Deng F, Zhu G. *Adv Mater*, 2018, 30: 1804169
94 Jia J, Chen Z, Jiang H, Belmabkhout Y, Mouchaham G, Aggarwal H, Adil K, Abou-Hamad E, Czaban-Jóźwiak J, Tchalala MR, Eddaoudi M. *Chem*, 2019, 5: 180–191
95 Sun JK, Antonietti M, Yuan J. *Chem Soc Rev*, 2016, 45: 6627–6656
96 Yuan Y, Sun F, Zhang F, Ren H, Guo M, Cai K, Jing X, Gao X, Zhu G. *Adv Mater*, 2013, 25: 6619–6624
97 Yuan Y, Sun F, Li L, Cui P, Zhu G. *Nat Commun*, 2014, 5: 4260
98 Yan Z, Yuan Y, Tian Y, Zhang D, Zhu G. *Angew Chem Int Ed*, 2015, 54: 12733–12737
99 Tian Y, Song J, Zhu Y, Zhao H, Muhammad F, Ma T, Chen M, Zhu G. *Chem Sci*, 2019, 10: 606–613
100 Song J, Li Y, Cao P, Jing X, Faheem M, Matsuo Y, Zhu Y, Tian Y, Wang X, Zhu G. *Adv Mater*, 2019, 31: 1902444
101 Zhang PP, Zou XQ, Song J, Tian YY, Zhu YL, Yu GL, Yuan Y, Zhu GS. *Adv Mater*, 2020, 32: 1907449
102 Ma H, Ren H, Zou X, Meng S, Sun F, Zhu G. *Polym Chem*, 2014, 5: 144–152
103 Ma H, Ren H, Zou X, Sun F, Yan Z, Cai K, Wang D, Zhu G. *J Mater Chem A*, 2013, 1: 752–758
104 Fan J, Wei Y, Wang J, Wu C, Shi H. *Anal Chim Acta*, 2009, 639: 42–50
105 Chen L, Xu S, Li J. *Chem Soc Rev*, 2011, 40: 2922–2942
106 Chen L, Wang X, Lu W, Wu X, Li J. *Chem Soc Rev*, 2016, 45: 2137–2211
107 Yang Y, Yan Z, Wang L, Meng Q, Yuan Y, Zhu G. *J Mater Chem A*, 2018, 6: 5202–5207
108 Yuan Y, Yang Y, Ma X, Meng Q, Wang L, Zhao S, Zhu G. *Adv Mater*, 2018, 30: 1706507
109 Yuan Y, Meng Q, Faheem M, Yang Y, Li Z, Wang Z, Deng D, Sun F, He H, Huang Y, Sha H, Zhu G. *ACS Cent Sci*, 2019, 5: 1432–1439
110 Yuan Y, Yang Y, Faheem M, Zou X, Ma X, Wang Z, Meng Q, Wang L, Zhao S, Zhu G. *Adv Mater*, 2018, 30: 1800069
111 Rowan SJ, Cantrill SJ, Cousins GRL, Sanders JKM, Stoddart JF. *Angew Chem Int Ed*, 2002, 41: 898–952
112 Yaghi OM, O'Keeffe M, Ockwig NW, Chae HK, Eddaoudi M, Kim J. *Nature*, 2003, 423: 705–714
113 Zhang G, Li X, Liao Q, Liu Y, Xi K, Huang W, Jia X. *Nat Commun*, 2018, 9: 2785
114 Mi Z, Yang P, Wang R, Unruangsri J, Yang W, Wang C, Guo J. *J Am Chem Soc*, 2019, 141: 14433–14442
115 Xing XL, He ZC, Ahmed SA, Liao Q, Guo LR, Ren S, Xi K, Ji LN, Wang K, Xia XH. *Anal Chem*, 2022, 94: 9851–9855
116 Ding SY, Cui XH, Feng J, Lu G, Wang W. *Chem Commun*, 2017, 53: 11956–11959
117 Tan J, Namuangruk S, Kong W, Kungwan N, Guo J, Wang C. *Angew Chem Int Ed*, 2016, 55: 13979–13984
118 Wang PL, Ding SY, Zhang ZC, Wang ZP, Wang W. *J Am Chem Soc*, 2019, 141: 18004–18008
119 Feng J, Zhang YJ, Ma SH, Yang C, Wang ZP, Ding SY, Li Y, Wang W. *J Am Chem Soc*, 2022, 144: 6594–6603
120 Zhao Y, Liu H, Wu C, Zhang Z, Pan Q, Hu F, Wang R, Li P, Huang X, Li Z. *Angew Chem Int Ed*, 2019, 58: 5376–5381
121 Zhou TY, Xu SQ, Wen Q, Pang ZF, Zhao X. *J Am Chem Soc*, 2014, 136: 15885–15888
122 Lin G, Ding H, Yuan D, Wang B, Wang C. *J Am Chem Soc*, 2016, 138: 3302–3305
123 Xu H, Chen X, Gao J, Lin J, Addicoat M, Irle S, Jiang D. *Chem Commun*, 2014, 50: 1292–1294
124 Zhong H, Wang M, Ghorbani-Asl M, Zhang J, Ly KH, Liao Z, Chen G, Wei Y, Biswal BP, Zschech E, Weidinger IM, Krasheninnikov AV, Dong R, Feng X. *J Am Chem Soc*, 2021, 143: 19992–20000
125 Chen D, Chen W, Xing G, Zhang T, Chen L. *Chem Eur J*, 2020, 26: 8377–8381
126 Qian C, Qi QY, Jiang GF, Cui FZ, Tian Y, Zhao X. *J Am Chem Soc*, 2017, 139: 6736–6743
127 Waller PJ, AlFaraj YS, Diercks CS, Jarenwattananon NN, Yaghi OM. *J Am Chem Soc*, 2018, 140: 9099–9103
128 Qian H, Meng F, Yang C, Yan X. *Angew Chem Int Ed*, 2020, 59: 17607–17613
129 Ma T, Kapustin EA, Yin SX, Liang L, Zhou Z, Niu J, Li LH, Wang Y, Su J, Li J, Wang X, Wang WD, Wang W, Sun J, Yaghi OM. *Science*, 2018, 361: 48–52
130 Li Y, Chen Q, Xu T, Xie Z, Liu J, Yu X, Ma S, Qin T, Chen L. *J Am Chem Soc*, 2019, 141: 13822–13828
131 Su Y, Wan Y, Xu H, Otake K, Tang X, Huang L, Kitagawa S, Gu C. *J Am Chem Soc*, 2020, 142: 13316–13321
132 Liu J, Yang T, Wang ZP, Wang PL, Feng J, Ding SY, Wang W. *J Am Chem Soc*, 2020, 142: 20956–20961
133 Wang K, Jia Z, Bai Y, Wang X, Hodgkiss SE, Chen L, Chong SY, Wang X, Yang H, Xu Y, Feng F, Ward JW, Cooper AI. *J Am Chem Soc*, 2020, 142: 11131–11138
134 Li XT, Zou J, Wang TH, Ma HC, Chen GJ, Dong YB. *J Am Chem Soc*, 2020, 142: 6521–6526
135 Wang JC, Kan X, Shang JY, Qiao H, Dong YB. *J Am Chem Soc*, 2020, 142: 16915–16920
136 Lu Z, Yang C, He L, Hong J, Huang C, Wu T, Wang X, Wu Z, Liu X, Miao Z, Zeng B, Xu Y, Yuan C, Dai L. *J Am Chem Soc*, 2022, 144: 9624–9633
137 Wei PF, Qi MZ, Wang ZP, Ding SY, Yu W, Liu Q, Wang LK, Wang HZ, An WK, Wang W. *J Am Chem Soc*, 2018, 140: 4623–4631
138 Jiang SY, Gan SX, Zhang X, Li H, Qi QY, Cui FZ, Lu J, Zhao X. *J Am Chem Soc*, 2019, 141: 14981–14986
139 Li C, Ma Y, Liu H, Tao L, Ren Y, Chen X, Li H, Yang Q. *Chin J Catal*, 2020, 41: 1288–1297
140 Liu H, Chu J, Yin Z, Cai X, Zhuang L, Deng H. *Chem*, 2018, 4: 1696–1709
141 Wang Y, Liu H, Pan Q, Wu C, Hao W, Xu J, Chen R, Liu J, Li Z, Zhao Y. *J Am Chem Soc*, 2020, 142: 5958–5963
142 Yang Z, Liu J, Li Y, Zhang G, Xing G, Chen L. *Angew Chem Int Ed*, 2021, 60: 20754–20759
143 Ren XR, Bai B, Zhang Q, Hao Q, Guo Y, Wan LJ, Wang D. *J Am Chem Soc*, 2022, 144: 2488–2494
144 Wang S, Li XX, Da L, Wang Y, Xiang Z, Wang W, Zhang YB, Cao D. *J Am Chem Soc*, 2021, 143: 15562–15566
145 Yuan C, Fu S, Yang K, Hou B, Liu Y, Jiang J, Cui Y. *J Am Chem Soc*, 2021, 143: 369–381
146 Cui W, Li F, Xu R, Zhang C, Chen X, Yan R, Liang R, Qiu J. *Angew Chem Int Ed*, 2020, 59: 17684–17690
147 Cui WR, Zhang CR, Jiang W, Li FF, Liang RP, Liu J, Qiu JD. *Nat Commun*, 2020, 11: 436
148 Bi S, Yang C, Zhang W, Xu J, Liu L, Wu D, Wang X, Han Y, Liang

Q, Zhang F. *Nat Commun*, 2019, 10: 2467
149 Bi S, Thiruvengadam P, Wei S, Zhang W, Zhang F, Gao L, Xu J, Wu D, Chen JS, Zhang F. *J Am Chem Soc*, 2020, 142: 11893–11900
150 Wei S, Zhang F, Zhang W, Qiang P, Yu K, Fu X, Wu D, Bi S, Zhang F. *J Am Chem Soc*, 2019, 141: 14272–14279
151 Zhang F, Wei S, Wei W, Zou J, Gu G, Wu D, Bi S, Zhang F. *Sci Bull*, 2020, 65: 1659–1666
152 Xu J, He Y, Bi S, Wang M, Yang P, Wu D, Wang J, Zhang F. *Angew Chem Int Ed*, 2019, 58: 12065–12069
153 Xu J, Yang C, Bi S, Wang W, He Y, Wu D, Liang Q, Wang X, Zhang F. *Angew Chem Int Ed*, 2020, 59: 23845–23853
154 Bi S, Meng F, Wu D, Zhang F. *J Am Chem Soc*, 2022, 144: 3653–3659
155 Zhai L, Yang S, Yang X, Ye W, Wang J, Chen W, Guo Y, Mi L, Wu Z, Soutis C, Xu Q, Jiang Z. *Chem Mater*, 2020, 32: 9747–9752
156 Wang Z, Yang Y, Zhao Z, Zhang P, Zhang Y, Liu J, Ma S, Cheng P, Chen Y, Zhang Z. *Nat Commun*, 2021, 12: 1982
157 Meng F, Bi S, Sun Z, Jiang B, Wu D, Chen J, Zhang F. *Angew Chem Int Ed*, 2021, 60: 13614–13620
158 Guan X, Li H, Ma Y, Xue M, Fang Q, Yan Y, Valtchev V, Qiu S. *Nat Chem*, 2019, 11: 587–594
159 Yue Y, Li H, Chen H, Huang N. *J Am Chem Soc*, 2022, 144: 2873–2878
160 Liang RR, Xu SQ, Zhang L, A RH, Chen P, Cui FZ, Qi QY, Sun J, Zhao X. *Nat Commun*, 2019, 10: 4609
161 Kang X, Han X, Yuan C, Cheng C, Liu Y, Cui Y. *J Am Chem Soc*, 2020, 142: 16346–16356
162 Li H, Ding J, Guan X, Chen F, Li C, Zhu L, Xue M, Yuan D, Valtchev V, Yan Y, Qiu S, Fang Q. *J Am Chem Soc*, 2020, 142: 13334–13338
163 Li H, Chen F, Guan X, Li J, Li C, Tang B, Valtchev V, Yan Y, Qiu S, Fang Q. *J Am Chem Soc*, 2021, 143: 2654–2659
164 Li Z, Sheng L, Wang H, Wang X, Li M, Xu Y, Cui H, Zhang H, Liang H, Xu H, He X. *J Am Chem Soc*, 2021, 143: 92–96
165 Li Z, Sheng L, Hsueh C, Wang X, Cui H, Gao H, Wu Y, Wang J, Tang Y, Xu H, He X. *Chem Mater*, 2021, 33: 9618–9623
166 Wang X, Han X, Cheng C, Kang X, Liu Y, Cui Y. *J Am Chem Soc*, 2022, 144: 7366–7373
167 Lan Y, Han X, Tong M, Huang H, Yang Q, Liu D, Zhao X, Zhong C. *Nat Commun*, 2018, 9: 5274
168 Shan Z, Wu M, Zhu D, Wu X, Zhang K, Verduzco R, Zhang G. *J Am Chem Soc*, 2022, 144: 5728–5733
169 Xie Y, Li J, Lin C, Gui B, Ji C, Yuan D, Sun J, Wang C. *J Am Chem Soc*, 2021, 143: 7279–7284
170 Xu HS, Ding SY, An WK, Wu H, Wang W. *J Am Chem Soc*, 2016, 138: 11489–11492
171 Wang L, Zhou J, Lan Y, Ding S, Yu W, Wang W. *Angew Chem Int Ed*, 2019, 58: 9443–9447
172 Zhang J, Han X, Wu X, Liu Y, Cui Y. *J Am Chem Soc*, 2017, 139: 8277–8285
173 Han X, Zhang J, Huang J, Wu X, Yuan D, Liu Y, Cui Y. *Nat Commun*, 2018, 9: 1294
174 Wang X, Han X, Zhang J, Wu X, Liu Y, Cui Y. *J Am Chem Soc*, 2016, 138: 12332–12335
175 Han X, Huang J, Yuan C, Liu Y, Cui Y. *J Am Chem Soc*, 2018, 140: 892–895
176 Qian HL, Yang CX, Yan XP. *Nat Commun*, 2016, 7: 12104
177 Han X, Xia Q, Huang J, Liu Y, Tan C, Cui Y. *J Am Chem Soc*, 2017, 139: 8693–8697
178 Ma HC, Kan JL, Chen GJ, Chen CX, Dong YB. *Chem Mater*, 2017, 29: 6518–6524
179 Ma HC, Zhao CC, Chen GJ, Dong YB. *Nat Commun*, 2019, 10: 3368
180 Wu X, Han X, Xu Q, Liu Y, Yuan C, Yang S, Liu Y, Jiang J, Cui Y. *J Am Chem Soc*, 2019, 141: 7081–7089
181 Hou B, Yang S, Yang K, Han X, Tang X, Liu Y, Jiang J, Cui Y. *Angew Chem Int Ed*, 2021, 60: 6086–6093
182 Ma HC, Chen GJ, Huang F, Dong YB. *J Am Chem Soc*, 2020, 142: 12574–12578
183 Yuan C, Jia W, Yu Z, Li Y, Zi M, Yuan LM, Cui Y. *J Am Chem Soc*, 2022, 144: 891–900
184 Hao L, Ning J, Luo B, Wang B, Zhang Y, Tang Z, Yang J, Thomas A, Zhi L. *J Am Chem Soc*, 2015, 137: 219–225
185 Liu J, Lyu P, Zhang Y, Nachtigall P, Xu Y. *Adv Mater*, 2018, 30: 1705401
186 Talapaneni SN, Hwang TH, Je SH, Buyukcakir O, Choi JW, Coskun A. *Angew Chem Int Ed*, 2016, 55: 3106–3111
187 Xie J, Shevlin SA, Ruan Q, Moniz SJA, Liu Y, Liu X, Li Y, Lau CC, Guo ZX, Tang J. *Energy Environ Sci*, 2018, 11: 1617–1624
188 Zhao Y, Yao KX, Teng B, Zhang T, Han Y. *Energy Environ Sci*, 2013, 6: 3684–3692
189 Lan ZA, Fang Y, Zhang Y, Wang X. *Angew Chem Int Ed*, 2018, 57: 470–474
190 Liu M, Guo L, Jin S, Tan B. *J Mater Chem A*, 2019, 7: 5153–5172
191 Sun T, Liang Y, Xu Y. *Angew Chem Int Ed*, 2022, 61: e2113926
192 Yang Z, Chen H, Wang S, Guo W, Wang T, Suo X, Jiang D, Zhu X, Popovs I, Dai S. *J Am Chem Soc*, 2020, 142: 6856–6860
193 Wang N, Cheng G, Guo L, Tan B, Jin S. *Adv Funct Mater*, 2019, 29: 1904781
194 Chen H, Suo X, Yang Z, Dai S. *Adv Mater*, 2022, 34: 2107947
195 Zhu X, Tian C, Mahurin SM, Chai SH, Wang C, Brown S, Veith GM, Luo H, Liu H, Dai S. *J Am Chem Soc*, 2012, 134: 10478–10484
196 Yu S, Mahmood J, Noh H, Seo J, Jung S, Shin S, Im Y, Jeon I, Baek J. *Angew Chem Int Ed*, 2018, 57: 8438–8442
197 Wang K, Yang LM, Wang X, Guo L, Cheng G, Zhang C, Jin S, Tan B, Cooper A. *Angew Chem Int Ed*, 2017, 56: 14149–14153
198 Bojdys MJ, Jeromenok J, Thomas A, Antonietti M. *Adv Mater*, 2010, 22: 2202–2205
199 Lan Z-, Wu M, Fang Z, Zhang Y, Chen X, Zhang G, Wang X. *Angew Chem Int Ed*, 2022, 61: e2201482
200 Ren S, Bojdys MJ, Dawson R, Laybourn A, Khimyak YZ, Adams DJ, Cooper AI. *Adv Mater*, 2012, 24: 2357–2361
201 Liu J, Zan W, Li K, Yang Y, Bu F, Xu Y. *J Am Chem Soc*, 2017, 139: 11666–11669
202 Liu M, Huang Q, Wang S, Li Z, Li B, Jin S, Tan B. *Angew Chem Int Ed*, 2018, 57: 11968–11972
203 Liu M, Jiang K, Ding X, Wang S, Zhang C, Liu J, Zhan Z, Cheng G, Li B, Chen H, Jin S, Tan B. *Adv Mater*, 2019, 31: 1807865
204 Wang X, Zhang S, Li X, Zhan Z, Tan B, Lang X, Jin S. *J Mater Chem A*, 2021, 9: 16405–16410
205 Zhang S, Cheng G, Guo L, Wang N, Tan B, Jin S. *Angew Chem Int Ed*, 2020, 59: 6007–6014
206 Guan L, Cheng G, Tan B, Jin S. *Chem Commun*, 2021, 57: 5147–5150
207 Sun R, Wang X, Wang X, Tan B. *Angew Chem Int Ed*, 2022, 61: e2117668
208 Hu X, Zheng L, Wang S, Wang X, Tan B. *Chem Commun*, 2022, 58: 8121–8124
209 Huang W, He Q, Hu Y, Li Y. *Angew Chem Int Ed*, 2019, 58: 8676–8680
210 Guo L, Niu Y, Razzaque S, Tan B, Jin S. *ACS Catal*, 2019, 9: 9438–9445
211 Guo L, Niu Y, Xu H, Li Q, Razzaque S, Huang Q, Jin S, Tan B. *J Mater Chem A*, 2018, 6: 19775–19781
212 Slater AG, Cooper AI. *Science*, 2015, 348: aaa8075
213 Yang Z, Liu T, Wang S, Chen H, Suo X, Wang T, Thapaliya BP, Jiang D, Popovs I, Dai S. *Chem Mater*, 2021, 33: 3386–3393
214 Yang Z, Guo W, Mahurin SM, Wang S, Chen H, Cheng L, Jie K, Meyer Iii HM, Jiang D, Liu G, Jin W, Popovs I, Dai S. *Chem*, 2020, 6: 631–645
215 Gao ZZ, Wang ZK, Wei L, Yin G, Tian J, Liu CZ, Wang H, Zhang DW, Zhang YB, Li X, Liu Y, Li ZT. *ACS Appl Mater Interfaces*, 2020, 12: 1404–1411
216 Tian J, Chen L, Zhang DW, Liu Y, Li ZT. *Chem Commun*, 2016, 52: 6351–6362

217 Lin JL, Wang ZK, Xu ZY, Wei L, Zhang YC, Wang H, Zhang DW, Zhou W, Zhang YB, Liu Y, Li ZT. *J Am Chem Soc*, 2020, 142: 3577–3582
218 Wang P, Miao X, Meng Y, Wang Q, Wang J, Duan H, Li Y, Li C, Liu J, Cao L. *ACS Appl Mater Interfaces*, 2020, 12: 22630–22639
219 Zhang KD, Tian J, Hanifi D, Zhang Y, Sue ACH, Zhou TY, Zhang L, Zhao X, Liu Y, Li ZT. *J Am Chem Soc*, 2013, 135: 17913–17918
220 Krieg E, Bastings MMC, Besenius P, Rybtchinski B. *Chem Rev*, 2016, 116: 2414–2477
221 Zou H, Liu J, Li Y, Li X, Wang X. *Small*, 2018, 14: 1802234
222 Tian J, Zhang L, Wang H, Zhang DW, Li ZT. *Supramol Chem*, 2016, 28: 769–783
223 Zhang ZJ, Zhang YM, Liu Y. *J Org Chem*, 2011, 76: 4682–4685
224 Jiang SY, Zhao X. *Chin J Polym Sci*, 2019, 37: 1–10
225 Zhou TY, Qi QY, Zhao QL, Fu J, Liu Y, Ma Z, Zhao X. *Polym Chem*, 2015, 6: 3018–3023
226 Lee HJ, Kim HJ, Lee EC, Kim J, Park SY. *Chem Asian J*, 2018, 13: 390–394
227 Liu H, Zhang Z, Zhao Y, Zhou Y, Xue B, Han Y, Wang Y, Mu X, Zang S, Zhou X, Li Z. *J Mater Chem B*, 2019, 7: 1435–1441
228 Tian X, Zuo M, Niu P, Wang K, Hu X. *Inorg Chem*, 2020, 40: 1823–1834
229 Han T, Yan D, Wu Q, Song N, Zhang H, Wang D. *Chin J Chem*, 2021, 39: 677–689
230 Xu SQ, Zhang X, Nie CB, Pang ZF, Xu XN, Zhao X. *Chem Commun*, 2015, 51: 16417–16420
231 Li Y, Dong Y, Miao X, Ren Y, Zhang B, Wang P, Yu Y, Li B, Isaacs L, Cao L. *Angew Chem Int Ed*, 2018, 57: 729–733
232 Li Y, Li Q, Miao X, Qin C, Chu D, Cao L. *Angew Chem Int Ed*, 2021, 60: 6744–6751
233 Zhang X, Nie CB, Zhou TY, Qi QY, Fu J, Wang XZ, Dai L, Chen Y, Zhao X. *Polym Chem*, 2015, 6: 1923–1927
234 Zhang L, Jia Y, Wang H, Zhang DW, Zhang Q, Liu Y, Li ZT. *Polym Chem*, 2016, 7: 1861–1865
235 Zhang L, Zhou TY, Tian J, Wang H, Zhang DW, Zhao X, Liu Y, Li ZT. *Polym Chem*, 2014, 5: 4715–4721
236 Yang B, Yu S, Zhang P, Wang Z, Qi Q, Wang X, Xu X, Yang H, Wu Z, Liu Y, Ma D, Li Z. *Angew Chem Int Ed*, 2021, 60: 26268–26275
237 Tian J, Zhou TY, Zhang SC, Aloni S, Altoe MV, Xie SH, Wang H, Zhang DW, Zhao X, Liu Y, Li ZT. *Nat Commun*, 2014, 5: 5574
238 Tian J, Yao C, Yang WL, Zhang L, Zhang DW, Wang H, Zhang F, Liu Y, Li ZT. *Chin Chem Lett*, 2017, 28: 798–806
239 Yao C, Tian J, Wang H, Zhang DW, Liu Y, Zhang F, Li ZT. *Chin Chem Lett*, 2017, 28: 893–899
240 Yan M, Liu XB, Gao ZZ, Wu YP, Hou JL, Wang H, Zhang DW, Liu Y, Li ZT. *Org Chem Front*, 2019, 6: 1698–1704
241 Yang B, Zhang JW, Yu SB, Wang ZK, Zhang PQ, Yang XD, Qi QY, Yang GY, Ma D, Li ZT. *Sci China Chem*, 2021, 64: 1228–1234
242 Yang B, Zhang XD, Li J, Tian J, Wu YP, Yu FX, Wang R, Wang H, Zhang DW, Liu Y, Zhou L, Li ZT. *CCS Chem*, 2019, 1: 156–165
243 Yu S, Qi Q, Yang B, Wang H, Zhang D, Liu Y, Li Z. *Small*, 2018, 14: 1801037
244 Wu YP, Wang ZK, Wang H, Zhang DW, Zhao X, Li ZT. *Acta Chim Sin*, 2019, 77: 735
245 Tian J, Xu ZY, Zhang DW, Wang H, Xie SH, Xu DW, Ren YH, Wang H, Liu Y, Li ZT. *Nat Commun*, 2016, 7: 11580
246 Li XF, Yu SB, Yang B, Tian J, Wang H, Zhang DW, Liu Y, Li ZT. *Sci China Chem*, 2018, 61: 830–835
247 Gao ZZ, Xu YY, Wang ZK, Wang H, Zhang DW, Li ZT. *ACS Appl Polym Mater*, 2020, 2: 4885–4892
248 Li XF, Liu XB, Chao JY, Wang ZK, Rahman FU, Wang H, Zhang DW, Liu Y, Li ZT. *Sci China Chem*, 2019, 62: 1634–1638
249 Zhang Y, Xu Z, Wang Z, Wang H, Zhang D, Liu Y, Li Z. *ChemPlusChem*, 2020, 85: 1498–1503
250 Germain J, Fréchet JMJ, Svec F. *J Mater Chem*, 2007, 17: 4989–4997
251 Ahn JH, Jang JE, Oh CG, Ihm SK, Cortez J, Sherrington DC. *Macromolecules*, 2006, 39: 627–632
252 Li B, Gong R, Luo Y, Tan B. *Soft Matter*, 2011, 7: 10910–10916
253 Urban J, Svec F, Fréchet JMJ. *Anal Chem*, 2010, 82: 1621–1623
254 Urban J, Svec F, Fréchet JMJ. *J Chromatogr A*, 2010, 1217: 8212–8221
255 Seo M, Kim S, Oh J, Kim SJ, Hillmyer MA. *J Am Chem Soc*, 2015, 137: 600–603
256 Tsyurupa MP, Davankov VA. *React Funct Polyms*, 2002, 53: 193–203
257 Webster OW, Gentry FP, Farlee RD, Smart BE. *Makromol Chem Macromol Symp*, 1992, 54-55: 477–482
258 Urban C, McCord EF, Webster OW, Abrams L, Long HW, Gaede H, Tang P, Pines A. *Chem Mater*, 1995, 7: 1325–1332
259 Shea KJ, Loy DA, Webster OW. *Chem Mater*, 1989, 1: 572–574
260 Loy DA, Shea KJ. *Chem Rev*, 1995, 95: 1431–1442
261 Gao H, Ding L, Li W, Ma G, Bai H, Li L. *ACS Macro Lett*, 2016, 5: 377–381
262 Wood CD, Tan B, Trewin A, Su F, Rosseinsky MJ, Bradshaw D, Sun Y, Zhou L, Cooper AI. *Adv Mater*, 2008, 20: 1916–1921
263 Sarkar C, Shit SC, Dao DQ, Lee J, Tran NH, Singuru R, An K, Nguyen DN, Le QV, Amaniampong PN, Drif A, Jerome F, Huyen PT, Phan TTN, Vo DVN, Thanh Binh N, Trinh QT, Sherburne MP, Mondal J. *Green Chem*, 2020, 22: 2049–2068
264 Li B, Gong R, Wang W, Huang X, Zhang W, Li H, Hu C, Tan B. *Macromolecules*, 2011, 44: 2410–2414
265 Errahali M, Gatti G, Tei L, Paul G, Rolla GA, Canti L, Fraccarollo A, Cossi M, Comotti A, Sozzani P, Marchese L. *J Phys Chem C*, 2014, 118: 28699–28710
266 Cui P, Jing XF, Yuan Y, Zhu GS. *Chin Chem Lett*, 2016, 27: 1479–1484
267 Puthiaraj P, Ahn WS. *Ind Eng Chem Res*, 2016, 55: 7917–7923
268 Modak A, Maegawa Y, Goto Y, Inagaki S. *Polym Chem*, 2016, 7: 1290–1296
269 Zhang C, Zhu PC, Tan L, Liu JM, Tan B, Yang XL, Xu HB. *Macromolecules*, 2015, 48: 8509–8514
270 Luo Y, Li B, Wang W, Wu K, Tan B. *Adv Mater*, 2012, 24: 5703–5707
271 Saleh M, Lee HM, Kemp KC, Kim KS. *ACS Appl Mater Interfaces*, 2014, 6: 7325–7333
272 Yang X, Yu M, Zhao Y, Zhang C, Wang X, Jiang JX. *J Mater Chem A*, 2014, 2: 15139–15145
273 Yao S, Yang X, Yu M, Zhang Y, Jiang JX. *J Mater Chem A*, 2014, 2: 8054–8059
274 Wang S, Zhang C, Shu Y, Jiang S, Xia Q, Chen L, Jin S, Hussain I, Cooper AI, Tan B. *Sci Adv*, 2017, 3: e1602610
275 Moore JC. *J Polym Sci Polym Chem*, 1996, 34: 1833–1841
276 Zhu T, Xie F, Huang T, Tian K, Wu Z, Yang H, Li L. *ACS Macro Lett*, 2018, 7: 1283–1288
277 Sun Q, Jiang M, Shen Z, Jin Y, Pan S, Wang L, Meng X, Chen W, Ding Y, Li J, Xiao FS. *Chem Commun*, 2014, 50: 11844–11847
278 Huangfu Y, Sun Q, Pan S, Meng X, Xiao FS. *ACS Catal*, 2015, 5: 1556–1559
279 Wuttke S, Medina DD, Rotter JM, Begum S, Stassin T, Ameloot R, Oschatz M, Tsotsalas M. *Adv Funct Mater*, 2018, 28: 1801545
280 Liu XH, Guan CZ, Wang D, Wan LJ. *Adv Mater*, 2014, 26: 6912–6920
281 Lafferentz L, Eberhardt V, Dri C, Africh C, Comelli G, Esch F, Hecht S, Grill L. *Nat Chem*, 2012, 4: 215–220
282 Guan CZ, Wang D, Wan LJ. *Chem Commun*, 2012, 48: 2943–2945
283 Liu XH, Guan CZ, Ding SY, Wang W, Yan HJ, Wang D, Wan LJ. *J Am Chem Soc*, 2013, 135: 10470–10474
284 Grill L, Dyer M, Lafferentz L, Persson M, Peters MV, Hecht S. *Nat Nanotech*, 2007, 2: 687–691
285 Gutzler R, Walch H, Eder G, Kloft S, Heckl WM, Lackinger M. *Chem Commun*, 2009, 4456
286 Wang W, Shi X, Wang S, Van Hove MA, Lin N. *J Am Chem Soc*, 2011, 133: 13264–13267

287 Bieri M, Nguyen MT, Gröning O, Cai J, Treier M, Aït-Mansour K, Ruffieux P, Pignedoli CA, Passerone D, Kastler M, Müllen K, Fasel R. *J Am Chem Soc*, 2010, 132: 16669–16676
288 Zhang YQ, Kepčija N, Kleinschrodt M, Diller K, Fischer S, Papageorgiou AC, Allegretti F, Björk J, Klyatskaya S, Klappenberger F, Ruben M, Barth JV. *Nat Commun*, 2012, 3: 1286
289 Yue JY, Mo YP, Li SY, Dong WL, Chen T, Wang D. *Chem Sci*, 2017, 8: 2169–2174
290 Dienstmaier JF, Medina DD, Dogru M, Knochel P, Bein T, Heckl WM, Lackinger M. *ACS Nano*, 2012, 6: 7234–7242
291 Colson JW, Woll AR, Mukherjee A, Levendorf MP, Spitler EL, Shields VB, Spencer MG, Park J, Dichtel WR. *Science*, 2011, 332: 228–231
292 Ratsch M, Ye C, Yang Y, Zhang A, Evans AM, Börjesson K. *J Am Chem Soc*, 2020, 142: 6548–6553
293 Zhao S, Jiang C, Fan J, Hong S, Mei P, Yao R, Liu Y, Zhang S, Li H, Zhang H, Sun C, Guo Z, Shao P, Zhu Y, Zhang J, Guo L, Ma Y, Zhang J, Feng X, Wang F, Wu H, Wang B. *Nat Mater*, 2021, 20: 1551–1558
294 Zhou Z, Shinde DB, Guo D, Cao L, Nuaimi RA, Zhang Y, Enakonda LR, Lai Z. *Adv Funct Mater*, 2022, 32: 2108672
295 Lindemann P, Tsotsalas M, Shishatskiy S, Abetz V, Krolla-Sidenstein P, Azucena C, Monnereau L, Beyer A, Gölzhäuser A, Mugnaini V, Gliemann H, Bräse S, Wöll C. *Chem Mater*, 2014, 26: 7189–7193
296 Cai SL, Zhang YB, Pun AB, He B, Yang J, Toma FM, Sharp ID, Yaghi OM, Fan J, Zheng SR, Zhang WG, Liu Y. *Chem Sci*, 2014, 5: 4693–4700
297 Liang B, Wang H, Shi X, Shen B, He X, Ghazi ZA, Khan NA, Sin H, Khattak AM, Li L, Tang Z. *Nat Chem*, 2018, 10: 961–967
298 Ma Y, Cui F, Rong H, Song J, Jing X, Tian Y, Zhu G. *Angew Chem Int Ed*, 2022, 61: e202113682
299 Gu C, Chen Y, Zhang Z, Xue S, Sun S, Zhang K, Zhong C, Zhang H, Pan Y, Lv Y, Yang Y, Li F, Zhang S, Huang F, Ma Y. *Adv Mater*, 2013, 25: 3443–3448
300 Zhang M, Yu A, Wu X, Shao P, Huang X, Ma D, Han X, Xie J, Feng X, Wang B. *Nano Res*, 2022, 15: 2552–2557
301 Zhou Z, Guo D, Shinde DB, Cao L, Li Z, Li X, Lu D, Lai Z. *ACS Nano*, 2021, 15: 11970–11980
302 Gu C, Huang N, Chen Y, Zhang H, Zhang S, Li F, Ma Y, Jiang D. *Angew Chem Int Ed*, 2016, 55: 3049–3053
303 Shi QX, Yang CY, Pei HJ, Chang C, Guan X, Chen FY, Xie XL, Ye YS. *Chem Eng J*, 2021, 404: 127044
304 Shi X, Wang R, Xiao A, Jia T, Sun SP, Wang Y. *ACS Appl Nano Mater*, 2018, 1: 6320–6326
305 Michl J, Magnera TF. *Proc Natl Acad Sci USA*, 2002, 99: 4788–4792
306 Feldblyum JI, McCreery CH, Andrews SC, Kurosawa T, Santos EJG, Duong V, Fang L, Ayzner AL, Bao Z. *Chem Commun*, 2015, 51: 13894–13897
307 Dai W, Shao F, Szczerbiński J, McCaffrey R, Zenobi R, Jin Y, Schlüter AD, Zhang W. *Angew Chem Int Ed*, 2016, 55: 213–217
308 Sahabudeen H, Qi H, Glatz BA, Tranca D, Dong R, Hou Y, Zhang T, Kuttner C, Lehnert T, Seifert G, Kaiser U, Fery A, Zheng Z, Feng X. *Nat Commun*, 2016, 7: 13461
309 Kim S, Lim H, Lee J, Choi HC. *Langmuir*, 2018, 34: 8731–8738
310 Liu K, Qi H, Dong R, Shivhare R, Addicoat M, Zhang T, Sahabudeen H, Heine T, Mannsfeld S, Kaiser U, Zheng Z, Feng X. *Nat Chem*, 2019, 11: 994–1000
311 Dey K, Pal M, Rout KC, Kunjattu H S, Das A, Mukherjee R, Kharul UK, Banerjee R. *J Am Chem Soc*, 2017, 139: 13083–13091
312 Chen Y, Li Y, Dai L, Qin G, Guo J, Zhang Q, Li S, Sherazi TA, Zhang S. *Chem Commun*, 2021, 57: 3131–3134
313 Pfeffermann M, Dong R, Graf R, Zajaczkowski W, Gorelik T, Pisula W, Narita A, Müllen K, Feng X. *J Am Chem Soc*, 2015, 137: 14525–14532
314 Li K, Zhu J, Liu D, Zhang Y, Van der Bruggen B. *Chem Mater*, 2021, 33: 7047–7056
315 Matsumoto M, Valentino L, Stiehl GM, Balch HB, Corcos AR, Wang F, Ralph DC, Mariñas BJ, Dichtel WR. *Chem*, 2018, 4: 308–317
316 Hao Q, Zhao C, Sun B, Lu C, Liu J, Liu MJ, Wan LJ, Wang D. *J Am Chem Soc*, 2018, 140: 12152–12158
317 McKeown NB, Budd PM. *Chem Soc Rev*, 2006, 35: 675–683
318 Agarwal P, Hefner Jr. RE, Ge S, Tomlinson I, Rao YQ, Dikic T. *J Membrane Sci*, 2020, 595: 117501
319 Huang M, Lu K, Wang Z, Bi X, Zhang Y, Jin J. *ACS Sustain Chem Eng*, 2021, 9: 9426–9435
320 Cheng G, Hasell T, Trewin A, Adams DJ, Cooper AI. *Angew Chem Int Ed*, 2012, 51: 12727–12731
321 Yadav RK, Kumar A, Park NJ, Kong KJ, Baeg JO. *J Mater Chem A*, 2016, 4: 9413–9418
322 Kang Z, Peng Y, Qian Y, Yuan D, Addicoat MA, Heine T, Hu Z, Tee L, Guo Z, Zhao D. *Chem Mater*, 2016, 28: 1277–1285
323 Wu X, Li H, Xu Y, Xu B, Tong H, Wang L. *Nanoscale*, 2014, 6: 2375–2380
324 Smith BJ, Parent LR, Overholts AC, Beaucage PA, Bisbey RP, Chavez AD, Hwang N, Park C, Evans AM, Gianneschi NC, Dichtel WR. *ACS Cent Sci*, 2017, 3: 58–65
325 Moon SY, Bae JS, Jeon E, Park JW. *Angew Chem Int Ed*, 2010, 49: 9504–9508
326 Huang W, Li B, Wu Y, Zhang Y, Zhang W, Chen S, Fu Y, Yan T, Ma H. *ACS Appl Mater Interfaces*, 2021, 13: 13604–13612
327 Zhong H, Wu G, Fu Z, Lv H, Xu G, Wang R. *Adv Mater*, 2020, 32: 2000730
328 Bunck DN, Dichtel WR. *J Am Chem Soc*, 2013, 135: 14952–14955
329 Chandra S, Kandambeth S, Biswal BP, Lukose B, Kunjir SM, Chaudhary M, Babarao R, Heine T, Banerjee R. *J Am Chem Soc*, 2013, 135: 17853–17861
330 Peng Y, Huang Y, Zhu Y, Chen B, Wang L, Lai Z, Zhang Z, Zhao M, Tan C, Yang N, Shao F, Han Y, Zhang H. *J Am Chem Soc*, 2017, 139: 8698–8704
331 Lan X, Du C, Cao L, She T, Li Y, Bai G. *ACS Appl Mater Interfaces*, 2018, 10: 38953–38962
332 Bika P, Giannakopoulou T, Osokin V, Li M, Todorova N, Kaidatzis A, Taylor RA, Trapalis C, Dallas P. *J Mater Chem C*, 2021, 9: 13770–13781
333 Chou FY, Tang JC, Lee HY, Lee JC, Ratchahat S, Chen TH, Kaveevivitchai W. *ACS Appl Energy Mater*, 2020, 3: 11300–11306
334 Khayum MA, Kandambeth S, Mitra S, Nair SB, Das A, Nagane SS, Mukherjee R, Banerjee R. *Angew Chem Int Ed*, 2016, 55: 15604–15608
335 Medina DD, Rotter JM, Hu Y, Dogru M, Werner V, Auras F, Markiewicz JT, Knochel P, Bein T. *J Am Chem Soc*, 2015, 137: 1016–1019
336 Bisbey RP, DeBlase CR, Smith BJ, Dichtel WR. *J Am Chem Soc*, 2016, 138: 11433–11436
337 Li XD, Zhang Y, Guo JH, Yu SQ, Du DW. *Int J Hydrogen Energy*, 2019, 44: 8357–8364
338 Li A, Lu RF, Wang Y, Wang X, Han KL, Deng WQ. *Angew Chem Int Ed*, 2010, 49: 3330–3333
339 Liao C, Liang Z, Liu B, Chen H, Wang X, Li H. *ACS Appl Nano Mater*, 2020, 3: 2889–2898
340 Wang H, Jiang D, Huang D, Zeng G, Xu P, Lai C, Chen M, Cheng M, Zhang C, Wang Z. *J Mater Chem A*, 2019, 7: 22848–22870
341 Chang G, Shang Z, Yu T, Yang L. *J Mater Chem A*, 2016, 4: 2517–2523
342 Jiang F, Jin T, Zhu X, Tian Z, Do-Thanh CL, Hu J, Jiang D, Wang H, Liu H, Dai S. *Macromolecules*, 2016, 49: 5325–5330
343 Fu Y, Wang Z, Li S, He X, Pan C, Yan J, Yu G. *ACS Appl Mater Interfaces*, 2018, 10: 36002–36009
344 Tao J, Wang Y, Tang J, Xiong S, Umar Javaid M, Li G, Sun Q, Liu C, Pan C, Yu G. *Chem Eng J*, 2019, 373: 338–344
345 Konstas K, Taylor JW, Thornton AW, Doherty CM, Lim WX, Bastow TJ, Kennedy DF, Wood CD, Cox BJ, Hill JM, Hill AJ, Hill MR. *Angew Chem Int Ed*, 2012, 51: 6639–6642

346 Babarao R, Dai S, Jiang D. *Langmuir*, 2011, 27: 3451–3460
347 Lyndon R, Konstas K, Evans RA, Keddie DJ, Hill MR, Ladewig BP. *Adv Funct Mater*, 2015, 25: 4405–4411
348 Wang Y, Tao J, Xiong S, Lu P, Tang J, He J, Javaid MU, Pan C, Yu G. *Chem Eng J*, 2020, 380: 122420
349 Li H, Ding X, Han BH. *Chem Eur J*, 2016, 22: 11863–11868
350 Shang Z, Zhao B, Wu Z, Ding Y, Hu A. *ACS Appl Mater Interfaces*, 2020, 12: 56454–56461
351 Cossi M, Gatti G, Canti L, Tei L, Errahali M, Marchese L. *Langmuir*, 2012, 28: 14405–14414
352 Li Y, Ben T, Zhang B, Fu Y, Qiu S. *Sci Rep*, 2013, 3: 2420
353 Doonan CJ, Tranchemontagne DJ, Glover TG, Hunt JR, Yaghi OM. *Nat Chem*, 2010, 2: 235–238
354 Peterson GW, Farha OK, Schindler B, Jones P, Mahle J, Hupp JT. *J Porous Mater*, 2011, 19: 261–266
355 Weston MH, Peterson GW, Browe MA, Jones P, Farha OK, Hupp JT, Nguyen SBT. *Chem Commun*, 2013, 49: 2995–2997
356 Van Humbeck JF, McDonald TM, Jing X, Wiers BM, Zhu G, Long JR. *J Am Chem Soc*, 2014, 136: 2432–2440
357 Kang DW, Kang M, Moon M, Kim H, Eom S, Choe JH, Lee WR, Hong CS. *Chem Sci*, 2018, 9: 6871–6877
358 Yang Y, Faheem M, Wang L, Meng Q, Sha H, Yang N, Yuan Y, Zhu G. *ACS Cent Sci*, 2018, 4: 748–754
359 Han YS, An S, Dai J, Hu J, Xu Q, Song F, Li M, Peng C, Liu H. *ACS Appl Polym Mater*, 2021, 3: 4534–4542
360 Tian X, Qiu J, Wang Z, Chen Y, Li Z, Wang H, Zhao Y, Wang J. *Chem Commun*, 2022, 58: 1151–1154
361 Li J, Xiao Y, Shui F, Yi M, Zhang Z, Liu X, Zhang L, You Z, Yang R, Yang S, Li B, Bu X. *Chin J Chem*, 2022, 40: 2445–2450
362 Yang Y, Feng L, Ren J, Liu Y, Jin S, Su L, Wood C, Tan B. *Macromol Rapid Commun*, 2018, 39: 1800441
363 Guo YZ, Gao F, Wang Z, Liu YA, Hu WB, Yang H, Wen K. *ACS Appl Mater Interfaces*, 2021, 13: 16507–16515
364 Wang Q, Wu J, Hao L, Wu Q, Wang C, Wang Z. *J Sep Sci*, 2018, 41: 3285–3293
365 Zhang Y, Hong X, Cao XM, Huang XQ, Hu B, Ding SY, Lin H. *ACS Appl Mater Interfaces*, 2021, 13: 6359–6366
366 Duan HL, Deng X, Wang J, Fan L, Yang YC, Zhang ZQ. *Eur Polym J*, 2020, 133: 109762
367 Zhang Y, Wang X, Thiruvengadam P, Ming W, Qiu F, Yu K, Liu P, Su Y, Zhang F. *Polym Chem*, 2019, 10: 2792–2800
368 Fu J, Das S, Xing G, Ben T, Valtchev V, Qiu S. *J Am Chem Soc*, 2016, 138: 7673–7680
369 Khan NA, Zhang R, Wu H, Shen J, Yuan J, Fan C, Cao L, Olson MA, Jiang Z. *J Am Chem Soc*, 2020, 142: 13450–13458
370 Liu G, Wang Y, Shen C, Ju Z, Yuan D. *J Mater Chem A*, 2015, 3: 3051–3058
371 Wang Z, Ou Q, Ma H, Cheng G, Zhang QP, Tan B, Zhang C. *ACS Appl Polym Mater*, 2020, 3: 171–177
372 Wang Z, Liu J, Fu Y, Liu C, Pan C, Liu Z, Yu G. *Chem Commun*, 2017, 53: 4128–4131
373 Yu G, Li Y, Wang Z, Liu TX, Zhu G, Zou X. *J Membrane Sci*, 2019, 591: 117343
374 Qiao Z, Zhao S, Sheng M, Wang J, Wang S, Wang Z, Zhong C, Guiver MD. *Nat Mater*, 2019, 18: 163–168
375 Wang C, Guo F, Li H, Xu J, Hu J, Liu H. *J Membrane Sci*, 2018, 564: 115–122
376 Suo X, Cui X, Yang L, Xu N, Huang Y, He Y, Dai S, Xing H. *Adv Mater*, 2020, 32: 1907601
377 Lu Y, He J, Chen Y, Wang H, Zhao Y, Han Y, Ding Y. *Macromol Rapid Commun*, 2018, 39: 1700468
378 Jiang L, Wang P, Li M, Zhang P, Li J, Liu J, Ma Y, Ren H, Zhu G. *Chem Eur J*, 2019, 25: 9045–9051
379 Tang B, Wang W, Hou H, Liu Y, Liu Z, Geng L, Sun L, Luo A. *Chin Chem Lett*, 2022, 33: 898–902
380 Tao Y, Ji W, Ding X, Han BH. *J Mater Chem A*, 2021, 9: 7336–7365
381 Wang M, Pan F, Yang H, Cao Y, Wang H, Song Y, Lu Z, Sun M, Wu H, Jiang Z. *J Mater Chem A*, 2019, 7: 9912–9923
382 Soyekwo F, Zhang Q, Gao R, Qu Y, Lv R, Chen M, Zhu A, Liu Q. *J Mater Chem A*, 2017, 5: 583–592
383 Aguila B, Sun Q, Cassady H, Abney CW, Li B, Ma S. *ACS Appl Mater Interfaces*, 2019, 11: 30919–30926
384 Wang Z, Meng Q, Ma R, Wang Z, Yang Y, Sha H, Ma X, Ruan X, Zou X, Yuan Y, Zhu G. *Chem*, 2020, 6: 1683–1691
385 Wang Z, Ma R, Meng Q, Yang Y, Ma X, Ruan X, Yuan Y, Zhu G. *J Am Chem Soc*, 2021, 143: 14523–14529
386 Zhang P, Weng Z, Guo J, Wang C. *Chem Mater*, 2011, 23: 5243–5249
387 Li L, Chen Z, Zhong H, Wang R. *Chem Eur J*, 2014, 20: 3050–3060
388 Zhang C, Wang JJ, Liu Y, Ma H, Yang XL, Xu HB. *Chem Eur J*, 2013, 19: 5004–5008
389 Jing LP, Sun JS, Sun F, Chen P, Zhu G. *Chem Sci*, 2018, 9: 3523–3530
390 Li B, Guan Z, Wang W, Yang X, Hu J, Tan B, Li T. *Adv Mater*, 2012, 24: 3390–3395
391 Zhou YB, Wang YQ, Ning LC, Ding ZC, Wang WL, Ding CK, Li RH, Chen JJ, Lu X, Ding YJ, Zhan ZP. *J Am Chem Soc*, 2017, 139: 3966–3969
392 Li RH, Ding ZC, Li CY, Chen JJ, Zhou YB, An XM, Ding YJ, Zhan ZP. *Org Lett*, 2017, 19: 4432–4435
393 Li W, Li C, Xiong H, Liu Y, Huang W, Ji G, Jiang Z, Tang H, Pan Y, Ding Y. *Angew Chem Int Ed*, 2019, 58: 2448–2453
394 Wang CA, Zhang ZK, Yue T, Sun YL, Wang L, Wang WD, Zhang Y, Liu C, Wang W. *Chem Eur J*, 2012, 18: 6718–6723
395 Lan Y, Yang C, Zhang Y, An W, Xue H, Ding S, Zhou P, Wang W. *Polym Chem*, 2019, 10: 3298–3305
396 Zhang J, Han X, Wu X, Liu Y, Cui Y. *ACS Sustain Chem Eng*, 2019, 7: 5065–5071
397 Sun Q, Meng X, Liu X, Zhang X, Yang Y, Yang Q, Xiao FS. *Chem Commun*, 2012, 48: 10505–10507
398 Wang T, Lyu Y, Chen X, Li C, Jiang M, Song X, Ding Y. *RSC Adv*, 2016, 6: 28447–28450
399 Sun Q, Dai Z, Meng X, Xiao FS. *Chem Mater*, 2017, 29: 5720–5726
400 An WK, Han MY, Wang CA, Yu SM, Zhang Y, Bai S, Wang W. *Chem Eur J*, 2014, 20: 11019–11028
401 Wang X, Zhang J, Liu Y, Cui Y. *Bull Chem Soc Jpn*, 2014, 87: 435–440
402 Dong J, Liu Y, Cui Y. *Chem Commun*, 2014, 50: 14949–14952
403 Willis MC. *Chem Rev*, 2010, 110: 725–748
404 McDonald RI, Liu G, Stahl SS. *Chem Rev*, 2011, 111: 2981–3019
405 Cole-Hamilton DJ. *Science*, 2003, 299: 1702–1706
406 Li C, Xiong K, Yan L, Jiang M, Song X, Wang T, Chen X, Zhan Z, Ding Y. *Catal Sci Technol*, 2016, 6: 2143–2149
407 Li C, Yan L, Lu L, Xiong K, Wang W, Jiang M, Liu J, Song X, Zhan Z, Jiang Z, Ding Y. *Green Chem*, 2016, 18: 2995–3005
408 Li C, Sun K, Wang W, Yan L, Sun X, Wang Y, Xiong K, Zhan Z, Jiang Z, Ding Y. *J Catal*, 2017, 353: 123–132
409 Sun Q, Dai Z, Liu X, Sheng N, Deng F, Meng X, Xiao FS. *J Am Chem Soc*, 2015, 137: 5204–5209
410 https://www.Cas.Cn/cg/zh/202009/t20200914_4759805.Shtml. Secondary https://www.Cas.Cn/cg/zh/202009/t20200914_4759805.Shtml
411 Wang W, Zheng A, Zhao P, Xia C, Li F. *ACS Catal*, 2014, 4: 321–327
412 Li Y, Dong Y, Kan JL, Wu X, Dong YB. *Org Lett*, 2020, 22: 7363–7368
413 Chen X, Zhu H, Wang T, Li C, Yan L, Jiang M, Liu J, Sun X, Jiang Z, Ding Y. *J Mol Catal A-Chem*, 2016, 414: 37–46
414 Chen X, Zhu H, Wang W, Du H, Wang T, Yan L, Hu X, Ding Y. *ChemSusChem*, 2016, 9: 2451–2459
415 Dai Z, Sun Q, Liu X, Bian C, Wu Q, Pan S, Wang L, Meng X, Deng F, Xiao FS. *J Catal*, 2016, 338: 202–209
416 Wang W, Li C, Yan L, Wang Y, Jiang M, Ding Y. *ACS Catal*, 2016, 6: 6091–6100
417 Wang T, Wang W, Lyu Y, Chen X, Li C, Zhang Y, Song X, Ding Y.

RSC Adv, 2017, 7: 2836–2841
418 Zhong H, Gao J, Sa R, Yang S, Wu Z, Wang R. *ChemSusChem*, 2020, 2001658
419 Dong B, Wang L, Zhao S, Ge R, Song X, Wang Y, Gao Y. *Chem Commun*, 2016, 52: 7082–7085
420 Wang G, Jiang M, Ji G, Sun Z, Li C, Yan L, Ding Y. *ACS Sustain Chem Eng*, 2020, 8: 5576–5583
421 Hu C, Dai L. *Adv Mater*, 2019, 31: 1804672
422 Deng X, Albero J, Xu L, García H, Li Z. *Inorg Chem*, 2018, 57: 8276–8286
423 Zhao J, Wang Q, Sun C, Zheng T, Yan L, Li M, Shao K, Wang X, Su Z. *J Mater Chem A*, 2017, 5: 12498–12505
424 Tu W, Zhou Y, Zou Z. *Adv Mater*, 2014, 26: 4607–4626
425 Ma Y, Wang Z, Xu X, Wang J. *Chin J Catal*, 2017, 38: 1956–1969
426 Yang S, Hu W, Zhang X, He P, Pattengale B, Liu C, Cendejas M, Hermans I, Zhang X, Zhang J, Huang J. *J Am Chem Soc*, 2018, 140: 14614–14618
427 Guo S, Zhang H, Chen Y, Liu Z, Yu B, Zhao Y, Yang Z, Han B, Liu Z. *ACS Catal*, 2018, 8: 4576–4581
428 Yang P, Zhuzhang H, Wang R, Lin W, Wang X. *Angew Chem Int Ed*, 2019, 58: 1134–1137
429 Yu X, Yang Z, Qiu B, Guo S, Yang P, Yu B, Zhang H, Zhao Y, Yang X, Han B, Liu Z. *Angew Chem Int Ed*, 2019, 58: 632–636
430 Chen Y, Ji G, Guo S, Yu B, Zhao Y, Wu Y, Zhang H, Liu Z, Han B, Liu Z. *Green Chem*, 2017, 19: 5777–5781
431 Wang L, Wang R, Zhang X, Mu J, Zhou Z, Su Z. *ChemSusChem*, 2020, 13: 2973–2980
432 Lei K, Wang D, Ye L, Kou M, Deng Y, Ma Z, Wang L, Kong Y. *ChemSusChem*, 2020, 13: 1725–1729
433 Xu R, Wang XS, Zhao H, Lin H, Huang YB, Cao R. *Catal Sci Technol*, 2018, 8: 2224–2230
434 Orchanian NM, Hong LE, Skrainka JA, Esterhuizen JA, Popov DA, Marinescu SC. *ACS Appl Energy Mater*, 2019, 2: 110–123
435 Fu Z, Wang X, Gardner AM, Wang X, Chong SY, Neri G, Cowan AJ, Liu L, Li X, Vogel A, Clowes R, Bilton M, Chen L, Sprick RS, Cooper AI. *Chem Sci*, 2020, 11: 543–550
436 Zhang S, Wang S, Guo L, Chen H, Tan B, Jin S. *J Mater Chem C*, 2020, 8: 192–200
437 Yadav RK, Kumar A, Yadav D, Park NJ, Kim JY, Baeg JO. *ChemCatChem*, 2018, 10: 1928
438 Wisser FM, Duguet M, Perrinet Q, Ghosh AC, Alves-Favaro M, Mohr Y, Lorentz C, Quadrelli EA, Palkovits R, Farru-seng D, Mellot-Draznieks C, Waele V, Canivet J. *Angew Chem Int Ed*, 2020, 59: 5116–5122
439 Yang C, Huang W, da Silva LC, Zhang KAI, Wang X. *Chem Eur J*, 2018, 24: 17454–17458
440 Liu W, Li X, Wang C, Pan H, Liu W, Wang K, Zeng Q, Wang R, Jiang J. *J Am Chem Soc*, 2019, 141: 17431–17440
441 Sarkar P, Riyajuddin S, Das A, Hazra Chowdhury A, Ghosh K, Islam SM. *Mol Catal*, 2020, 484: 110730
442 Zhong W, Sa R, Li L, He Y, Li L, Bi J, Zhuang Z, Yu Y, Zou Z. *J Am Chem Soc*, 2019, 141: 7615–7621
443 Dai W, Xu H, Yu J, Hu X, Luo X, Tu X, Yang L. *Appl Surf Sci*, 2015, 356: 173–180
444 Sato S, Arai T, Morikawa T, Uemura K, Suzuki TM, Tanaka H, Kajino T. *J Am Chem Soc*, 2011, 133: 15240–15243
445 Wang S, Xu M, Peng T, Zhang C, Li T, Hussain I, Wang J, Tan B. *Nat Commun*, 2019, 10: 676
446 Zhan Z, Wang H, Huang Q, Li S, Yi X, Tang Q, Wang J, Tan B. *Small*, 2022, 18: 2105083
447 Ma Y, Yi X, Wang S, Li T, Tan B, Chen C, Majima T, Waclawik ER, Zhu H, Wang J. *Nat Commun*, 2022, 13: 1400
448 Guo S, Yang P, Zhao Y, Yu X, Wu Y, Zhang H, Yu B, Han B, George MW, Liu Z. *ChemSusChem*, 2020, 2000712